# Updates to the MAX IV 3 GeV Storage Ring Lattice

Simon C. Leemann

November 7, 2012 (Revised January 29, 2014)

MAX-lab Internal Note 20121107[1]

**Abstract**

The optics for the MAX IV 3 GeV storage ring have been modified and the official lattice has been updated. The new 20121107 branch [1] will replace the previous 20111213, 20111124, and 20110117 branches. The optics change has resulted from slightly modified field distributions in the dipole slices. The field distribution in the slices used in the updated lattice now properly resembles the distribution in the magnet design's 3D model [2] which is the basis for magnet production. Although only minor changes to the gradients in the dipoles and quadrupoles were required in order to restore the design linear optics, some lattice properties have changed and the nonlinear optics have been re-optimized to restore the design performance. This document describes the linear and nonlinear optics changes. Performance of the lattice is re-evaluated and a summary is included in this note. A list of current official lattice files and their purpose is appended.

[1] This document can be found at `http://www.maxlab.lu.se/node/999`

# 1 Summary of Modifications in the New Lattice

The following is a summary of modifications applied to the previous lattice branch m4-20111213-420 resulting in the new lattice branch m4-20121107-430.

- Dipole slices have a new field distribution. DIP and DIPm no longer make use of common slices.
- As a consequence of the previous item, quadrupole, sextupole, and octupole gradients have been modified to restore design optics.
- The vertical pinger magnet PV was moved from its provisional location R3_20S2 to its actual location in R3_10S2.

# 2 Updated Linear Optics

The dipole slice model for the 3 GeV storage ring was updated to match the field distribution in the 3D model used in magnet design [2] which is the model that the ongoing magnet production is based on. In this updated model, DIP and DIPm no longer contain common slices. This, however, is perfectly compatible with the real machine where the two different types of dipoles are powered by two separate power supplies (as are the pole-face strips in the different dipole types). The lengths and positions of the slices have not been modified (the nomenclature has, however). The updated slice model is detailed in Tables 1 and 2. Field distributions are displayed in Fig. 1.

Table 1: Parameters for the slices used to model DIP, i.e. one half of the 3° dipole in all unit cells.

| Slice | Length | Bend Angle | Dipole Field | Gradient | |
|---|---|---|---|---|---|
| | [mm] | [°] | [T] | $b_2$ [m$^{-2}$] | $K$ [T/m] |
| D0 | 361.89 | 1.094181 | 0.528159 | −0.864858 | −8.656046 |
| Df1 | 50.00 | 0.151199 | 0.528239 | −0.864908 | −8.656543 |
| Df2 | 50.00 | 0.151101 | 0.527897 | −0.866059 | −8.668066 |
| Df3 | 50.00 | 0.101861 | 0.355869 | −0.551829 | −5.523050 |
| Df4 | 50.00 | 0.001569 | 0.005481 | +0.011759 | +0.117695 |
| Df5 | 50.00 | 0.000089 | 0.000312 | −0.000128 | −0.001284 |

Table 2: Parameters for the slices used to model DIPm, i.e. the 1.5° dipole in all matching cells.

| Slice | Length | Bend Angle | Dipole Field | Gradient | |
|---|---|---|---|---|---|
| | [mm] | [°] | [T] | $b_2$ [m$^{-2}$] | $K$ [T/m] |
| Ds6 | 50.00 | 0.001070 | 0.003738 | +0.006608 | +0.066139 |
| Ds5 | 50.00 | 0.050729 | 0.177229 | −0.271428 | −2.716626 |
| Ds4 | 50.00 | 0.074672 | 0.260879 | −0.425119 | −4.254854 |
| Ds3 | 50.00 | 0.076248 | 0.266385 | −0.426048 | −4.264156 |
| Ds2 | 50.00 | 0.114983 | 0.401713 | −0.584884 | −5.853888 |
| Ds1 | 50.00 | 0.152049 | 0.531211 | −0.870351 | −8.711026 |
| Ds0 | 204.24 | 0.621695 | 0.531727 | −0.870701 | −8.714526 |
| Dm1 | 50.00 | 0.152220 | 0.531808 | −0.870751 | −8.715026 |
| Dm2 | 50.00 | 0.152122 | 0.531464 | −0.871910 | −8.726627 |
| Dm3 | 50.00 | 0.102549 | 0.358273 | −0.555557 | −5.560363 |
| Dm4 | 50.00 | 0.001579 | 0.005518 | +0.011839 | +0.118490 |
| Dm5 | 50.00 | 0.000090 | 0.000315 | −0.000129 | −0.001293 |

In order to restore the design linear optics the slice gradients in the tables above have been scaled with a common factor $\mathbf{f = 1.00002733}$ with respect to the slice model supplied by magnet design [2] (this factor is included in the gradients in Tables 1 and 2). This scaling corresponds to a very weak excitation of the pole-face strips in the real machine. The quadrupole gradients were also slightly modified in order to restore the original design linear optics. These adjustments are detailed in Table 3.

Table 3: List of gradient changes in order to restore design linear optics.

| Magnet family | Gradient change | Rel. difference |
|---|---|---|
| QF | $b_2 = 4.030907\,\mathrm{m}^{-2} \longrightarrow 4.030076\,\mathrm{m}^{-2}$ | −0.02% |
| QFm | $b_2 = 3.776156\,\mathrm{m}^{-2} \longrightarrow 3.773995\,\mathrm{m}^{-2}$ | −0.06% |
| QFend | $b_2 = 3.656234\,\mathrm{m}^{-2} \longrightarrow 3.653849\,\mathrm{m}^{-2}$ | −0.07% |
| QDend | $b_2 = -2.507705\,\mathrm{m}^{-2} \longrightarrow -2.503663\,\mathrm{m}^{-2}$ | −0.16% |

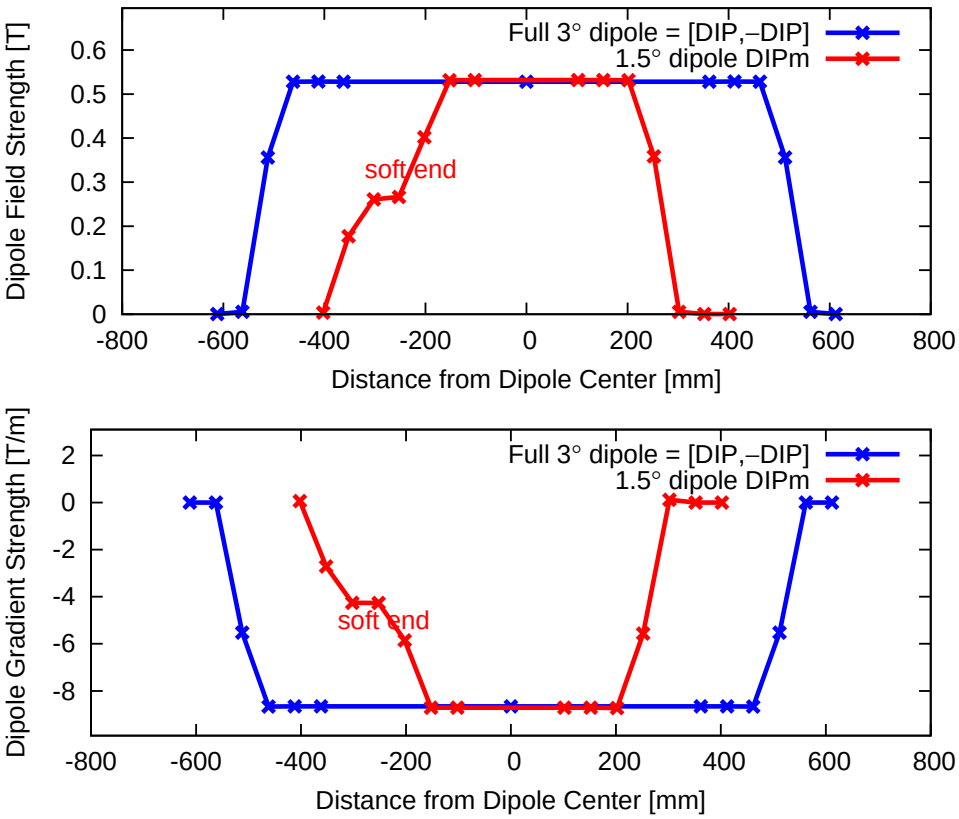


Figure 1: Dipole field and gradient strengths in the slices used to model DIP (i.e. one half of the 3° dipole in all unit cells) and DIPm (i.e. the 1.5° dipole in all matching cells).

With the above mentioned changes to dipole slice model and quadrupole gradients, the design optics were restored very well. Since the optics in the dipoles have been modified slightly, the radiation integrals have changed by a small amount. This leads to minor changes of certain lattice properties, e.g. emittance, energy spread, damping partition numbers, etc. An overview of the updated optics and lattice properties are given in Table 4 and Fig. 2.

Table 4: The most important properties of the updated lattice for the MAX IV 3 GeV storage ring.

| | |
|---|---|
| Periodicity | 20 |
| Circumference | 528 m |
| Horizontal tune $\nu_x$ | 42.20 |
| Vertical tune $\nu_y$ | 16.28 |
| Natural horizontal chromaticity $\xi_x$ | $-49.984$ |
| Natural vertical chromaticity $\xi_y$ | $-50.198$ |
| Momentum compaction (linear) $\alpha_c$ | $3.06\times10^{-4}$ |
| Horizontal damping partition $J_x$ | 1.8471 |
| Bare lattice emittance $\varepsilon_0$ | 0.328 nm rad |
| Bare lattice energy loss per turn | 363.8 keV |
| Bare lattice natural energy spread $\sigma_\delta$ | $0.769\times10^{-3}$ |
| Bare lattice horizontal damping time $\tau_x$ | 15.725 ms |
| Bare lattice vertical damping time $\tau_y$ | 29.047 ms |
| Bare lattice longitudinal damping time $\tau_E$ | 25.194 ms |
| Horizontal beta function at center of LS $\beta_x^*$ (bare lattice) | 9.00 m |
| Vertical beta function at center of LS $\beta_y^*$ (bare lattice) | 2.00 m |

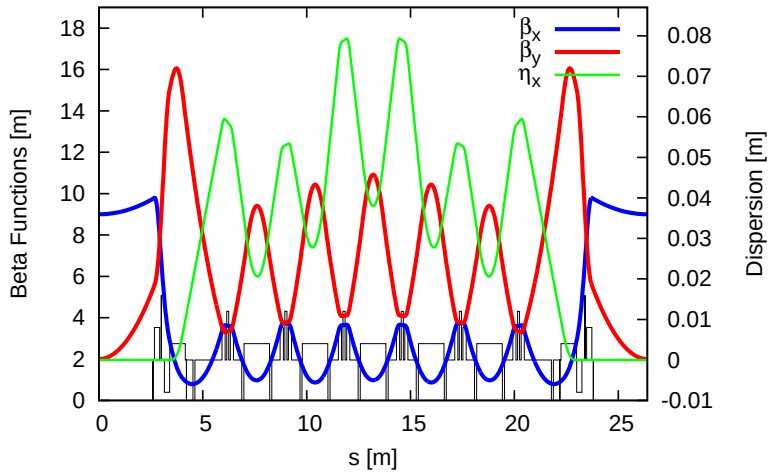


Figure 2: The updated optics in one of the 20 MBAs of the MAX IV 3 GeV storage ring. The magnetic structure is indicated at the bottom.

# 3 Changes to the Nonlinear Optics

The small changes in the linear optics of the updated lattice have resulted in slightly different natural chromaticities. Therefore an update of the nonlinear optics was required. The targets of the previous nonlinear optimization process (420 nonlinear optics branch) have, however, been retained. Updated gradients for the sextupoles and octupoles have been derived in order to achieve those goals. These revised settings make up the 430 nonlinear optics branch. The sextupole gradient changes required for the 430 branch are detailed in Table 5.

Table 5: List of sextupole gradient changes by magnet family.

| Magnet family | Sextupole gradient change | Rel. difference |
|---|---|---|
| SD | $b_3 = -116.414\,\mathrm{m}^{-3} \longrightarrow -116.625\,\mathrm{m}^{-3}$ | +0.18% |
| SDend | $b_3 = -170.000\,\mathrm{m}^{-3} \longrightarrow -170.000\,\mathrm{m}^{-3}$ | n/a |
| SFm | $b_3 = 170.000\,\mathrm{m}^{-3} \longrightarrow 170.000\,\mathrm{m}^{-3}$ | n/a |
| SFo | $b_3 = 174.000\,\mathrm{m}^{-3} \longrightarrow 174.000\,\mathrm{m}^{-3}$ | n/a |
| SFi | $b_3 = 206.707\,\mathrm{m}^{-3} \longrightarrow 207.412\,\mathrm{m}^{-3}$ | +0.34% |

Likewise, octupole gradients were derived in order to satisfy the previous linear amplitude-dependent tune shift terms $\partial\nu_x/\partial J_x = -2500$, $\partial\nu_x/\partial J_y = \partial\nu_y/\partial J_x = 2300$, and $\partial\nu_y/\partial J_y = 3500$. The octupole gradient changes required for the 430 branch are listed in Table 6.

Table 6: List of octupole gradient changes by magnet family.

| Magnet family | Octupole gradient change | Rel. difference |
|---|---|---|
| OXX | $b_4 = -1618.31\,\mathrm{m}^{-4} \longrightarrow -1648.58\,\mathrm{m}^{-4}$ | +1.87% |
| OXY | $b_4 = 3250.19\,\mathrm{m}^{-4} \longrightarrow 3270.14\,\mathrm{m}^{-4}$ | +0.61% |
| OYY | $b_4 = -1416.59\,\mathrm{m}^{-4} \longrightarrow -1420.22\,\mathrm{m}^{-4}$ | +0.26% |

With these modifications to the nonlinear optics, the 430 branch shows a very similar chromatic and amplitude-dependent behavior as the previous 420 branch. The chromaticity is displayed in Fig. 3, while amplitude-dependent tune shifts are shown in Fig. 4. Overall, these tune shifts result in a very compact tune footprint (cf. Fig. 5) over the entire physical acceptance as well as the entire RF acceptance.

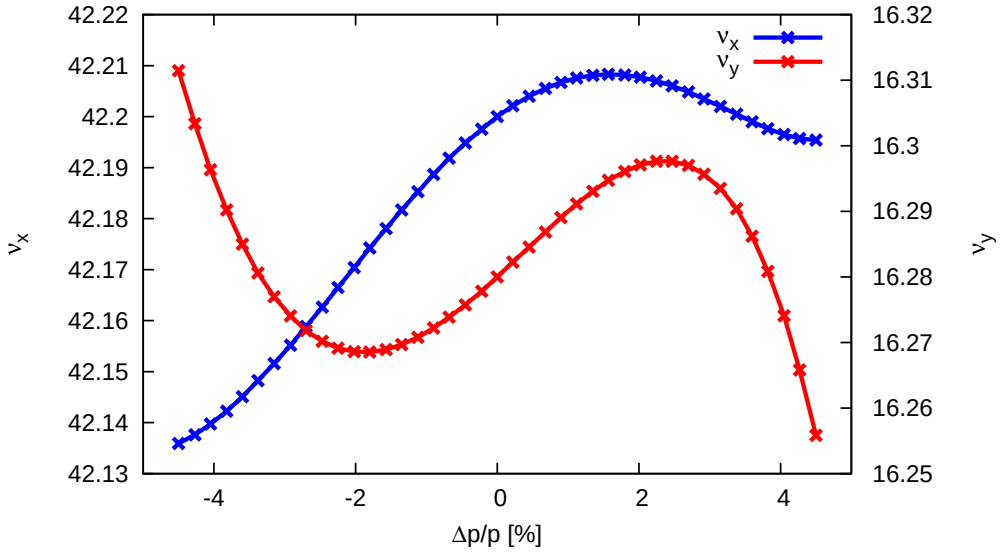


Figure 3: Chromaticity calculated by TRACY-3 using the new optics. The range chosen corresponds to the required MA of the ring.

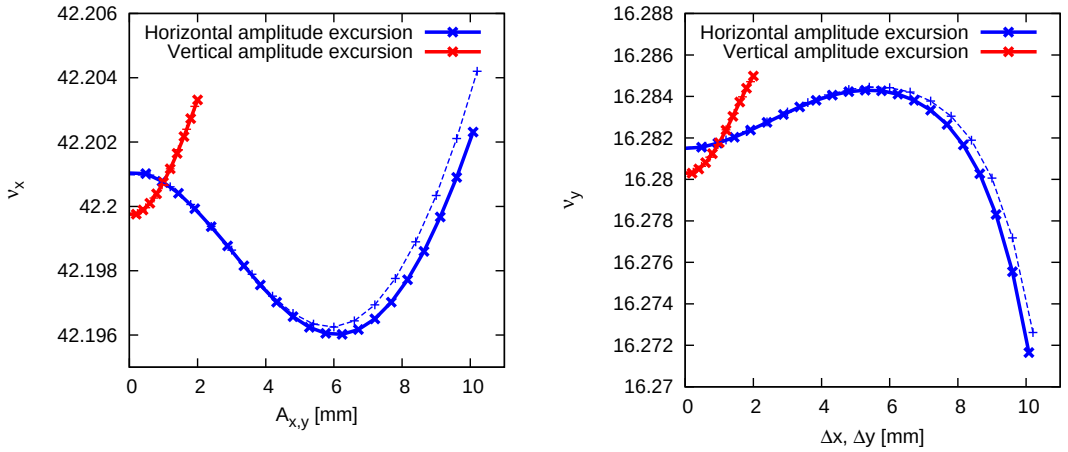


Figure 4: Amplitude-dependent tune shift calculated by TRACY-3 using the new optics. The range chosen corresponds to the required apertures of the ring. Dashed lines correspond to the previous lattice m4-20110117-420-bare.

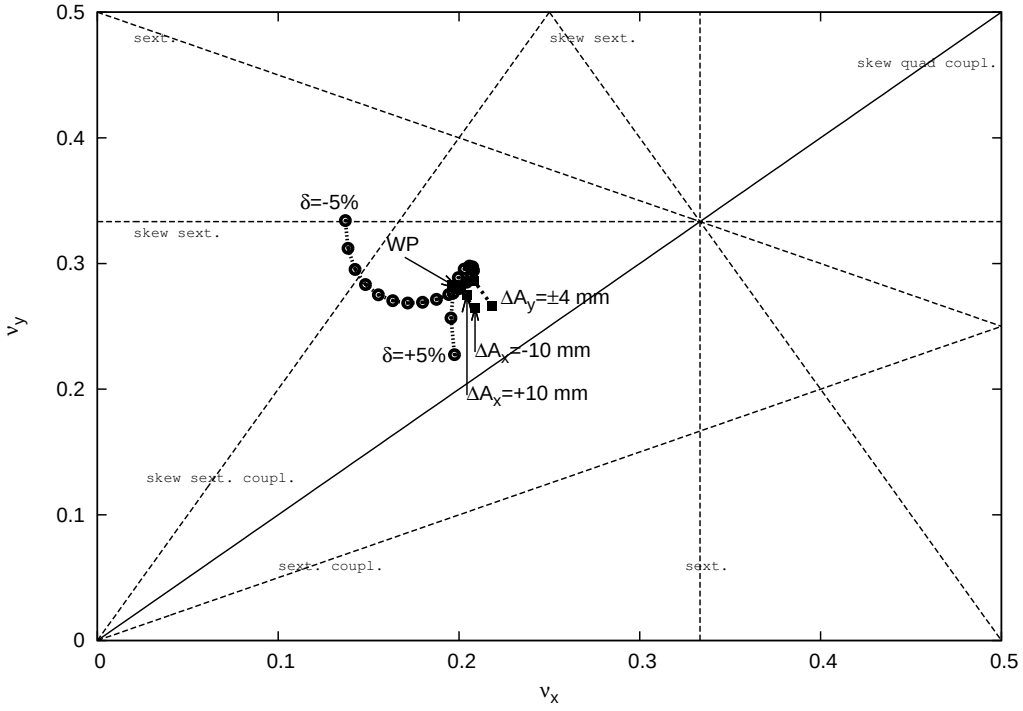


Figure 5: A plot of fractional tune space for the MAX IV 3 GeV storage ring bare lattice as calculated by OPA. Resonance and skew resonance lines have been included up to third order. WP indicates the working point. The step size chosen for the chromatic tune shift is 0.5% and 2.5 mm [1.0 mm] for the horizontal [vertical] amplitude-dependent tune shift.

The result of this small tune footprint is reflected by the large DA (cf. Figs. 6 and 7) as well as large MA (cf. Fig. 8). The diffusion maps confirm the DA results. Within the DA, there is a large area of only low diffusion. Within the required aperture, there is virtually no diffusion at all.

Four bands can be recognized within the required $\pm 4.5\%$ MA: the band around $\delta = -2.5\%$ is caused by $6\nu_x = 253$, while the skew octupole resonance $2\nu_x + 2\nu_y = 117$ is the cause of the two lighter bands around $\delta = +1.3\%$ and $\delta = +2.5\%$. Finally, the band around $\delta = +4.5\%$ is caused by $4\nu_y = 65$. None of these resonances are expected to be driven strongly in a well-aligned and corrected machine.

Overall, DA and FMA for the new 430 nonlinear optics branch show hardly any perceivable differences compared to the previous 420 branch. This is, however, not surprising, considering that there is no difference in chromatic tune shift and hardly any difference in amplitude-dependent tune shift compared to the previous

420 nonlinear optics branch.

The similar MA is further corroborated by the Touschek lifetime. OPA estimates for dynamic Touschek lifetime (bare lattice, no Landau cavities, 2.5% emittance coupling, 1.8 MV total cavity voltage $\rightarrow$ $\delta_{\mathrm{rf}} = 7.062\%$, 500 mA stored current, IBS neglected) show 31.03 hours, compared to the 30.94 hours observed with the previous lattice m4-20110117-420-bare.

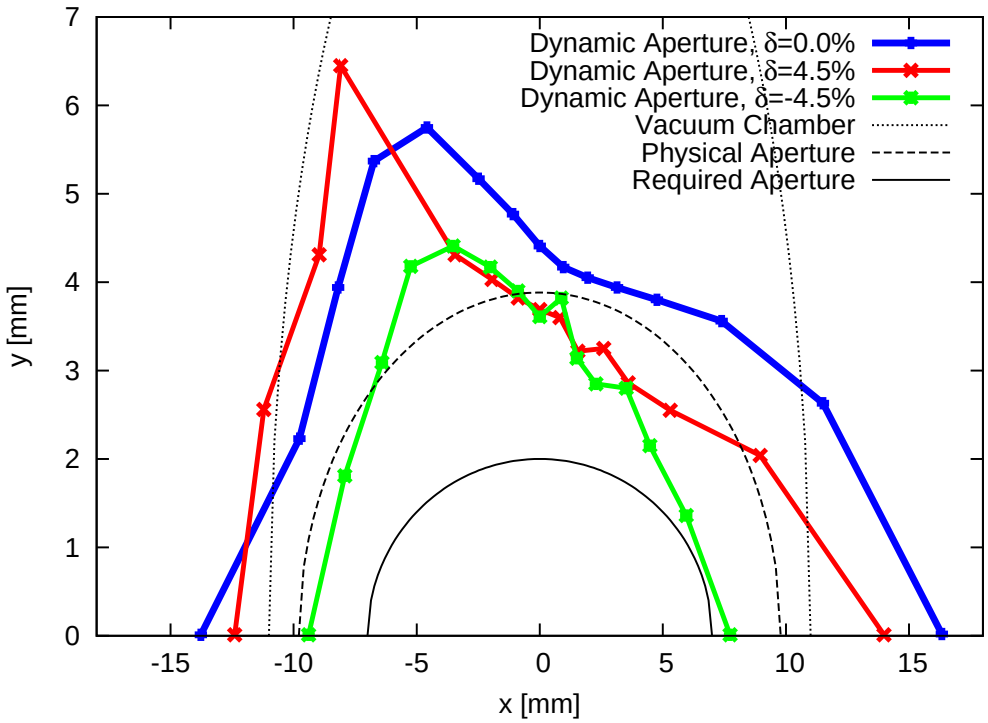


Figure 6: Dynamic aperture at the center of the long straight section in the MAX IV 3 GeV storage ring (bare lattice). Tracking was performed with TRACY-3 in 6D for half a synchrotron period. Physical aperture and required aperture (determined by the injection process and lifetime concerns) are also indicated in the plot.

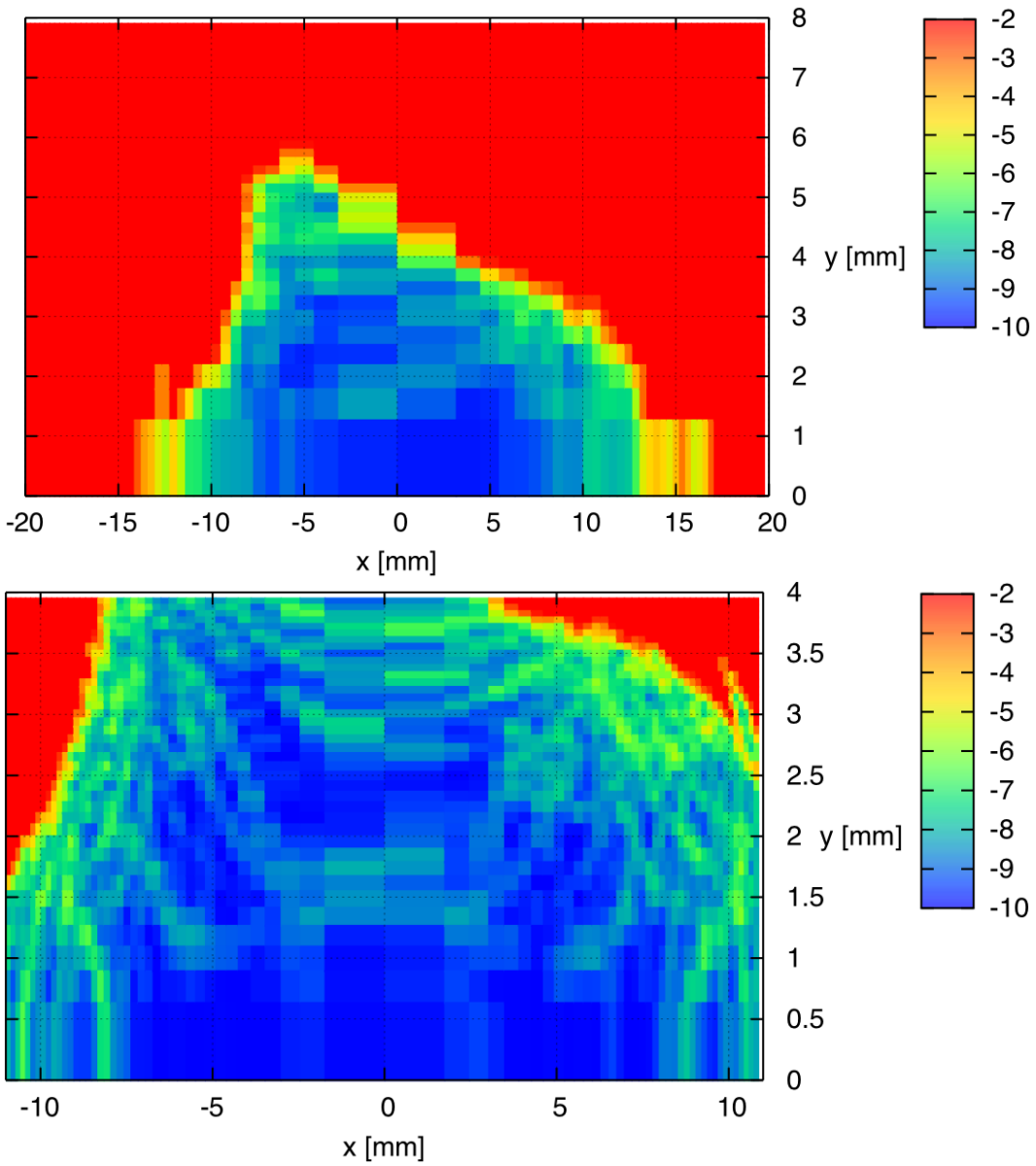


Figure 7: Diffusion maps for the MAX IV 3 GeV storage ring bare lattice taken at the center of the straight section (physical acceptance at this location is $\pm 10.5\,\text{mm} \times \pm 3.9\,\text{mm}$). The lower plot is a magnification of the core area of the upper plot. Blue areas show small tune shifts, red areas show large tune shifts and particle loss. The plots have been generated with TRACY-3 by scanning transverse configuration space on-momentum and tracking for 2048 turns.

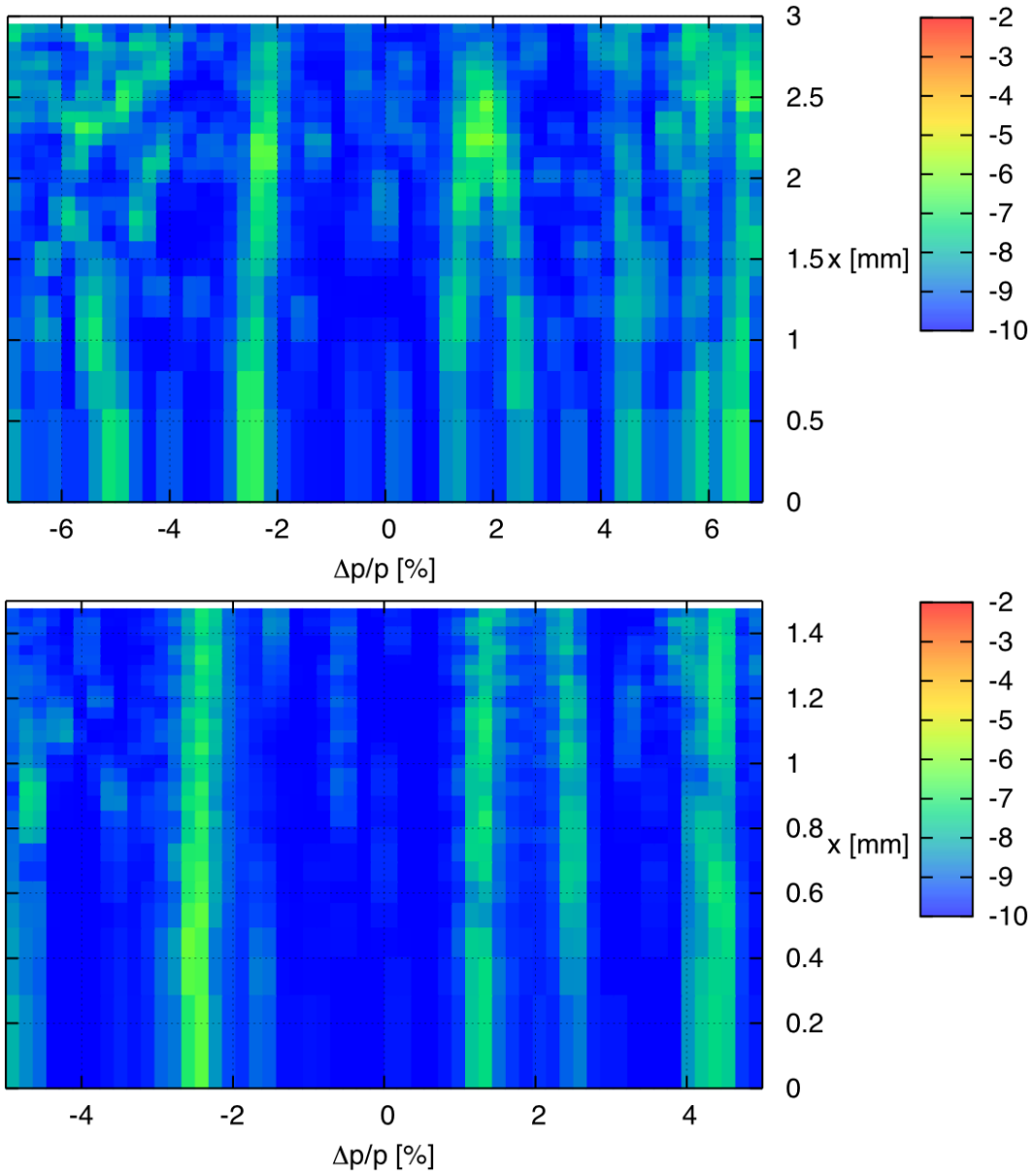


Figure 8: Diffusion maps for the MAX IV 3 GeV storage ring bare lattice taken at the center of the straight section for off-momentum particles. The lower plot is a magnification of the core area of the upper plot. Blue areas show small tune shifts, red areas show large tune shifts and particle loss. The plots have been generated with TRACY-3 by scanning the horizontal coordinate and momenta and tracking for 2048 turns. The initial vertical amplitude was +1 mm.

# 4 Expected Performance of the New Lattice

This section attempts to give performance estimates for the new lattice in a realistic environment, e.g. a situation where the lattice is subjected to all kinds of random and systematic imperfections: alignment errors, field errors, and multipole errors. After a brief introduction of the various error models, the effect of errors on dynamic aperture (which determines injection/capture efficiency as well as Touschek lifetime) of the new lattice is investigated. This is followed by a section dedicated to investigating closed orbits, coupling, and orbit correction (slow orbit correction, i.e. correction of static errors and slow drifts as usually performed by a slow orbit feedback). Finally, the last section deals with emittance — both with and without the effect of intrabeam scattering (IBS) — and expected Touschek lifetime.

## 4.1 Error Models

This section summarizes the errors models used when studying the lattice with imperfections. The models are similar to those presented in the DDR [5], but a few parameters have been modified to better model expected imperfections. The first section briefly introduces systematic errors and their effect on lattice optics. This is followed by a section listing the various random field errors and the multipole errors. Finally, an overview of the alignment errors is given.

### 4.1.1 Systematic Field Errors

Systematic field errors beyond magnet manufacturing errors (which are assumed to be compensated for by shunts) have to be considered since they are caused by commonly present sources such as power supply ripple. Since only some magnets within a family are usually connected to a common power supply, the effect of these imperfections on optics depends not only on the type of field, but also on the number of power supplies and magnets within a family as well as how these magnets are connected to the power supply.

The analytic estimates performed in DDR Section 2.4.2.1 [5] remain mostly valid since overall optics changes since these studies have remained small. A brief summary of these systematic errors and their effect:

**Systematic quadrupole errors:**

- 8 QF magnets connected in series to a single power supply; 20 power supplies with $10^{-4}$ ripple.

- 4 QFm magnets connected in series to a single power supply; 20 power supplies with $10^{-4}$ ripple.
- 2 QFend magnets connected in series to a single power supply; 20 power supplies with $10^{-4}$ ripple.
- 2 QDend magnets connected in series to a single power supply; 20 power supplies with $10^{-4}$ ripple.
- 100 DIP PFSs connected in series to a single power supply; power supply with $10^{-3}$ ripple.
- 40 DIPm PFSs connected in series to a single power supply; power supply with $10^{-3}$ ripple.

$\rightarrow$ Results in tune jitter in both planes $< 0.001$.

**Systematic sextupole errors:**

- 2 SFi magnets connected in series to a single power supply; 20 power supplies with $10^{-4}$ ripple.
- 2 SFo magnets connected in series to a single power supply; 20 power supplies with $10^{-4}$ ripple.
- 2 SFm magnets connected in series to a single power supply; 20 power supplies with $10^{-4}$ ripple.
- 10 SD magnets connected in series to a single power supply; 20 power supplies with $10^{-4}$ ripple.
- 2 SDend magnets connected in series to a single power supply; 20 power supplies with $10^{-4}$ ripple.

$\rightarrow$ Results in chromaticity jitter in both planes $< 0.003$; overall $\Delta(b_3 L)/(b_3 L) = 0.005$.

**Systematic octupole errors:**

- 38 OXX magnets connected in series to a single power supply; power supply with $10^{-4}$ ripple.
- 2 OXX magnets connected in series to a single power supply; power supply with $10^{-4}$ ripple.
- 38 OXY magnets connected in series to a single power supply; power supply with $10^{-4}$ ripple.
- 2 OXY magnets connected in series to a single power supply; power supply with $10^{-4}$ ripple.

- 40 OYY magnets connected in series to a single power supply; power supply with $10^{-4}$ ripple.

→ Results in overall $\Delta(b_4 L)/(b_4 L) = 0.007$.

### 4.1.2 Field and Multipole Errors

The following random field errors as well as random and systematic multipole errors have been included in the magnet error model.

- Field errors are assumed to be Gaussian with 0.05% RMS and a cut-off at $2\sigma$ (an attempt to model the 20 $\mu$m peak-to-peak machining accuracy we expect from magnet manufacturing in combination with the typical magnet bore of 25 mm.). These errors have been applied to all dipoles (gradient errors, not bending angle errors)[2], quadrupoles, sextupoles, and octupoles.
- The shunting strategy presented in DDR Section 2.4.2.1.4 [5] remains valid for dipoles and quadrupoles, although the exact figures have been modified. Initially, magnets within a family will be shunted after manufacturing according to magnet measurements in order to ensure quadrupole gradient variation across a family remains below 0.1% RMS; this is referred to as "coarse shunting". In the assembled machine and once beam can be stored in the ring, beam-based measurements (e.g. LOCO [6]) can reveal remaining quadrupole gradient errors in magnets within the same family. As a consequence of such measurements, a second shunting stage can be performed (the "fine shunting") with the goal to push RMS gradient variations within magnet families to below 0.05% RMS.

Apart from such field errors, what remains are multipole errors in all magnets.

- Multipole errors have been modeled similar to what was detailed in the DDR. Both systematic and random multipole errors for upright as well as skew multipoles have been included.
- The original multipole model made use of unscaled BINP measurement data taken with SLS magnets. This was a pessimistic model as it took multipole errors with a reference radius of 28 mm used for the SLS magnets and applied

[2] Actually, gradient errors are applied to individual dipole slices, not the entire dipole magnet. Since these errors are defined as RMS values of a Gaussian distribution with a certain cut-off, applying this error model to the dipole slices rather than the entire dipole is unphysical. However, it results as a direct consequence of the slice model used in the lattice. Towards the end of Section 4.2 this issue is re-examined by comparison with a simplified lattice without dipole slicing.

them to the MAX IV magnets assuming a reference radius of 11 mm (the usual vacuum aperture). Hence, the MAX IV multipole errors were being systematically over-estimated. It was, however, at the time considered prudent to make a somewhat more pessimistic assumption, since the MAX IV magnets are machined from common yokes and separation between individual magnets is very narrow.

- In the refined model, these errors have been properly scaled to the MAX IV magnets. However, comparisons have revealed only very small differences in dynamic aperture as a result of the proper multipole scaling. Differences became larger when comparing to a preliminary model using systematic multipoles as derived from 3D quadrupole models [9]: dynamic aperture actually increased when using these systematic multipoles in the quadrupoles compared to the previous multipole models. Overall DA remains to be dominated by misalignment errors (cf. Section 4.2 below); for DA studies using multipole errors alone, results can be considered somewhat pessimistic, but not unrealistically so.

### 4.1.3 Alignment Errors

The standard alignment error model is set up as follows:

- Misalignments are applied to entire magnet blocks (girder misalignments) as well as individual magnets within blocks. The misalignment within the block is added on top of the misalignment of the entire block.
- Misalignments are assumed to be Gaussian with a cut-off at $2\sigma$.
- All magnet blocks ("girders") are assumed to be misaligned transversely by $50\,\mu$m RMS[3]; their roll error is expected to be 0.2 mrad RMS.
- Dipoles[4] are assumed to be misaligned transversely by $25\,\mu$m RMS; their roll error is expected to be 0.2 mrad RMS.
- Quadrupoles are assumed to be misaligned transversely by $25\,\mu$m RMS; their roll error is expected to be 0.2 mrad RMS.

[3]This is an attempt to model the absolute alignment tolerance specified as better than $100\,\mu$m for neighboring blocks.

[4]Actually, the misalignments are applied to individual dipole slices, not the entire dipole magnet. This is unphysical, but since TRACY-3 does not have support for nested girders, this is the only way to model dipole misalignments short of abandoning the slice model entirely. Towards the end of Section 4.2 this issue is re-examined by comparison with a simplified lattice without dipole slicing.

- Sextupoles are assumed to be misaligned transversely by 25 $\mu$m RMS; their roll error is expected to be 0.2 mrad RMS.
- Octupoles are assumed to be misaligned transversely by 25 $\mu$m RMS; their roll error is expected to be 0.2 mrad RMS.
- Orbit correctors (dipole correctors) are assumed to be misaligned transversely by 25 $\mu$m RMS; their roll error is expected to be 0.2 mrad RMS.
- BPMs are assumed to be misaligned transversely by 3 $\mu$m RMS; their roll error is expected to be 0.1 mrad RMS. This is an attempt to model repeatability/accuracy of the beam-based BPM calibration.

Sextupole and quadrupole rolls have been increased in studies in order to derive specifications for assembly tolerances. As long as quadrupole and sextupole rolls remain below 0.5 mrad RMS, the DA remains almost unchanged while emittance coupling and beam tilt (after orbit correction) are not significantly higher than in cases where the standard misalignment model is used (cf. Section 4.3).

## 4.2 Dynamic Aperture Studies

On and off-momentum dynamic aperture of the bare lattice allows studying the influence of the various error sources detailed above. A first example is given in Fig. 9 where multipole errors and field errors as detailed above have been included and the DA has been calculated on and off-momentum for 20 error seeds. By comparison with a situation where only field errors have been included (cf. Fig. 10) it can be concluded that at this level, DA reduction is dominated by field errors, not multipole errors. The primary cause of the DA reduction from field errors is gradient errors in the dipoles. This can be recognized by comparing Fig. 11, where only dipole gradient errors have been included, to Figs. 9 or 10. Although quadrupole, sextupole, and octupole field errors all lead to a slight reduction of DA, the overall effect is comparable to that of multipole errors, and thus presents a small effect compared to the major contribution to DA reduction caused by dipole gradient errors.

In terms of beta beat, the average (across seeds) of the RMS beta beat is 1.2% (H) and 4.3% (V) for the data shown in Figs. 9 and 10. For the data shown in Fig. 11 it is 0.5% (H) and 4.0% (V).

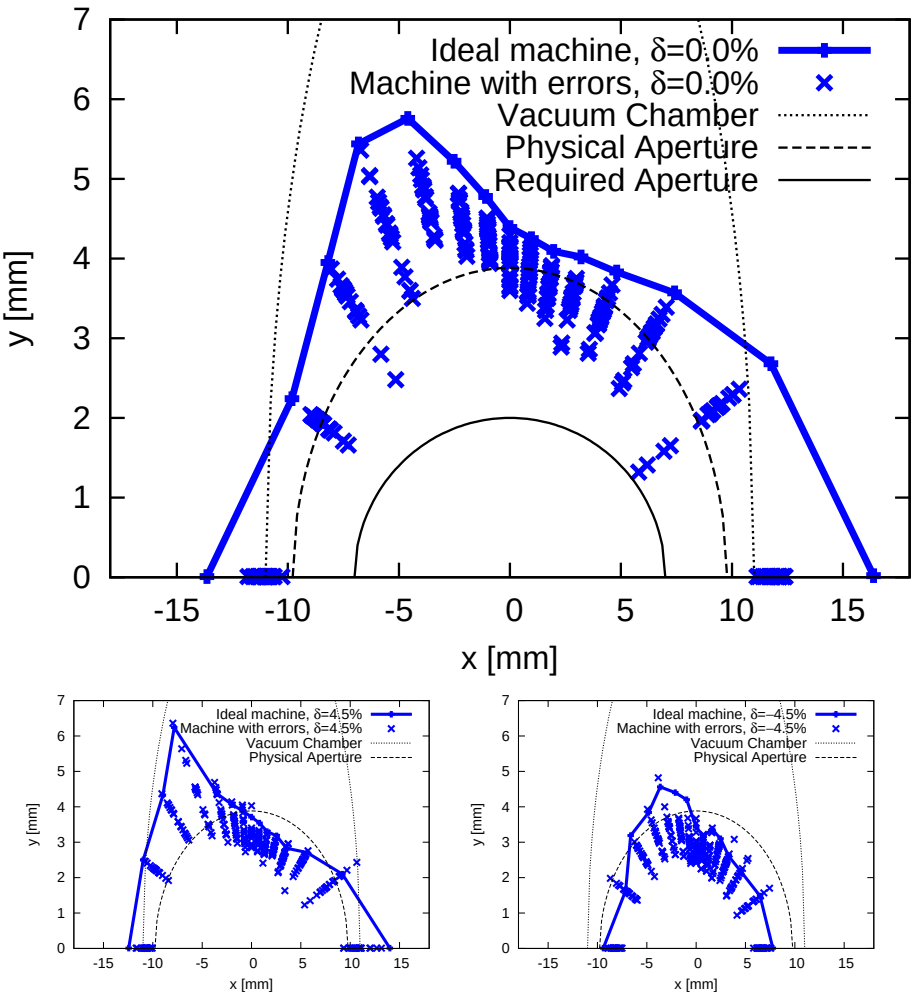


Figure 9: Dynamic aperture at the center of the long straight section in the MAX IV 3 GeV storage ring (bare lattice) from tracking with TRACY-3. The plots show the ideal lattice and results for 20 seeds with field and multipole errors.

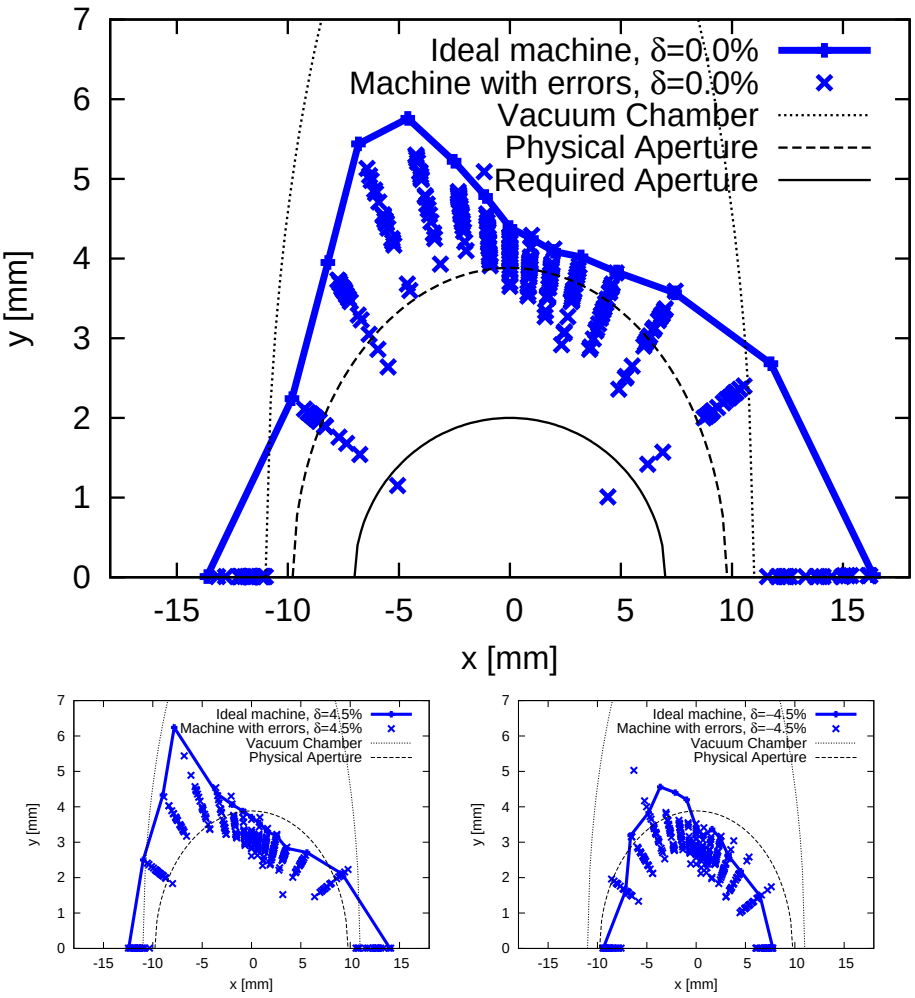


Figure 10: Dynamic aperture at the center of the long straight section in the MAX IV 3 GeV storage ring (bare lattice) from tracking with TRACY-3. The plots show the ideal lattice and results for 20 seeds with field errors only.

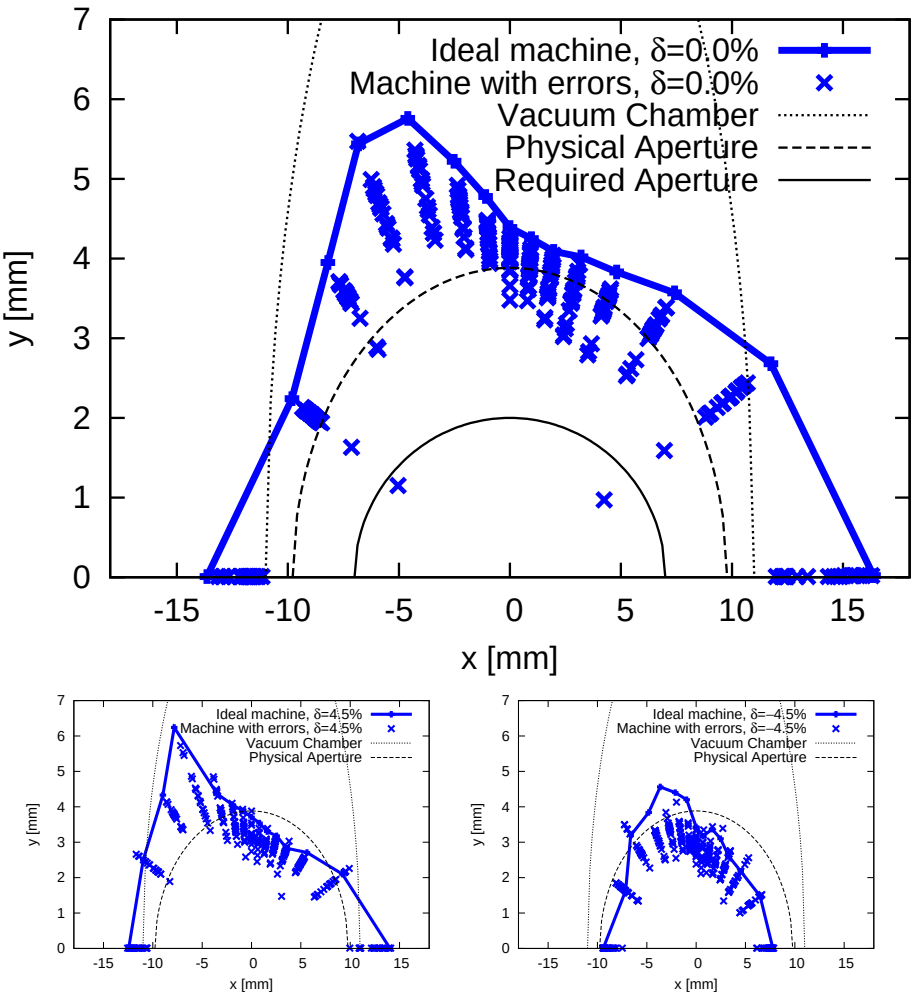


Figure 11: Dynamic aperture at the center of the long straight section in the MAX IV 3 GeV storage ring (bare lattice) from tracking with TRACY-3. The plots show the ideal lattice and results for 20 seeds with dipole gradient errors only.

Alignment errors will also lead to a reduction of DA, despite orbit correction efforts (cf. Section 4.3) which will attempt to correct the orbit to the BPM centers (which in turn have been calibrated so as to minimize the orbit in the adjacent SFi/o/m, SDend, and OXX magnets)[5]. A first example is shown in Fig. 12 where the DA has been calculated on and off-momentum for 20 seeds with alignment errors as detailed above after the orbit has been corrected. For this case the average RMS beta beat is 1.6% (H) and 4.3% (V). The results show that these alignment errors lead to a more severe reduction of DA than that observed from field and multipole errors (cf. Fig. 9).

If, however, the alignment errors of the magnet blocks are halved (i.e. 25 $\mu$m RMS transverse misalignment, 0.1 mrad RMS roll error), the resulting level of DA reduction (cf. Fig. 13) becomes comparable to that observed from field and multipole errors alone (cf. Fig. 9). The beta beat (after orbit correction) is reduced to 1.4% (H) and 3.1% (V).

[5]Note that this describes the actual procedure in a real storage ring. It is, however, not exactly the same procedure that is used in TRACY-3. As will be explained more thoroughly in Section 4.3, TRACY-3 orbit correction attempts to correct towards the ideal orbit. This ideal orbit does not exist in a real machine (as there is no way of detecting it) and doesn't necessarily have to coincide with the BPM centers either. It is, however, the BPM centers which—in the real machine—are used to define a "design orbit" or "golden orbit" towards which the orbit is corrected. A more in-depth analysis of the issue can be found in [10].

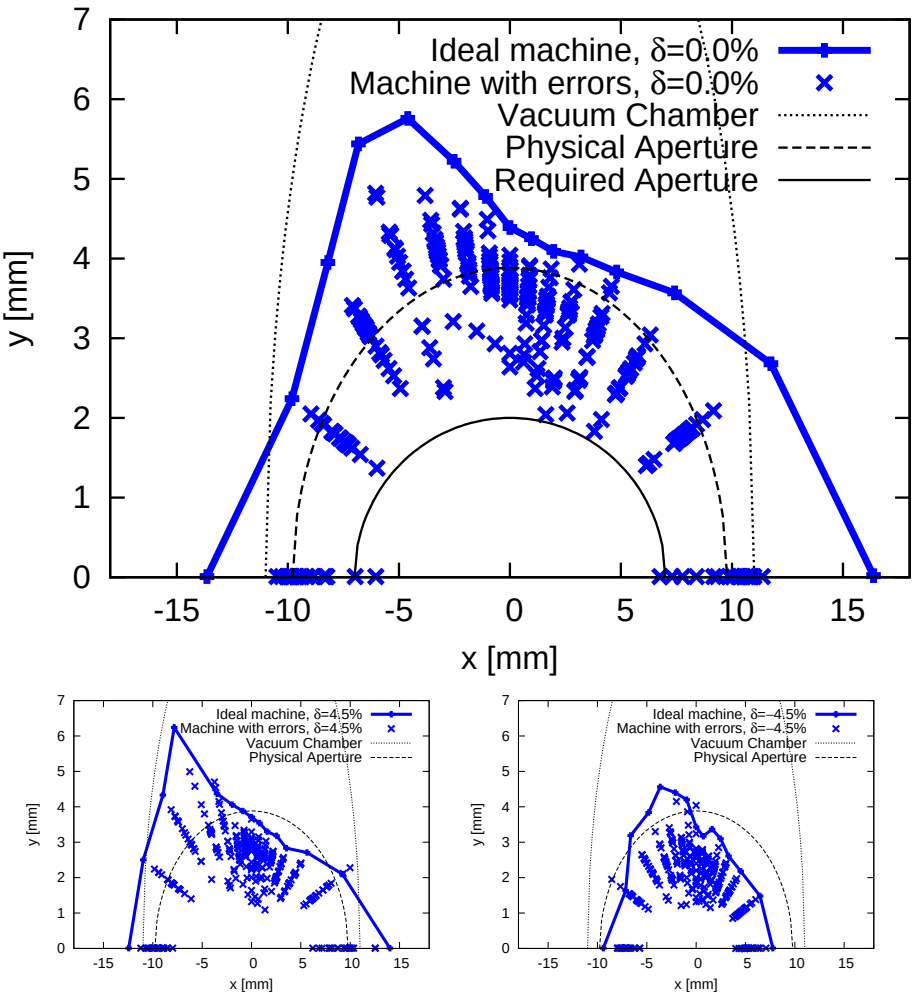


Figure 12: Dynamic aperture at the center of the long straight section in the MAX IV 3 GeV storage ring (bare lattice) from tracking with TRACY-3. The plots show the ideal lattice and results for 20 seeds with alignment errors only.

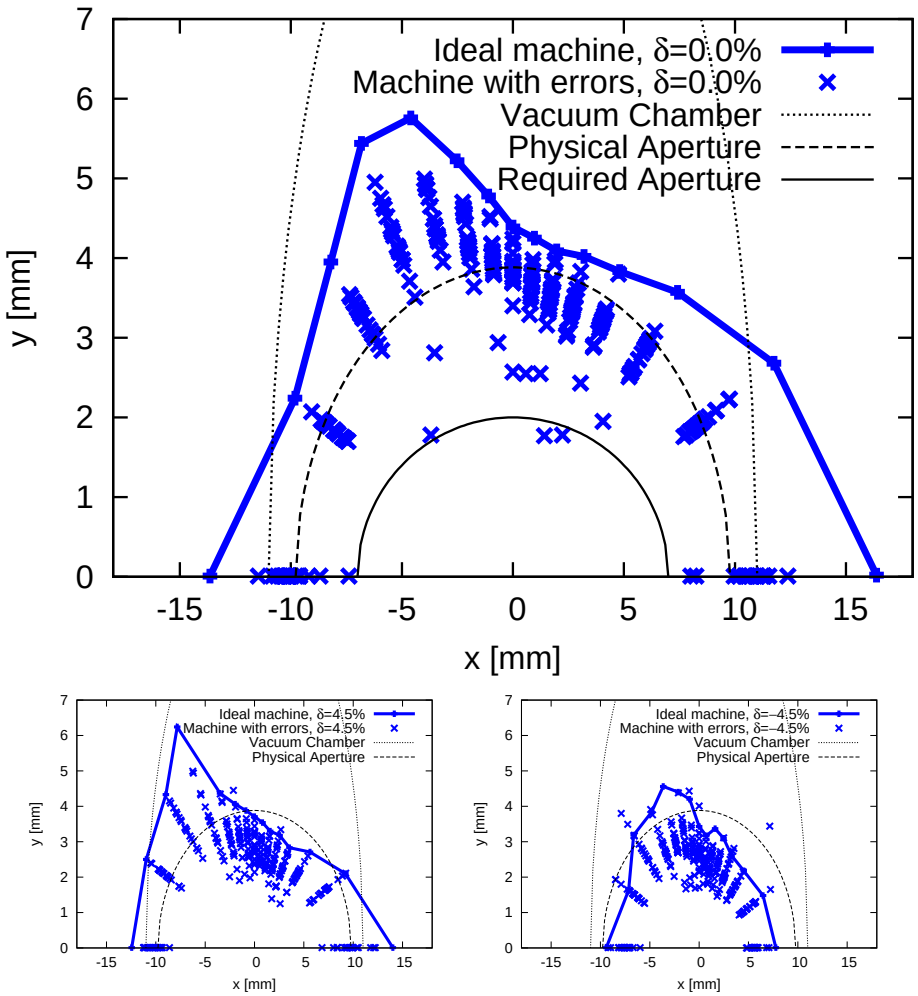


Figure 13: Dynamic aperture at the center of the long straight section in the MAX IV 3 GeV storage ring (bare lattice) from tracking with TRACY-3. The plots show the ideal lattice and results for 20 seeds with alignment errors only. In the alignment error model, the alignment errors of the magnet blocks have been reduced to half their originally assumed value.

Ultimately, these error sources will act together, i.e. DA reduction will be an overall result of a combination of all these error sources. Figure 14 is an attempt at modeling this situation: field, multipole, and alignment errors according to the models detailed above have all been included and the resulting DA reduction calculated (after orbit correction). The resulting situation, although not entirely unworkable, shows that several seeds do in fact infringe on required aperture. Such a situation would result in either limited capture efficiency and/or reduced momentum acceptance leading to reduced Touschek lifetime. The average beta beat for this case is 2.1% (H) and 6.6% (V).

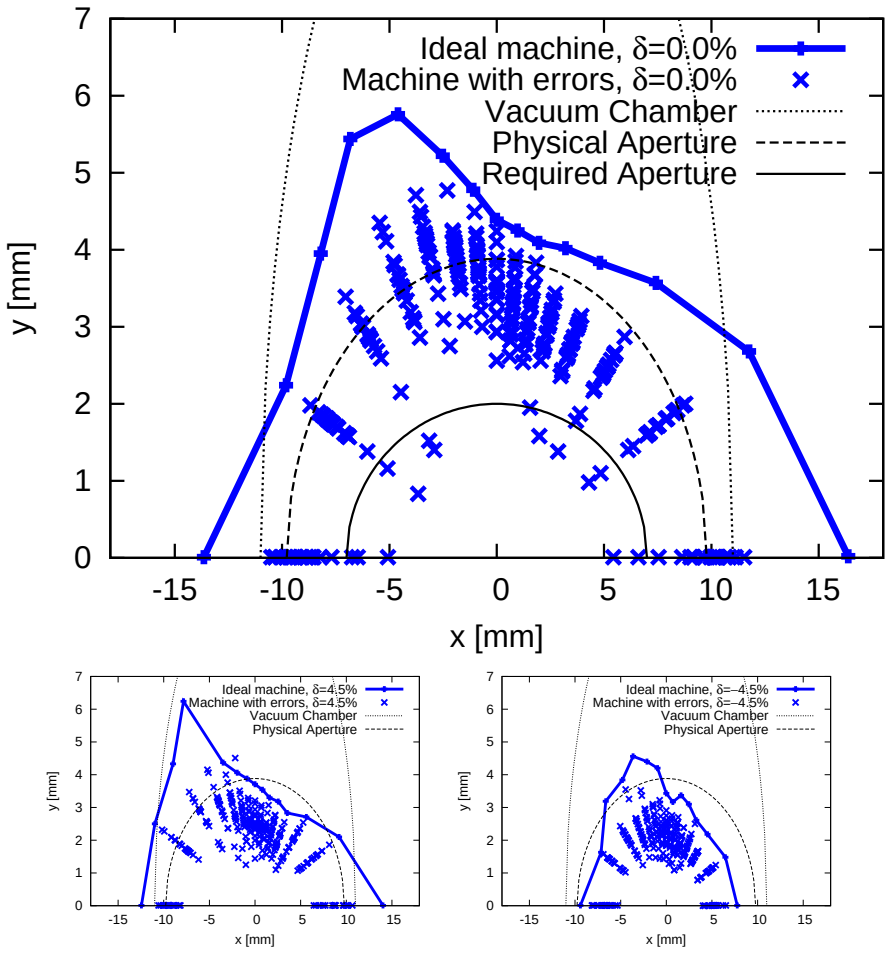


Figure 14: Dynamic aperture at the center of the long straight section in the MAX IV 3 GeV storage ring (bare lattice) from tracking with TRACY-3. The plots show the ideal lattice and results for 20 seeds with field, multipole, and alignment errors.

This situation can be improved, however. If the alignment of the magnet blocks is improved, the overall DA reduction becomes less severe even when all error sources are combined. In Fig. 15 a situation has been investigated where field, multipole, and alignment errors have all been included, however, in the alignment error model the magnet block misalignments have been reduced to half their originally assumed value (i.e. 25 $\mu$m RMS transverse misalignment, 0.1 mrad RMS roll error). The result is a much better DA and a reduced beta beat: 1.9% (H) and 5.6% (V). In such a situation high capture efficiency and good lifetime should be achieved. This situation corresponds to what can be expected during regular user operation once re-alignment of the storage ring has been successful and after "fine shunting" has been performed as a result of beam-based studies (e.g. LOCO).

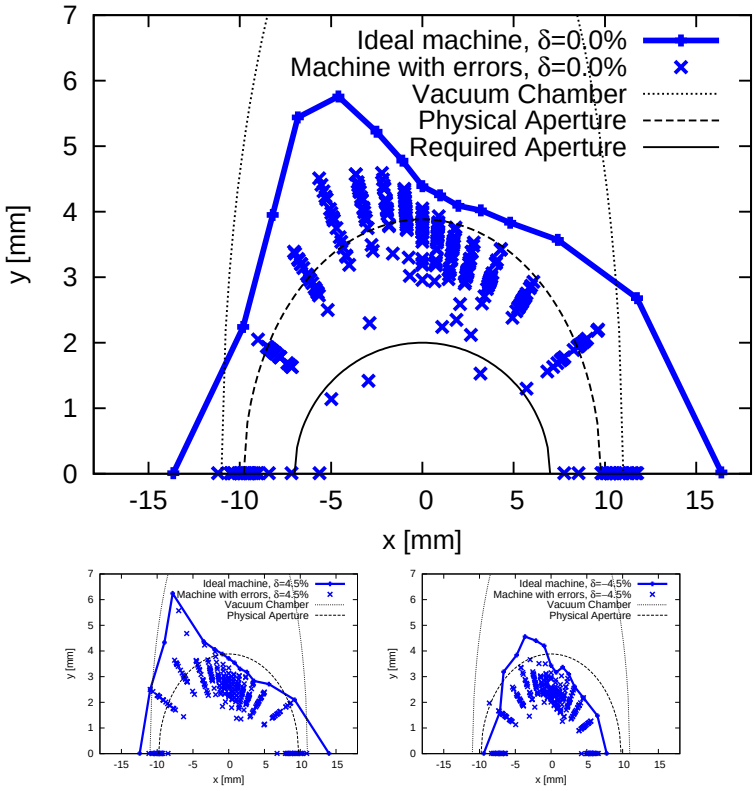


Figure 15: Dynamic aperture at the center of the long straight section in the MAX IV 3 GeV storage ring (bare lattice) from tracking with TRACY-3. The plots show the ideal lattice and results for 20 seeds with field, multipole, and alignment errors. In the alignment error model, the alignment errors of the magnet blocks have been reduced to half their originally assumed value.

It has already been stated that field errors on the order of 0.05% RMS are expected to result from "fine shunting" according to the outcome of LOCO studies. But since LOCO can only be performed with stored beam and finite lifetime, it first needs to be verified that beam can be stored even in the presence of field errors on the order of 0.1% RMS as expected as a result of "coarse shunting" after manufacturing according to magnet measurement data. Figure 16 shows DA reduction from field, multipole, and alignment errors where field errors with 0.1% RMS have been assumed. It can be directly compared to Fig. 14. The reduction of DA is clearly more severe as a consequence of the increased beta beat (3.0% in the horizontal and 10.5% in the vertical), however, despite the reduced DA, storing beam with finite lifetime should still be possible. LOCO can then be performed in order to improve the shunting, arrive at a smaller field error variation and hence at the improved DA.

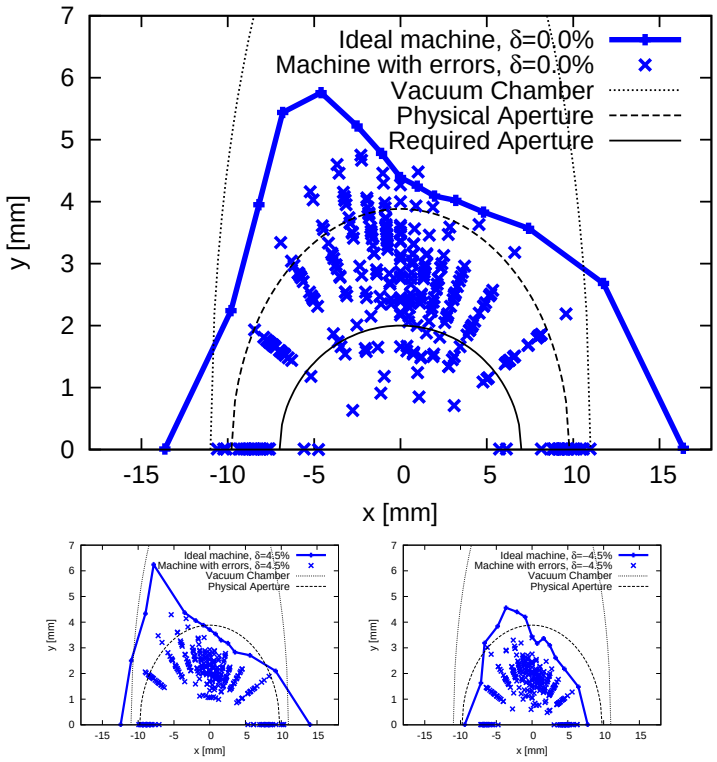


Figure 16: Dynamic aperture at the center of the long straight section in the MAX IV 3 GeV storage ring (bare lattice) from tracking with TRACY-3. The plots show the ideal lattice and results for 20 seeds with field, multipole, and alignment errors. The field errors have been increased to 0.1% RMS.

But actually, when the commissioning starts, the situation could be worse yet. Not only must field errors on a 0.1% RMS level be expected from "coarse shunting", initial alignment could also be poorer than desired. Alignment can be improved by inspection of the corrector pattern and subsequent re-alignment, but initially, beam needs to be stored in a possibly more severely misalignment machine so that corrector patterns can be derived and analyzed in the first place. Figure 17 shows a situation that attempts to model this "initial commissioning scenario": the girders have been misaligned by twice their originally assumed value (i.e. 100 $\mu$m RMS transverse misalignment, 0.4 mrad RMS roll error) and the field errors have been modeled with 0.1% RMS. This leads to rather large beta beat (3.4% in the horizontal and 12.7% in the vertical) and consequently the reduction of DA is quite severe (capture efficiency as well as momentum acceptance will most likely be restricted). However, despite the reduced DA, storing beam with finite lifetime should be possible. At this point the corrector pattern can be used to determine the worst misalignments and re-align the machine (leading to a situation similar to what is depicted in Fig. 16). Once this has been carried out successfully, LOCO can then be performed in order to improve the shunting, arrive at a smaller field error variation and hence at the improved DA (ideally such as depicted in Fig. 15).

It is important to note that the assumed alignment errors dominate the DA reduction compared to field and multipole errors at the originally expected levels. However, it is equally important to notice that field errors need to be better than 0.1% RMS in order to achieve good DA. No amount of re-alignment can restore the collapsed DA that results from severe field errors (mainly quadrupole gradient errors in the dipoles and quadrupoles). A consequence of this is that there exists a clear commissioning strategy: start up with field errors not above the 0.1% RMS level as a result of decent-quality "coarse shunting" at the factory, align the machine as well as possible (maintaining that neighboring girders are aligned to within 100 $\mu$m of each other) in order to enable decent capture as well as good enough lifetime so that LOCO studies can be carried out successfully. Once small amounts of beam can be stored for sufficiently long time, beam-based measurements will reveal crude misalignments and/or field errors, so that the "fine shunting" can be performed and/or the machine can be re-aligned leading ultimately to the desired DA.

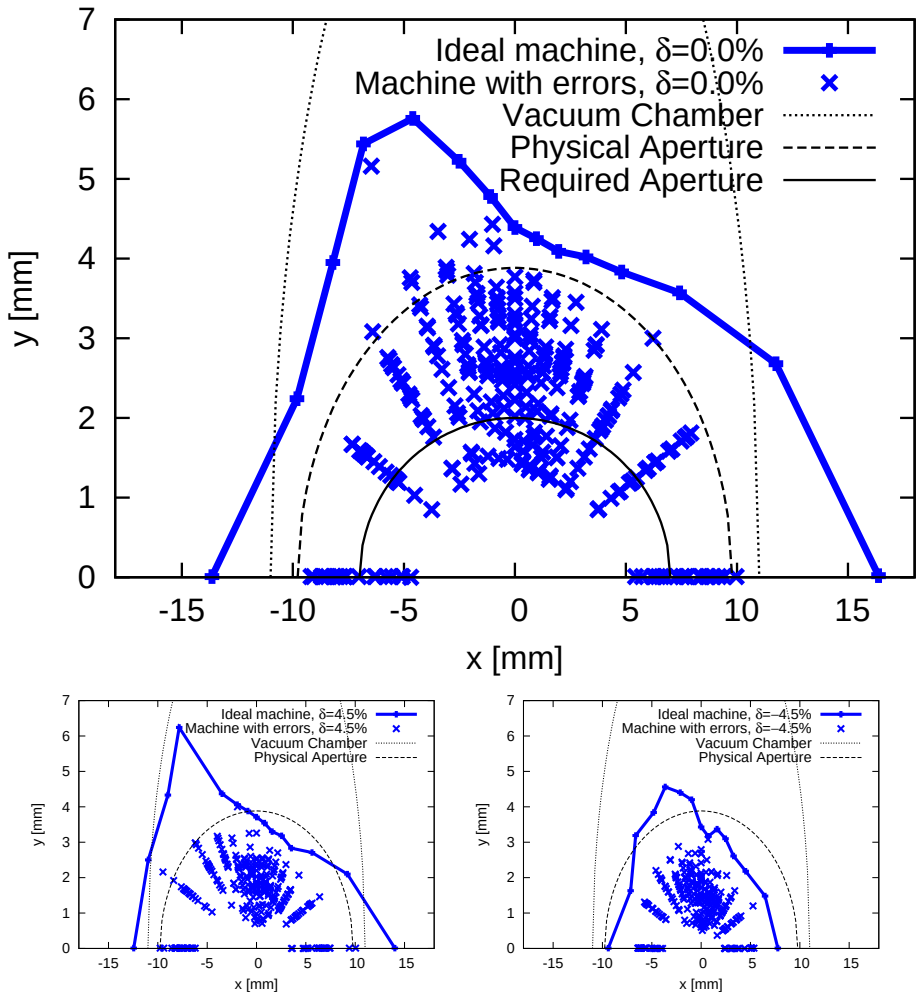


Figure 17: Dynamic aperture at the center of the long straight section in the MAX IV 3 GeV storage ring (bare lattice) from tracking with TRACY-3. The plots show the ideal lattice and results for 20 seeds with field, multipole, and alignment errors. The field errors have been increased to 0.1% RMS and the alignment errors of the magnet blocks have been increased to twice their originally assumed value.

Another assumption that needs to be investigated more closely is the multipole error model. Both 3D magnet models and first magnetic bench measurements indicate that the systematic multipoles contained in the quadrupole magnets are higher than originally assumed [7, 8]. Rather than showing systematic $n = 6$ and $n = 10$ multipoles around $10^{-4}$ at 25 mm, these new measurements indicated roughly an order of magnitude larger relative amplitudes at 10 mm reference radius. Figure 18 shows a comparison between the previous multipole error model (applied to the quadrupoles only) and a modified model where larger systematic components have been assumed for all quadrupoles. Although the larger systematic multipoles show further DA reduction, the reduction is not serious and still very small compared to the overall reduction expected from field errors (e.g. Fig. 10) or misalignments (e.g. Fig. 12). If alignment and field errors can be maintained at the previously assumes levels, even with an increase of multipole content as described here, the overall resulting DA should still be sufficient.

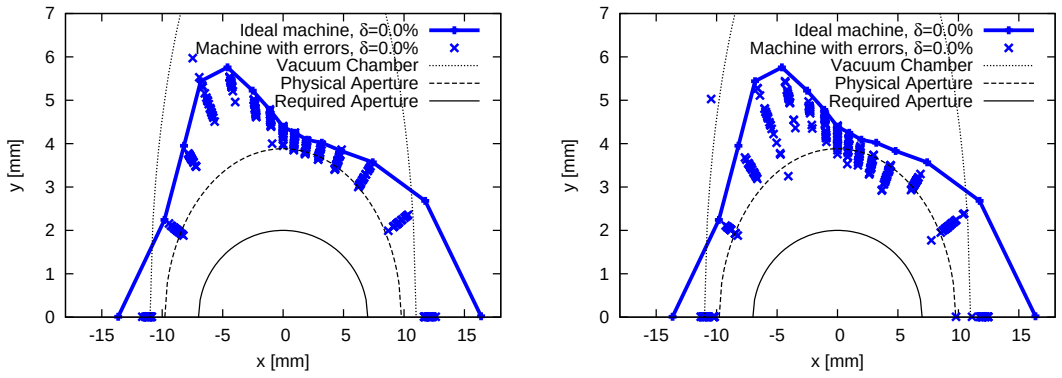


Figure 18: Dynamic aperture at the center of the long straight section in the MAX IV 3 GeV storage ring (bare lattice) from tracking with TRACY-3. The plots show the ideal lattice and results for 20 seeds with multipole errors for the quadrupole magnets only. Left: the standard multipole error model. Right: increased multipole errors according to first measurement data.

As briefly mentioned in the beginning of this chapter, the dipole is modeled in the lattice file as a sequence of dipole slices. For tracking studies including errors this means that individual dipole slices are misaligned against each other or that gradient errors are applied among dipole slices rather than among dipoles. This makes the error model not only somewhat unphysical, but most likely also optimistic. A simple way to gauge how much of a systematic error the dipole slicing introduces to the previous DA studies, is to compare with DA results using a lattice

that does not contain dipole slices. For this purpose a simplified lattice is introduced where the dipoles are modeled as simple hard-edge sector bends with a vertically focusing gradient. The bending angle matches the sum of slice bending angles, while the length has been set to match the effective length derived from the gradient distribution among all slices. Dipole gradients as well as quadrupole gradients were then tweaked to restore the design linear optics. This led to natural chromaticities not far from design. Sextupole gradients in SD and SFi were then adjusted to restore the corrected chromaticity to +1.0 in both planes, while the octupole strengths in all three families were re-adjusted to achieve the design ADTS terms. This resulted in a similar tune footprint and on/off momentum DA as in the original lattice with the slice dipole model.

All of the above detailed DA studies using various error models were repeated for the simplified lattice. In these studies the dipoles are now misaligned coherently and individually against neighboring magnets, furthermore, dipole gradient errors are now distributed statistically among various dipoles rather than among all dipole slices in the ring. The conclusion that can be drawn from a comparison of error DA studies with the original lattice vs. the simplified lattice is that, indeed, slices in the lattice lead to a somewhat optimistic picture. However, this is demonstrated by usually 1–3 seeds out of 20 that are substantially worse than the worst seeds observed using the original lattice while the average among all seeds is hardly changed. An extreme example is displayed in Fig. 19 where the underlying assumptions are the same as those used for Fig. 17, but here, the original lattice is compared to the simplified lattice without dipole slicing. The average DA among all seeds is comparable regardless of the choice of lattice, but the poorest DA is clearly recorded with the simplified lattice. For this lattice and these error assumption the worst DA is in fact so poor that it would be difficult to inject any beam into the machine at all. For most studies the differences are not as pronounced as in this comparison, but the underlying characteristics are the same. In conclusion, while estimates for average DA from many seeds can be trusted even when using a slice lattice, if one is interested in worst-case DA, the simplified lattice without the dipole slice model should be used.

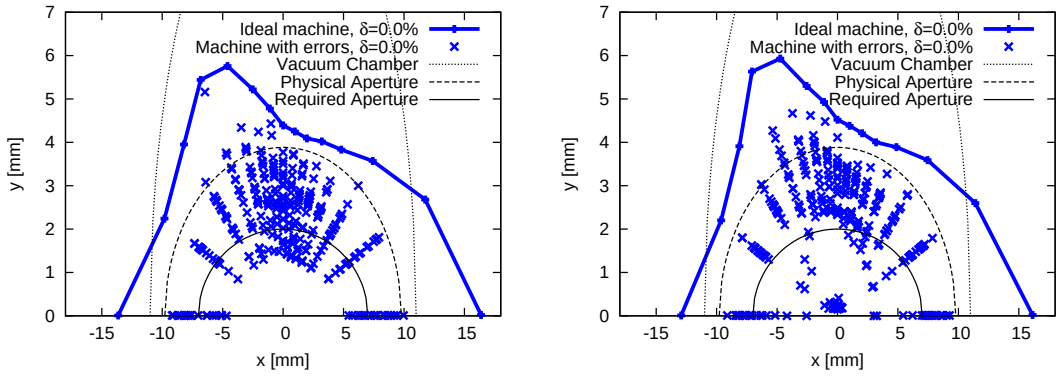


Figure 19: Dynamic aperture at the center of the long straight section in the MAX IV 3 GeV storage ring (bare lattice) from tracking with TRACY-3. The plots show the ideal lattice and results for 20 seeds with field, multipole, and alignment errors. The field errors have been increased to 0.1% RMS and the alignment errors of the magnet blocks have been increased to twice their originally assumed value. Left: the original lattice using a slice model for the dipoles. Right: a simplified lattice using a hard-edge sector magnet model for the dipoles.

## 4.3 Orbit Correction and Coupling

Closed orbit deviations result from alignment errors and orbit correction. In tracking studies, once alignment errors have been applied, an attempt is made at finding a closed orbit. The deviation between such a closed orbit and the ideal orbit[6] is the closed orbit deviation (COD). Orbit correction (OCO) then attempts to find corrector settings that minimize these deviations at the locations of the BPMs by using the inverted (ideal) response matrix; this is usually an iterative process as the actual response matrix contains the effect of the imperfections of each seed (error sequence); this is however unknown to the orbit correction routine in the tracking simulation and hence, the solution needs to be found by iterative approximation.

In the tracking studies shown here, for each case 50 error seeds were generated in Tracy-3 and closed orbit deviations as well as required corrector strengths were returned. In addition, transverse normal mode emittances are calculated which allows recording the resulting emittance coupling and tilt of the beam profile (sometimes referred to as beam ellipse twist). This section introduces results of orbit correction and coupling studies. The main sources of CODs and emittance coupling are identified and their effect quantified. The effect of orbit correction is demonstrated.

A first example shows closed orbit deviations for a single seed throughout the entire machine (cf. Fig. 20, top). In this example field errors, multipole errors, and misalignments have all been applied. The former have been modeled as described in Section 4.1.2, while the alignment errors follow the model detailed in Section 4.1.3. The results show that despite rather large CODs, beam injection and capture should be possible under the assumption that the design acceptance of the ring has not been compromised.

Once beam can be injected and stored, response matrices can be obtained and orbit correction is performed. The result of three iterative applications of orbit correction are then shown in the bottom of Fig. 20 along with the required corrector strengths. The RMS orbit (at the BPMs) has been reduced from 1.4 mm to 41 $\mu$m in the horizontal plane and from 1.1 mm to 37 $\mu$m in the vertical plane. In the process

[6]Note that this *ideal orbit* exists in simulation only. In the real machine, the *design orbit* is defined as the orbit that passes (sextupole/octupole) magnets through their centers. BPMs are calibrated to the magnetic centers of the neighboring sextupole/octupole. Hence, in the real machine, the orbit is corrected to this *design orbit*, i.e. to the magnet centers of the sextupoles/octupoles. In simulations on the other hand, the orbit is always corrected with respect to the *ideal orbit*, which—in principle—can be far away from the magnetic center. This can happen, if for example, misalignments move magnets and BPMs away from their original "ideal" position. Correcting to the *ideal orbit* is not possible in the real machine, as such an ideal orbit cannot be determined and remains unknown. A more in-depth analysis of the issue can be found in [10].

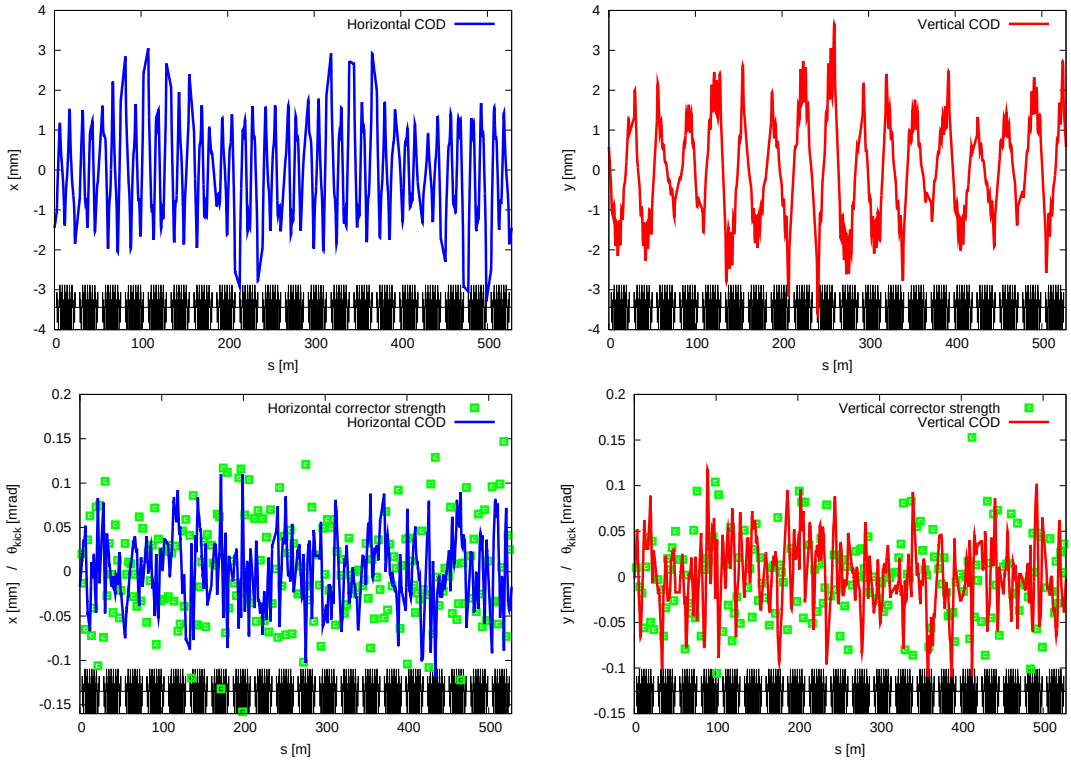


Figure 20: Top: closed orbit deviations before orbit correction for one specific error seed in the MAX IV 3 GeV storage ring. Bottom: closed orbit deviations and required corrector strengths after orbit correction for the same error seed as used in the top plots.

of this orbit correction the emittance coupling has been reduced from initially 11.8% to 0.7% well below the target while the beam ellipse twist in the long straights has been cut in half ending up at roughly 0.3° with respect to the ideal machine plane.

This example demonstrates the capability and benefit of orbit correction nicely, but it is only one example for one specific error sequence. Immediately further questions arise. Firstly, if the orbit correction system is always capable of correcting for expected imperfections as well as what the achieved performance then is, and secondly, what the exact sources for CODs and emittance coupling are as well as if possibilities exist to diminish the influence of such errors. The former require studies using many different seeds while the latter can be inferred from comparisons of multiple-seed studies using different error models. This shall be pursued in the following sections.

A first study using 50 different error seeds with the same error models as detailed

above is shown in Figs. 21—23. The RMS CODs (at the BPMs) are on the order of 1.4 mm and 1.3 mm in the horizontal and vertical planes, respectively. The average emittance coupling is 12% (9% RMS) for 50 seeds while the beam ellipse twist in the long straights is roughly 3° RMS. Under the assumption that the storage ring's design acceptance is available and that $4\sigma$ is sufficient to contain all foreseeable cases, storing beam should always be possible with imperfections according to the applied models. This is also confirmed by the distribution of RMS CODs shown in Fig. 22 (top).

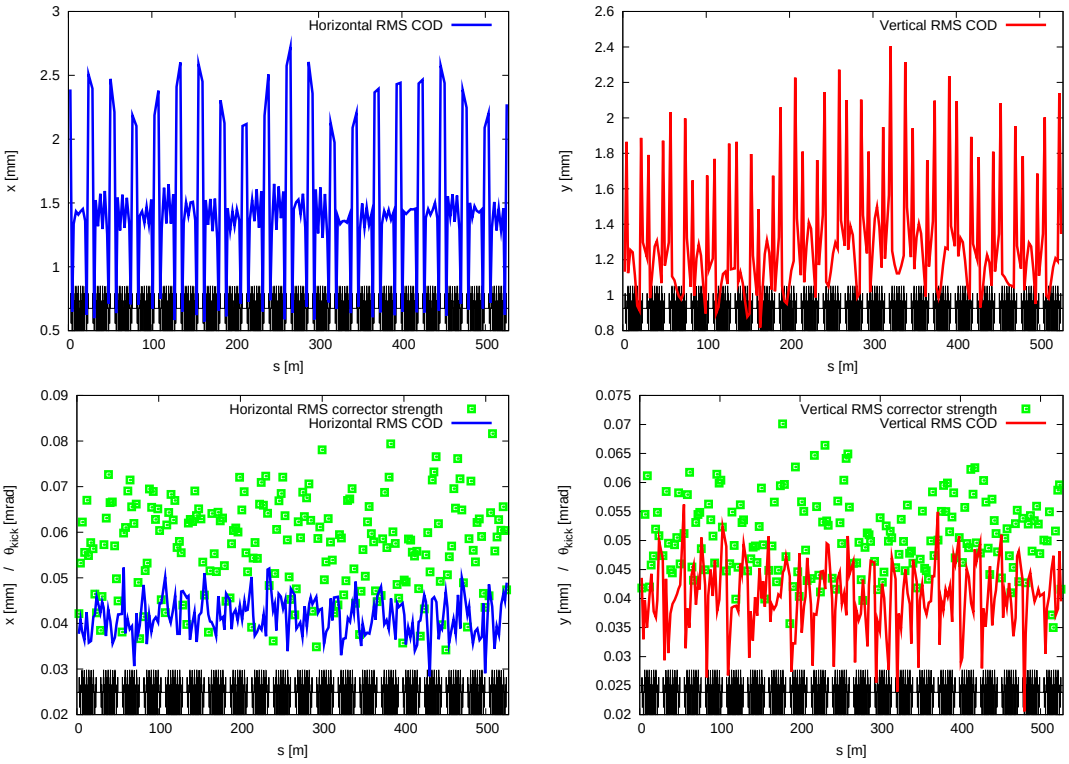


Figure 21: Top: RMS closed orbit deviations before orbit correction for 50 error seeds in the MAX IV 3 GeV storage ring. Bottom: RMS closed orbit deviations and required RMS corrector strengths after orbit correction for the same error seeds as used in the top plots.

With stored beam in the machine, response matrices can be obtained and orbit correction performed leading to residual RMS CODs (at the BPMs) on the order of 42 $\mu$m and 40 $\mu$m in the horizontal and vertical planes, respectively. Figure 22 (bottom) shows the distribution of RMS CODs after orbit correction. The orbit correction discussed here requires an RMS corrector strength (average over

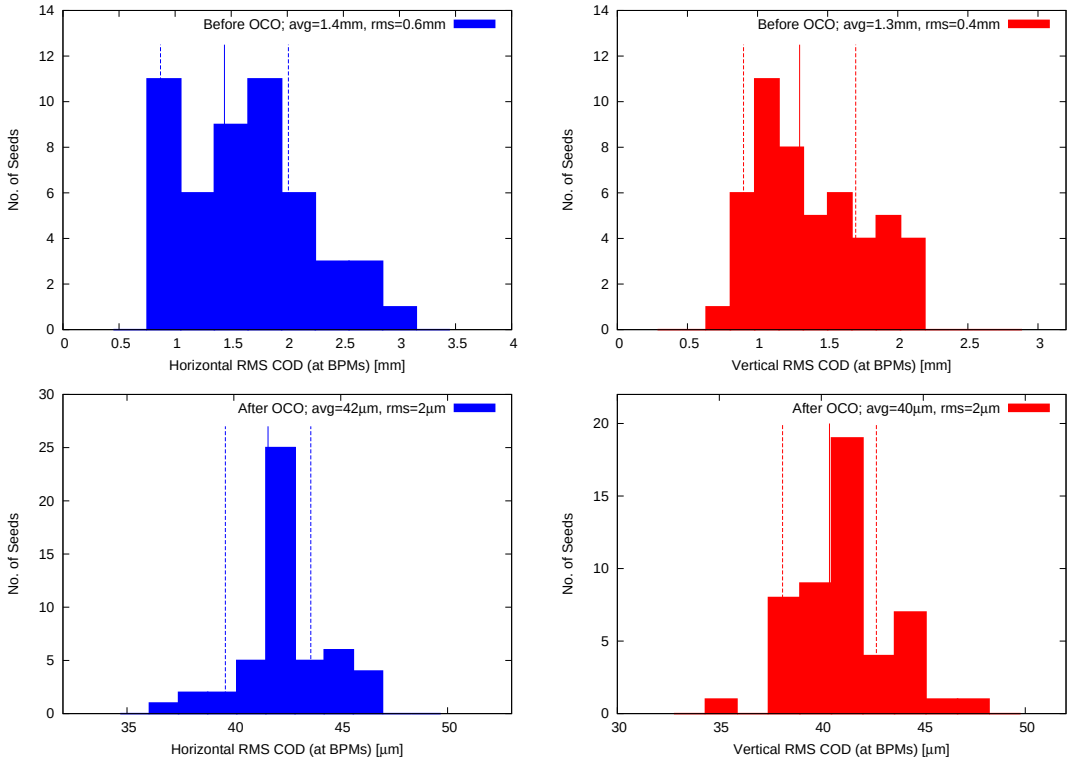


Figure 22: Histogram of RMS closed orbit deviations before (top) and after (bottom) orbit correction for 50 error seeds in the MAX IV 3 GeV storage ring. The mean values and standard deviations are indicated.

the entire machine) of 57 $\mu$rad and 51 $\mu$rad in the horizontal and vertical planes, respectively. Again, assuming $4\sigma$ is sufficient to contain all foreseeable cases, the slow orbit correctors of the MAX IV 3 GeV storage ring should be capable of performing these corrections.

Typical beam ellipse twist values in the long straights after orbit correction are below 2° with respect to the ideal machine plane. This can be inferred from the bottom right plot in Fig. 23 when looking at RMS levels in the long straights. After orbit correction the emittance coupling is reduced to 2.0% (1.4% RMS). From tracking studies the sigma ratio of the beam is obtained as displayed in Fig. 23 (left).

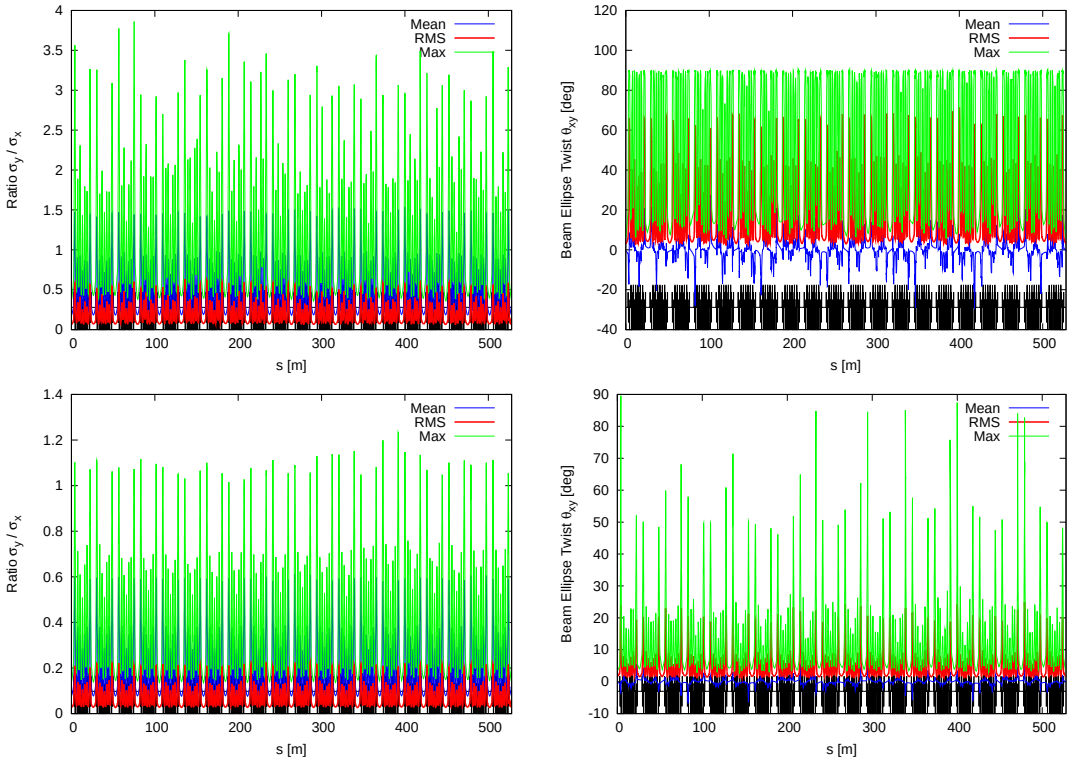


Figure 23: Left: Transverse beam size aspect ratio before (top) and after (bottom) orbit correction for 50 error seeds in the MAX IV 3 GeV storage ring. Right: Beam ellipse twist before (top) and after (bottom) orbit correction for 50 error seeds in the MAX IV 3 GeV storage ring.

For the special case where there is no horizontal dispersion, no spurious vertical dispersion, and vanishing beam ellipse twist, the emittance coupling $\kappa = \varepsilon_{II}/\varepsilon_I$ and sigma ratio $\sigma_y/\sigma_x$ are closely connected since for such a case $\sigma_y/\sigma_x \approx \sqrt{\kappa\,\beta_y/\beta_x}$. Once the orbit has been corrected, the horizontal dispersion along with the spurious vertical dispersion in the long straights becomes very small. As indicated the bottom right plot in Fig. 23, the beam ellipse twist in the long straights is also very small once orbit correction has been successfully applied. Hence, it is to be expected that the long straights show a sigma ratio consistent with what can be approximated from the emittance coupling ratio. Indeed, tracking studies reveal a sigma ratio of roughly 0.077 (average for 50 seeds), while $\kappa = \varepsilon_{II}/\varepsilon_I = 2\%$ would correspond to $\sigma_y/\sigma_x = 0.067$ at the center of the long straight. Table 7 contains a summary of results for the standard error model including all types of imperfections.

Table 7: Tracking results using 50 error seeds for the MAX IV 3 GeV storage ring lattice with all types of imperfections. The COD results are taken across seeds; CODs within an individual seed are evaluated at the BPMs only. The corrector strengths results are taken across all correctors; individual corrector results are RMS values across all seeds.

| | Standard imperfections | |
|---|---|---|
| | before OCO | after OCO |
| RMS beam ellipse twist | 56 mrad | 31 mrad |
| Mean emittance coupling | 12.4% | 2.0% |
| RMS emittance coupling | 9.2% | 1.4% |
| Mean hor. COD | 1.4 mm | 42 $\mu$m |
| RMS hor. COD | 0.6 mm | 2 $\mu$m |
| Mean ver. COD | 1.3 mm | 40 $\mu$m |
| RMS ver. COD | 0.4 mm | 2 $\mu$m |
| Mean hor. corr. strength | n/a | 57 $\mu$rad |
| RMS hor. corr. strength | n/a | 10 $\mu$rad |
| Mean ver. corr. strength | n/a | 51 $\mu$rad |
| RMS ver. corr. strength | n/a | 6 $\mu$rad |

The above expected values for emittance coupling, beam ellipse twist, and CODs as a result of orbit correction can certainly be deemed acceptable. However, in order to further improve on this situation, it is important to understand which type of imperfection is the dominating source. For this purpose several studies were conducted with different error types included in the imperfection model. After thorough comparison it becomes quite evident that the main driver for CODs, emittance coupling, and beam ellipse twist are alignment errors. This can be easily seen when comparing Fig. 24 where only alignment errors have been taken into account with the previous Fig. 21 which includes besides misalignments also field and multipole errors.

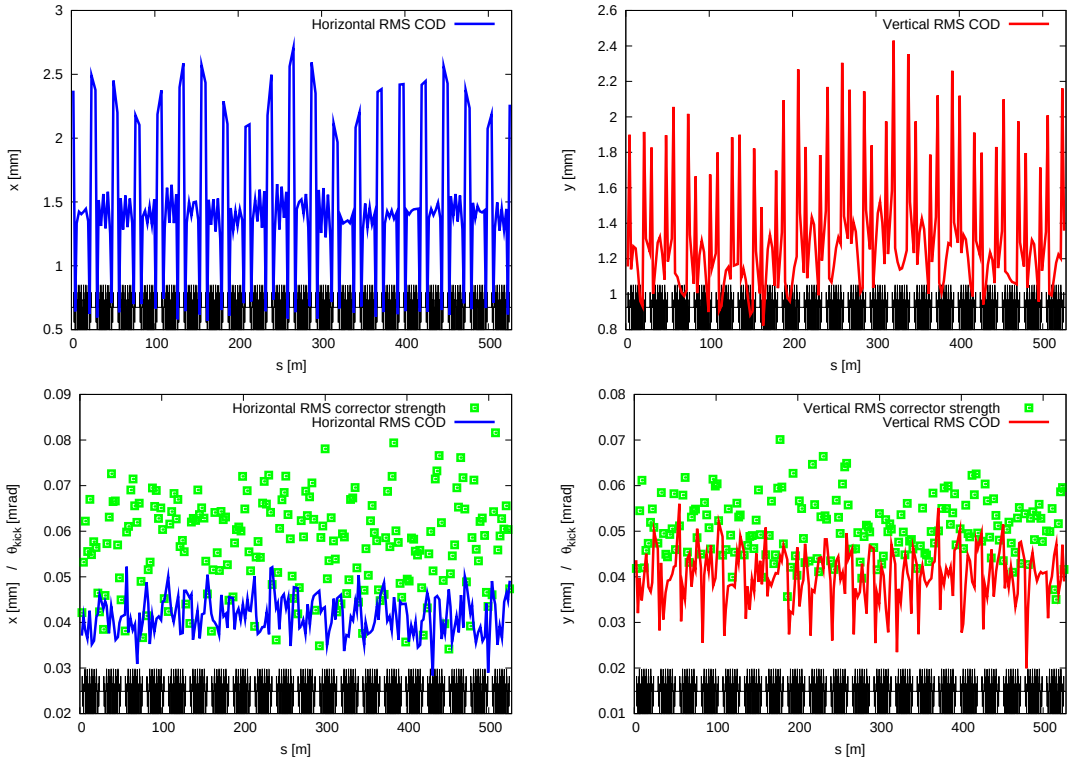


Figure 24: Top: RMS closed orbit deviations before orbit correction for 50 error seeds using alignment errors only. Bottom: RMS closed orbit deviations and required RMS corrector strengths after orbit correction for the same error seeds as used in the top plots.

As can be expected, the CODs and corrector strengths are basically unchanged. There is no change in mean values of beam ellipse twist or emittance greater than 3% of the RMS value. This can also be seen in the histogram shown in Fig. 25 where the two different error models are compared both before and after orbit correction.

Once alignment errors have been determined to be the main driver behind CODs and coupling, the next question is what type of misalignment has the most effect. One obvious candidate would be magnet roll errors. More specifically, quadrupole and sextupole roll errors[7]. As briefly mentioned towards the end of Section 4.1.3, there is a possibility of increased roll errors among quadrupoles and sextupoles related to the assembly of the yoke pieces in the solid iron blocks for each cell.

[7]Dipole roll errors would obviously also create vertical dispersion. It is believed, however, that because each magnet blocks contains a single large dipole and because this dipole's field is mapped very carefully, survey and alignment will succeed in installing the block in such a ways as to reduce dipole roll errors to very low levels compared to those of other magnetic elements within the same block.

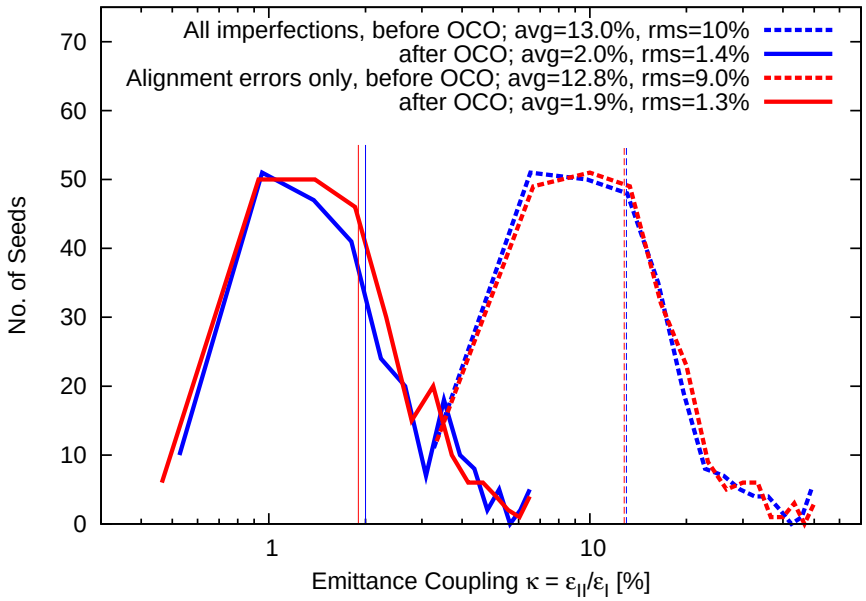


Figure 25: Histogram of emittance coupling results for two different cases: error model including all imperfections vs. error model including misalignments only. Both coupling values before and after orbit correction are shown. Average values among all 250 seeds per case are indicated by thin lines.

To model the effect of such an increased level of roll, a study on orbit correction and coupling was performed assuming that individual quadrupole and sextupole errors would come in at 0.5 mrad roll RMS instead of the originally assumed 0.2 mrad RMS (in addition to the 0.2 mrad RMS roll of the entire magnet block). Table 8 shows a summary of the changes. It is important to point out that while the emittance coupling mean values change as a consequence of the increased roll errors, the increase remains very small compared to the RMS value. It is therefore believed that despite a potential increase of quadrupole and sextupole roll errors, there will be no significant effect on coupling.

Table 8: Tracking results using 50 error seeds for the MAX IV 3 GeV storage ring lattice with alignment errors. The COD results are taken across seeds; CODs within an individual seed are evaluated at the BPMs only. The corrector strengths results are taken across all correctors; individual corrector results are RMS values across all seeds.

| | Standard misalignments | | Increased roll errors | |
|---|---|---|---|---|
| | before OCO | after OCO | before OCO | after OCO |
| RMS twist | 57 mrad | 31 mrad | 60 mrad | 38 mrad |
| Mean emittance coupling | 12.6% | 2.1% | 12.8% | 2.7% |
| RMS emittance coupling | 8.5% | 1.5% | 8.4% | 2.1% |
| Mean hor. COD | 1.4 mm | 42 $\mu$m | 1.4 mm | 42 $\mu$m |
| RMS hor. COD | 0.6 mm | 2 $\mu$m | 0.6 mm | 2 $\mu$m |
| Mean ver. COD | 1.3 mm | 40 $\mu$m | 1.3 mm | 40 $\mu$m |
| RMS ver. COD | 0.4 mm | 2 $\mu$m | 0.4 mm | 3 $\mu$m |
| Mean hor. corr. strength | n/a | 57 $\mu$rad | n/a | 57 $\mu$rad |
| RMS hor. corr. strength | n/a | 10 $\mu$rad | n/a | 10 $\mu$rad |
| Mean ver. corr. strength | n/a | 51 $\mu$rad | n/a | 51 $\mu$rad |
| RMS ver. corr. strength | n/a | 6 $\mu$rad | n/a | 6 $\mu$rad |

Since an increase of the roll errors do not appear to affect CODs and coupling, the next candidate is the actual displacement of magnets form the ideal orbit. Specifically girder misalignment (cf. p. 41) and individual magnet misalignment leading to large vertical CODs in the sextupoles (cf. p. 55). Before investigating these issues, however, it should first be verified that the results presented here are not masked by artifacts of two already mentioned deficiencies in the model, namely

1. Dipoles are modeled as series of slices where any individual slice can be misaligned and have its own field and multipole errors compared to the next slice. This is unphysical and leads—due to the way in which imperfections are specified— to presumably somewhat optimistic performance estimates (cf. p. 14, 15).
2. The orbit position and stability in the IDs is measured in terms of the COD at the BPMs flanking the ID (in the real machine). In tracking studies, however, orbit correction is performed towards the ideal orbit (cf. p. 31). Since the BPMs are a part of the girder assembly and since the girders can be misaligned considerably with respect to the ideal orbit in tracking simulations, this can

lead to a situation where large CODs in a long straight can be mistaken for large orbit fluctuations in the ID, when actually they are merely artifacts of BPM misalignments with respect to the ideal orbit (which exists in simulation only).

Similar to the cross-check performed above, issue no. 1 was investigated by comparing results with those obtained using a simplified lattice where all slice dipole models had been replaced by an individual hard-edge sector bend with the same bending angle and integrated vertically focusing gradient as the slice model. Studies including all types of misalignments as well as those containing only alignment errors were conducted using the simplified lattice. Although the slice model does indeed lead to slightly optimistic results before OCO is applied, no significant changes in CODs, coupling, or beam ellipse twist could be determined once OCO had completed.

Issue no. 2 can be can be dealt with by moving the BPMs in the matching cells off the girders. Although this results in a model which is systematically misrepresenting the situation in the real machine (where BPMs are calibrated with respect to the adjacent sextupole/octupole magnet to which they are firmly attached), it has the distinct advantage that orbit correction in the tracking simulation now corrects the orbit towards the BPM centers (as it would in the real machine) while it attempts to correct the orbit within the ID to the ideal orbit (which doesn't exist in the real machine). The remaining deviation between ideal orbit and the OCO's target orbit is then dominated by the 3 $\mu$m RMS offset between BPMs and ideal orbit representing the reproducibility/accuracy of the BPM calibration (cf. Section 4.1.3). In studies using such a lattice model, the beam ellipse twist and emittance coupling after correction remain unchanged, however, the CODs are reduced in the long straights as expected. The overall change for the entire machine is small as it is dominated by the many BPM readings within the unit cells where BPMs cannot be modeled off the girder. Figure 26 shows CODs after orbit correction and and required corrector strengths for a study where all imperfections have been applied to a lattice with long straight section BPMs modeled off the girder. They can be compared to the original situation shown in Fig. 21 revealing that the RMS CODs in the long straights are now on sub-10 $\mu$m level without requiring any extra corrector strength.

A more in-depth analysis of the two issues regarding modeling raised above can be found in [10].

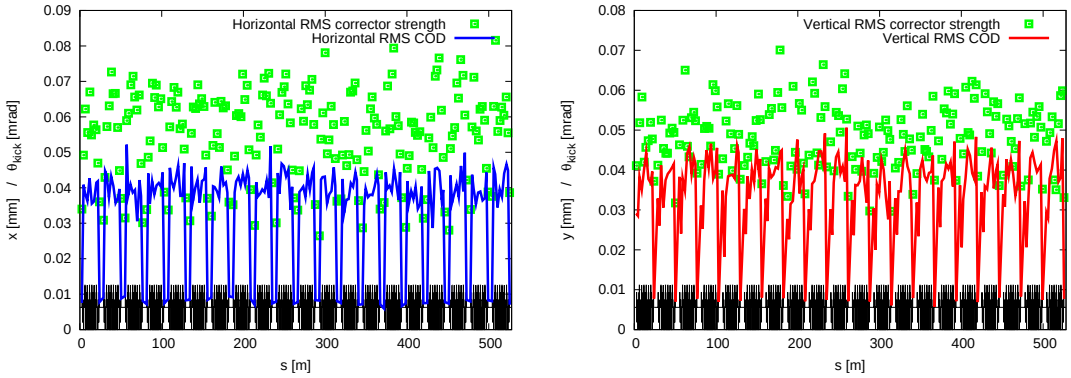


Figure 26: RMS closed orbit deviations and required RMS corrector strengths after orbit correction for 50 error seeds using a modified lattice model for the MAX IV 3 GeV storage ring. In this model the BPMs in the long straight sections (and hence the BPM readings displayed here) are not misaligned with respect to the ideal orbit by more than the BPM calibration reproducibility/accuracy.

### 4.3.1 Increased Imperfections During Early Commissioning

Returning to the main sources of CODs and coupling, girder misalignments (i.e. correlated misalignments across many magnets) are suspected to have a significant impact. As already mentioned on p. 26, when commissioning begins more significant girder misalignments (along with increased levels of field errors) have to be expected. This has significant consequences for CODs and coupling, the most severe however, before orbit correction can be performed. Using the same set of imperfections as already described on p. 26 orbit correction and coupling studies were repeated. An example for one seed with the elevated levels of imperfections is given in Fig. 27. The COD before orbit correction are 1.7 mm in both planes and maximum deviations throughout the ring approach half of the available *design* acceptance[8]. Orbit correction succeeds in reducing the CODs to 83 $\mu$m and 74 $\mu$m in the horizontal and vertical planes, respectively. This can be compared to the case shown in Fig. 20 where the standard level of imperfections was applied, namely transverse girder misalignments on the order of 50 $\mu$m RMS compared to the 100 $\mu$m used here. The case shown here requires roughly twice the corrector strength of the originally displayed case.

[8]Note that the design acceptance will not necessarily be available at the beginning of commissioning before any beam-based measurements have revealed and allowed correction of crude imperfections.

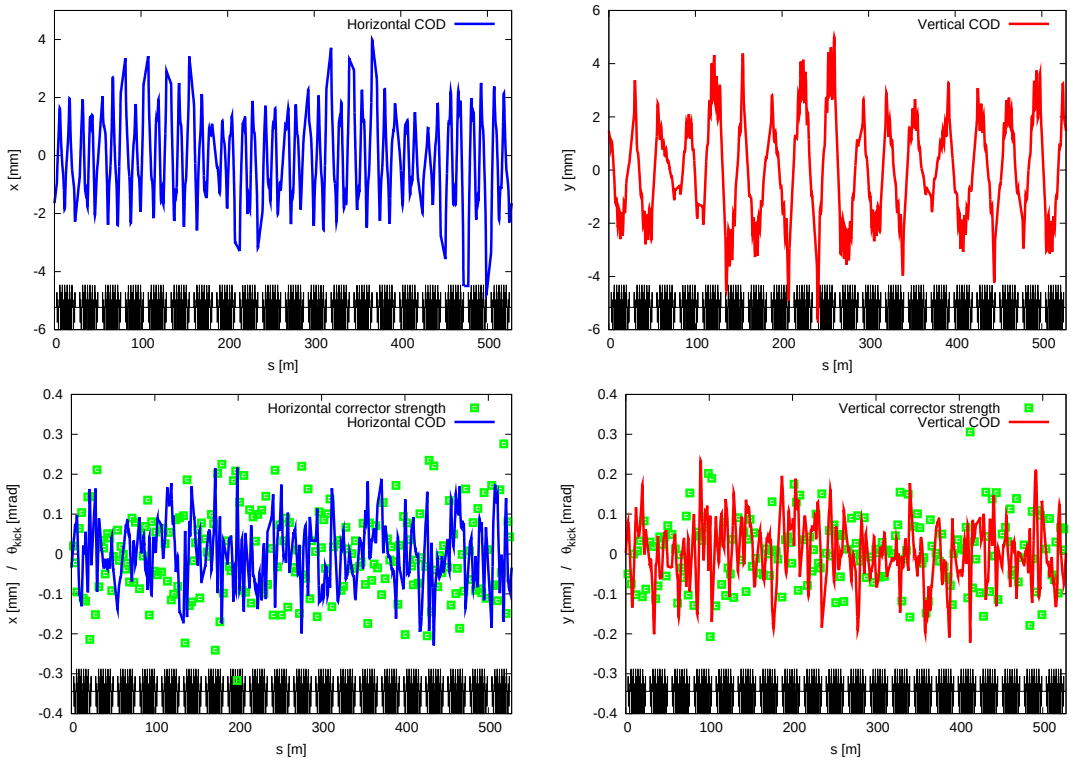


Figure 27: Top: closed orbit deviations before orbit correction for one specific error seed in the MAX IV 3 GeV storage ring. The error model applied here assumes larger misalignments and field errors as they are expected to during early stages of commissioning. Bottom: closed orbit deviations and required corrector strengths after orbit correction for the same error seed as used in the top plots.

The study was expanded to include many seeds in order to get some statistics. In roughly half of the 50 seeds the imperfections were, however, so severe that the threader was not able to find a closed orbit unless the imperfections were ramped up to their full levels in steps. If the OCO routine is allowed to ramp up errors successively so the threader always succeeds in finding a closed orbit, all 50 error seeds can be analyzed in terms of CODs, corrector strengths, and coupling. Results are displayed in Figs. 28–30. A comparison can be made with the results for the standard imperfection models shown in Figs. 21–23.

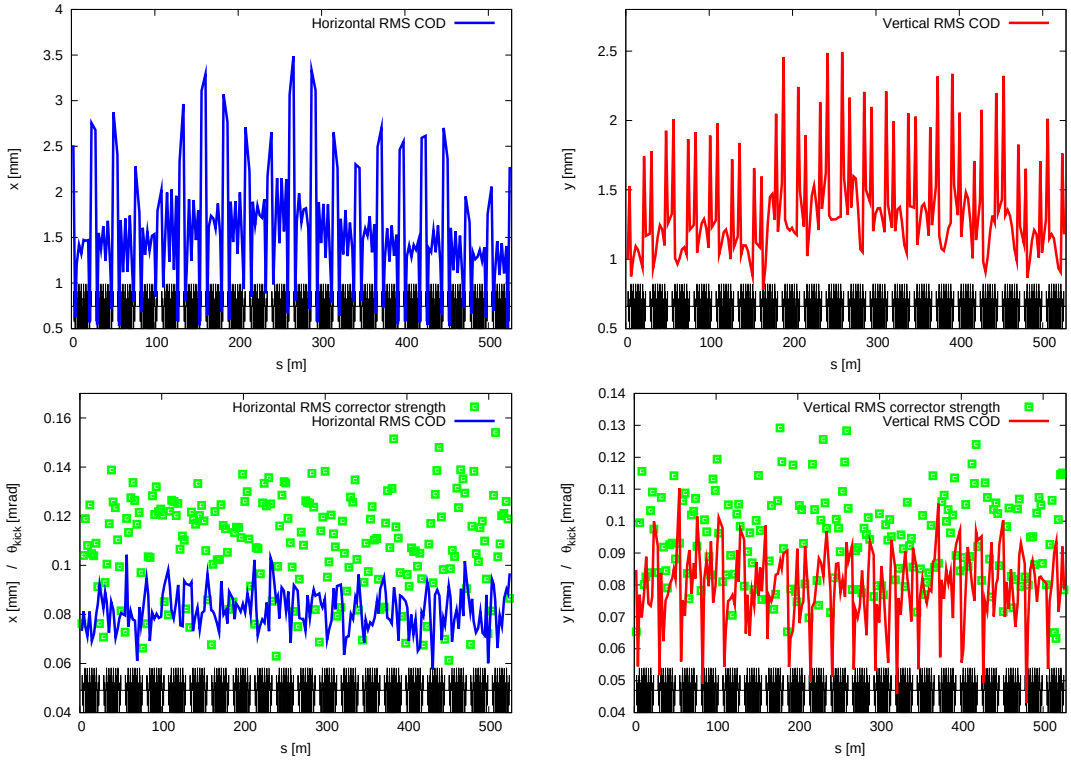


Figure 28: Top: RMS closed orbit deviations before orbit correction for 50 error seeds in the MAX IV 3 GeV storage ring. The error model applied here assumes larger misalignments and field errors as they are expected to during early stages of commissioning. Bottom: RMS closed orbit deviations and required RMS corrector strengths after orbit correction for the same error seeds as used in the top plots.

Orbit correction succeeds in reducing the mean RMS COD to 82 $\mu$m and 80 $\mu$m in the horizontal and vertical planes, respectively. This requires an average RMS corrector strength of 108 $\mu$rad and 94 $\mu$rad in the horizontal and vertical planes, respectively. These are roughly twice the values generated when using the standard imperfection models. After orbit correction an RMS beam ellipse twist of 51 mrad remains while the emittance coupling average lies at roughly 6%.

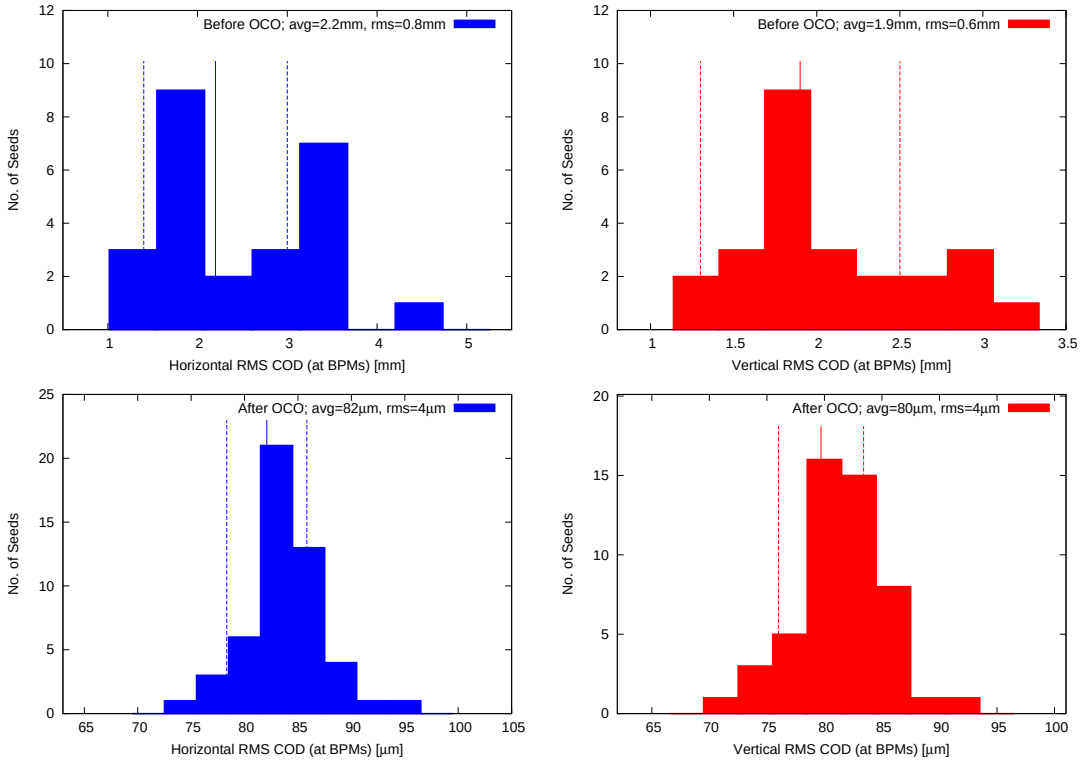


Figure 29: Histogram of RMS closed orbit deviations before (top) and after (bottom) orbit correction for 25 (top) / 50 (bottom) error seeds in the MAX IV 3 GeV storage ring. The error model applied here assumes larger misalignments and field errors as they are expected to during early stages of commissioning. The mean values and standard deviations are indicated.

It is important to note here that this case lies close to the limit of what can still be tolerated in order to inject and capture beam in the storage ring during early stages of commissioning. Although the orbit correctors should offer adequate strength in most cases, the resulting orbits end up occupying large amounts of the overall available design acceptance in many seeds. The fact that these increased levels of imperfections push the lattice to the limit of what can be handled during early commissioning is quite consistent with the conclusions already drawn during DA analysis (cf. p. 26).

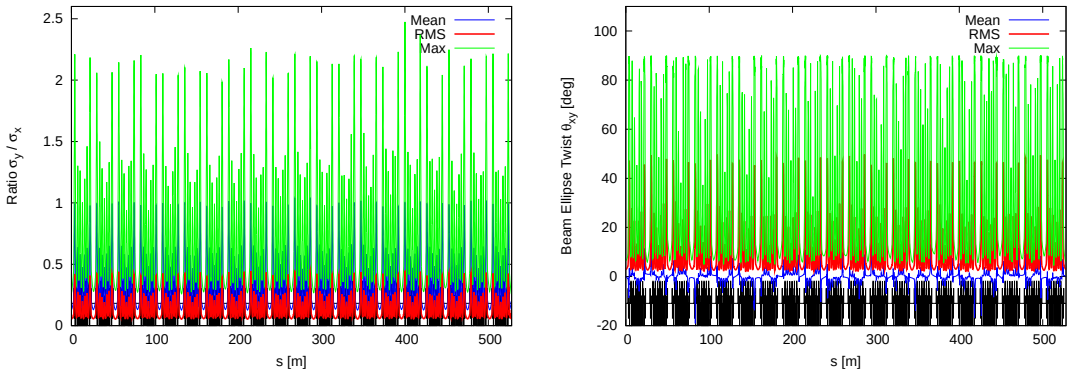


Figure 30: Left: Transverse beam size aspect ratio after orbit correction for 50 error seeds in the MAX IV 3 GeV storage ring. The error model applied here assumes larger misalignments and field errors as they are expected to during early stages of commissioning. Right: Beam ellipse twist after orbit correction for 50 error seeds in the MAX IV 3 GeV storage ring.

As concluded from the discussion of the commissioning scenario DA results, it appears crucial to prevent large initial girder misalignments which in turn could jeopardize early commissioning efforts to inject and store beam. Since beam-based measurements revealing local alignment issues only become possible once beam can be injected and stored, it is paramount to ensure survey and alignment procedures succeed in aligning neighboring girders to within better than 50 $\mu$m RMS or within the absolute limits of $\pm 100\,\mu$m so that any beam-based improvement of the initial machine becomes possible.

An impressive display of the influence of girder misalignments on overall coupling levels is given in Fig. 31. If it is assumed that the increased girder misalignments are left uncorrected, emittance coupling—despite orbit correction efforts—will not be able to systematically undercut the coupling levels achieved with standard imperfection models and no orbit correction at all. Or conversely, if girder alignment errors are allowed to increase to the levels discussed in this Section, no amount of orbit correction effort can make up entirely for the amount of coupling generated by the girder misalignments. Naturally, local corrections of spurious vertical dispersion and betatron coupling could also be contemplated in order to cope with the consequences of large girder misalignments, however, such a correction scheme would require a very large number of individual power supplies (on the order of 40–80 across the entire ring) exciting skew quadrupole components in the sextupoles and octupoles (which have been equipped with the necessary auxiliary windings). This, however, presents a cost and complexity issue of its own.

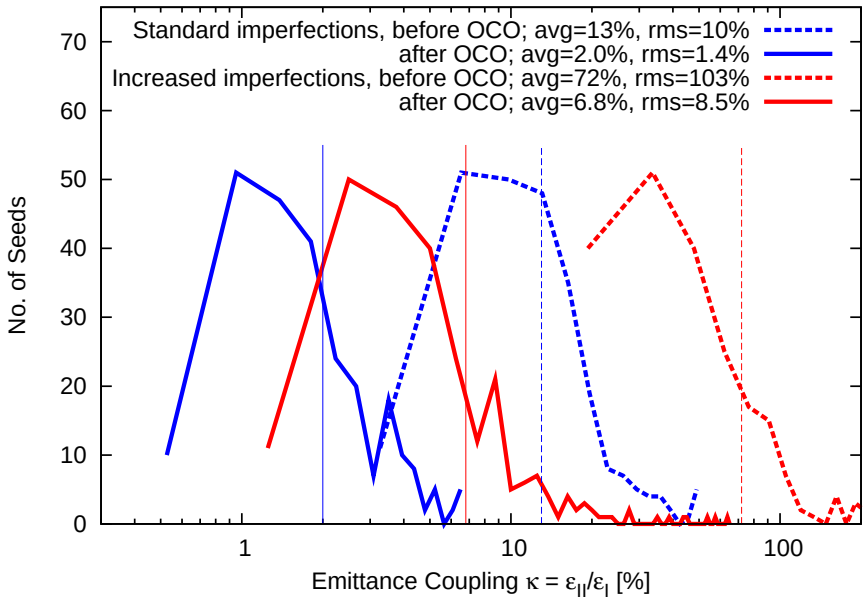


Figure 31: Histogram of emittance coupling results for two different cases: error model including standard imperfections vs. error model including increased imperfections as expected during early commissioning. Both coupling values before and after orbit correction are shown. Average values among all 250 seeds per case are indicated by thin lines.

### 4.3.2 Reduced Girder Misalignments After Re-alignment

Assuming that beam can be injected and stored in the machine, the previous line of thought can be reversed: one can ask what levels of performance can be achieved if beam-based measurements are employed in order to detect and reduce girder displacements through successive girder re-alignment. Since CODs and coupling appear to be heavily dominated by girder misalignments, using beam-based measurements to reduce these misalignments presents a natural method to improve storage ring performance. Similar to what was done during analysis of the DA under influence of imperfections (cf. p. 24), CODs and coupling can be investigated assuming that girder misalignments have been reduced to roughly half of the values in the standard misalignment model (i.e. 25 $\mu$m RMS transverse misalignment, 0.1 mrad RMS roll error).

This is shown in Figs. 32–34 and can be directly compared to Figs. 21–23. The CODs and corrector strengths are roughly cut in half compared to the standard error model. The reduction of beam ellipse twist is not quite as large, but it it is still

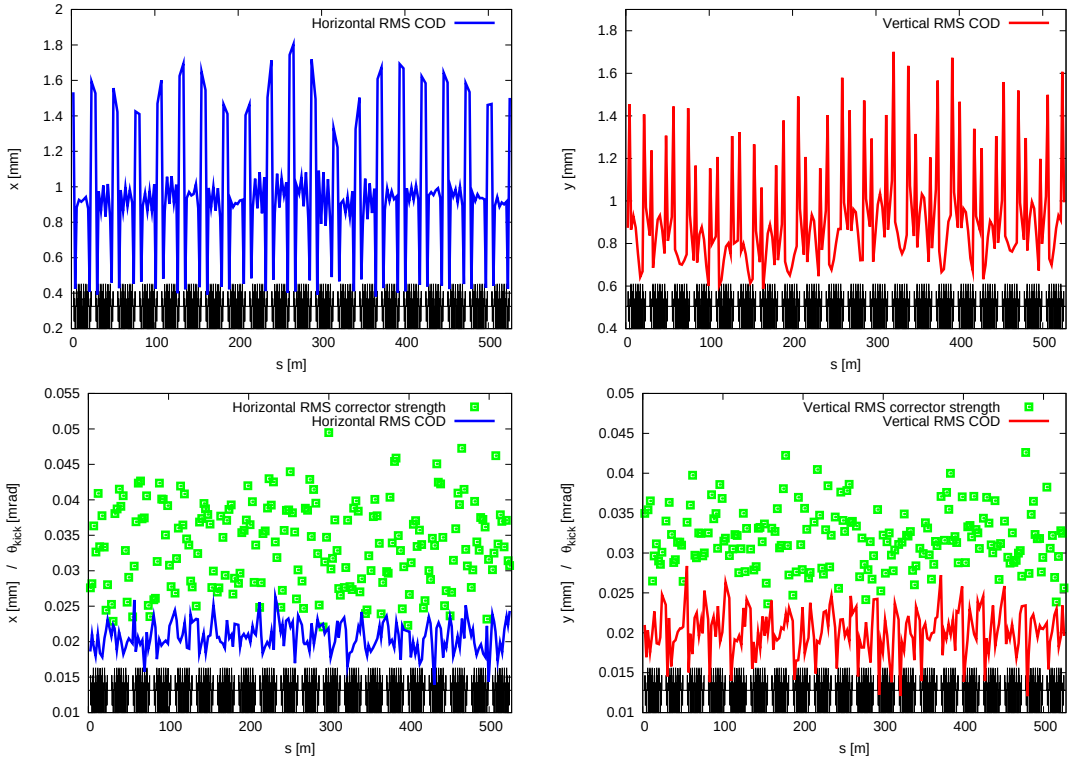


Figure 32: Top: RMS closed orbit deviations before orbit correction for 50 error seeds in the MAX IV 3 GeV storage ring. The error model applied here assumes reduced girder misalignments as could possibly be expected after beam-based measurements and re-alignment. Bottom: RMS closed orbit deviations and required RMS corrector strengths after orbit correction for the same error seeds as used in the top plots.

significant, especially once the orbit has been corrected, when a remaining tilt in the long straights on the order of just 1° can be expected. The mean emittance coupling can be pushed to roughly 1% using orbit correction alone in the situation where the girder misalignments have been reduced to within $\pm 50\,\mu$m. Table 9 contains a summary of results comparing the standard error models to an error model with reduced girder misalignments.

It is noteworthy that these reduced girder misalignments allow reaching a vertical emittance on the order of 3 pm rad *without any* skew quadrupole corrections to directly address local betatron coupling and/or spurious vertical dispersion. Future studies will investigate such efforts to estimate what the lowest achievable vertical emittance becomes as a function of skew quadrupole correction effort.

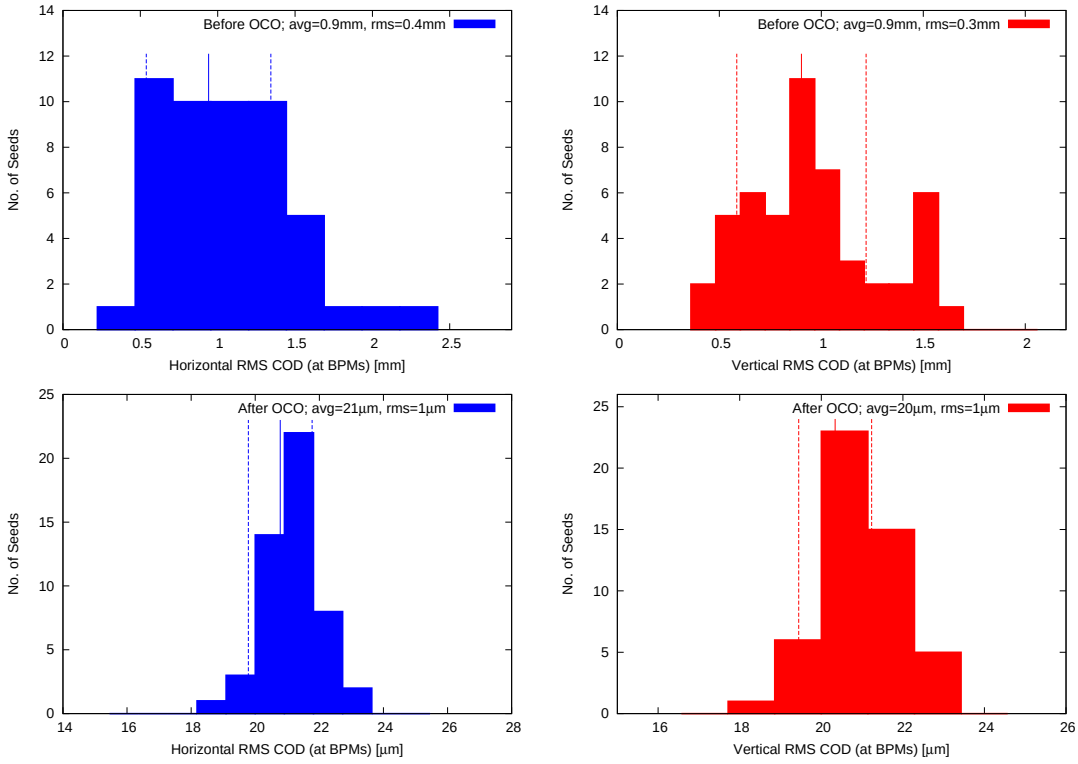


Figure 33: Histogram of RMS closed orbit deviations before (top) and after (bottom) orbit correction for 50 error seeds in the MAX IV 3 GeV storage ring. The error model applied here assumes reduced girder misalignments as could possibly be expected after beam-based measurements and re-alignment. The mean values and standard deviations are indicated.

From these studies it appears as if emittance coupling (after orbit correction) scales roughly with the girder misalignments. It is also rather interesting to note that if girder misalignments are allowed to increase too much, orbit correction can no longer ensure sufficiently low emittance coupling. On the other hand, girder re-alignment appears to be a very efficient method to reduce emittance coupling. This is illustrated nicely by the comparison shown in Fig. 35 where it is demonstrated that girder re-alignment in many cases leads to lower coupling *even before* orbit correction than can be achieved using the standard girder misalignments in combination with orbit correction. At this point it must once again be emphasized that tight initial alignment of the girders is crucial in order to quickly get stored beam of decent quality during early commissioning. Once this has been achieved, a beam-based misalignment measurement and re-alignment campaign promises significant

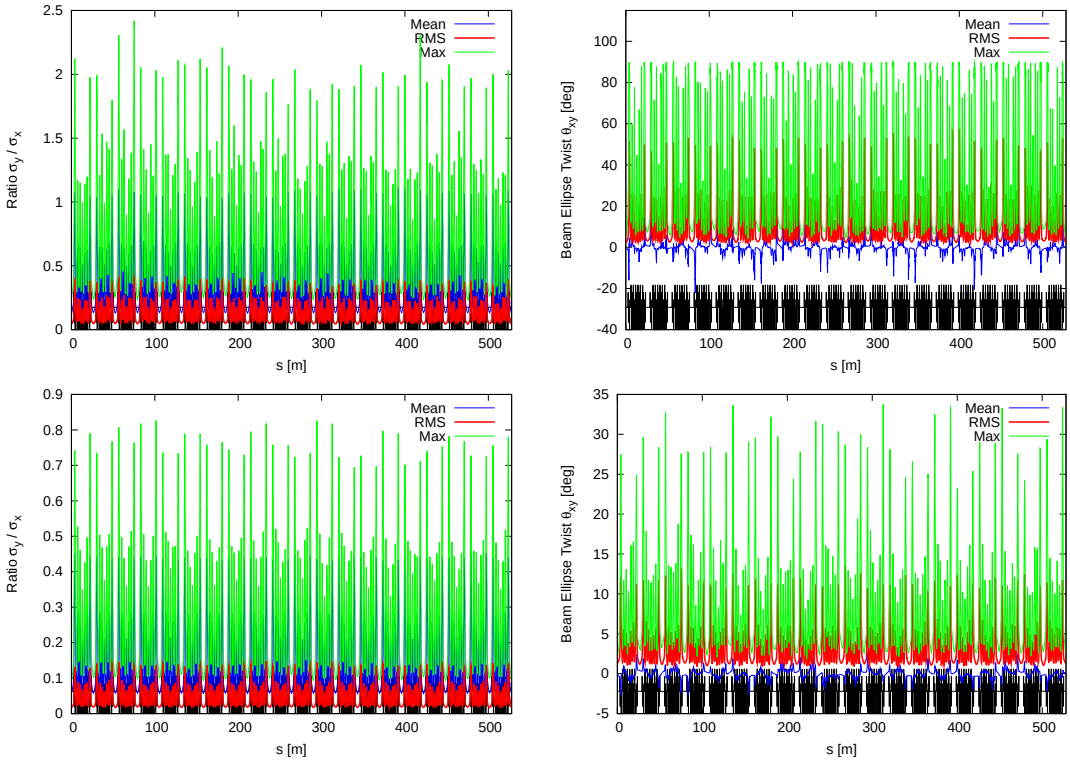


Figure 34: Left: Transverse beam size aspect ratio before (top) and after (bottom) orbit correction for 50 error seeds in the MAX IV 3 GeV storage ring. Right: Beam ellipse twist before (top) and after (bottom) orbit correction for 50 error seeds in the MAX IV 3 GeV storage ring. The error model applied here assumes reduced girder misalignments as could possibly be expected after beam-based measurements and re-alignment.

performance benefits.

Table 9: Tracking results using 50 error seeds for the MAX IV 3 GeV storage ring lattice with alignment errors. The COD results are taken across seeds; CODs within an individual seed are evaluated at the BPMs only. The corrector strengths results are taken across all correctors; individual corrector results are RMS values across all seeds.

| | Standard imperfections | | Reduced girder misalignments | |
|---|---|---|---|---|
| | before OCO | after OCO | before OCO | after OCO |
| RMS twist | 56 mrad | 31 mrad | 43 mrad | 23 mrad |
| Mean emittance coupling | 12.4% | 2.0% | 6.2% | 1.1% |
| RMS emittance coupling | 9.2% | 1.4% | 4.1% | 0.6% |
| Mean hor. COD | 1.4 mm | 42 $\mu$m | 0.9 mm | 20.8 $\mu$m |
| RMS hor. COD | 0.6 mm | 2 $\mu$m | 0.4 mm | 1.0 $\mu$m |
| Mean ver. COD | 1.3 mm | 40 $\mu$m | 0.9 mm | 20.3 $\mu$m |
| RMS ver. COD | 0.4 mm | 2 $\mu$m | 0.3 mm | 0.9 $\mu$m |
| Mean hor. corr. strength | n/a | 57 $\mu$rad | n/a | 34 $\mu$rad |
| RMS hor. corr. strength | n/a | 10 $\mu$rad | n/a | 6 $\mu$rad |
| Mean ver. corr. strength | n/a | 51 $\mu$rad | n/a | 32 $\mu$rad |
| RMS ver. corr. strength | n/a | 6 $\mu$rad | n/a | 4 $\mu$rad |

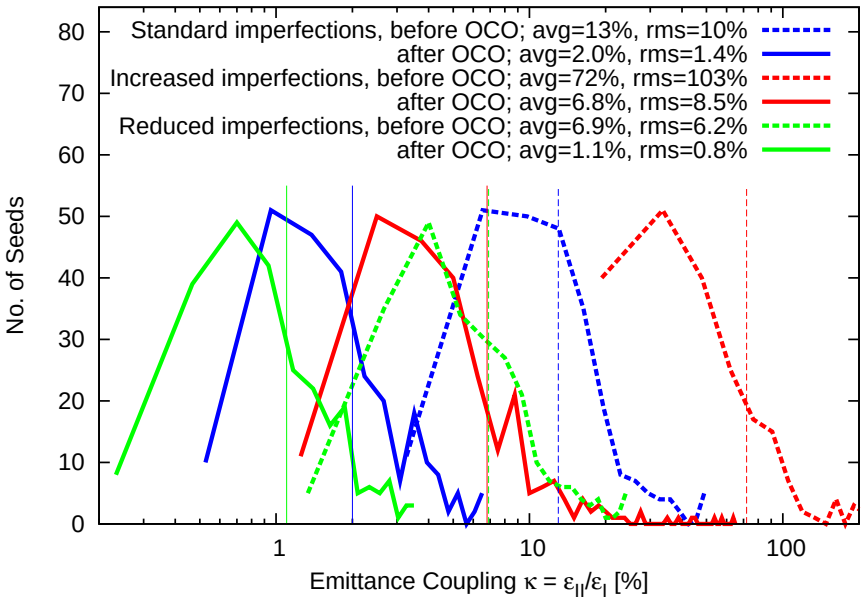


Figure 35: Histogram of emittance coupling results for three different cases: error model including standard imperfections vs. error model including increased imperfections as expected during early commissioning vs. error model including reduced imperfections as possibly expected after beam-based re-alignment. Both coupling values before and after orbit correction are shown. Average values among all 250 seeds per case are indicated by thin lines.

### 4.3.3 Sources of Coupling

As mentioned in the previous Sections, girder misalignments appear to drive coupling. However, the question remains what the actual source of this coupling increase is. Several studies were conducted in order to pinpoint the exact cause of coupling increase. Extra roll errors on quadrupoles and sextupoles did not lead to a large increase of emittance coupling (cf. p. 37). But in principle quadrupole roll errors do drive coupling since they generate skew quadrupole components. To gauge the sensitivity of the lattice to quadrupole roll errors a study was conducted comparing emittance coupling for the standard misalignment model to that calculated for an identical model but with zero quadrupole roll errors as well as with increased quadrupole roll errors. The standard misalignment model assumes individual quadrupoles have a RMS roll error of 0.2 mrad (in addition to the roll error of the girder). The increased quadrupole roll error assumed in this study was set

at 0.5 mrad RMS for individual magnets (again in addition to the roll error of the girder)[9]. A summary of the results is displayed in Fig. 36. Note that while the emittance coupling for all three cases is roughly the same before orbit correction, it differs by almost one standard deviation after orbit correction. While neglecting quadrupole roll errors has a very small influence, increasing the roll errors leads to roughly an additional 1% emittance coupling after orbit correction.

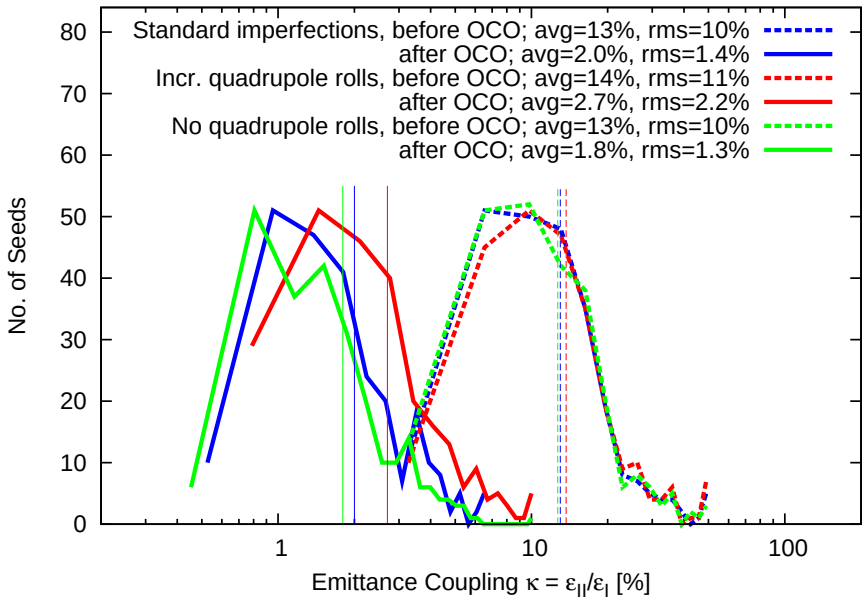


Figure 36: Histogram of emittance coupling results for three different cases: error model including standard imperfections (i.e. with 0.2 mrad RMS quadrupole rolls) vs. error model including increased quadrupole rolls (0.5 mrad RMS) vs. error model without any individual quadrupole rolls. Both coupling values before and after orbit correction are shown. Average values among all 250 seeds per case are indicated by thin lines.

Nevertheless, as long as individual quadrupole roll errors are not allowed to increase too far, it appears coupling results are dominated by other error sources. Additional studies were conducted to investigate the effect of transverse misalignments of individual quadrupoles. Such errors feed down as dipole kick errors which can be directly compensated for by the orbit correction system and hence, does not lead to large emittance coupling after orbit correction. In fact, varying transverse

[9]Note that in this specific case the threader could not find a closed orbit for one seed without ramping up errors.

quadrupole misalignments around the expected value shows no effect on emittance coupling after orbit correction at all.

The primary driver of emittance coupling lies obviously in sextupole errors. This comes as no surprise considering that any vertical sextupole misalignment feeds down as a skew quadrupole. In order to verify this mechanism and gauge then lattice's sensitivity to sextupole imperfections, studies were conducted where different types of sextupole errors were removed from the standard imperfections model and emittance coupling results then compared. Figure 37 shows a summary of such a study. Once orbit correction has completed, the cases fall into two groups: increased emittance coupling for the cases with the standard transverse sextupole misalignments and lower emittance coupling for those cases where the (individual) transverse sextupole misalignments have been set to zero.

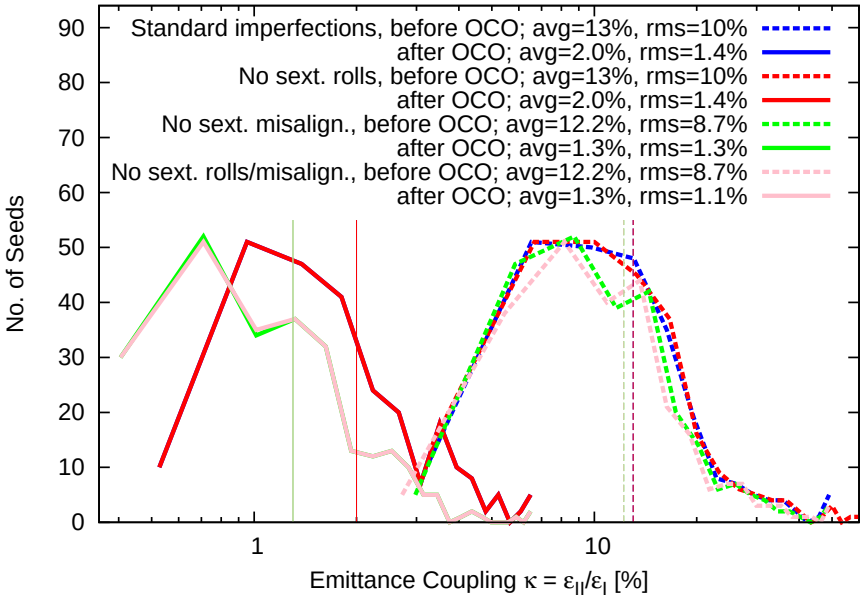


Figure 37: Histogram of emittance coupling results for four different cases: error model including standard imperfections (i.e. with 0.2 mrad RMS sextupole rolls and 25 $\mu$m RMS transverse sextupole misalignment) vs. error model without individual sextupole misalignments vs. error model without individual sextupole rolls vs. error model without individual sextupole misalignments or rolls. Both coupling values before and after orbit correction are shown. Note that the solid blue line is not visible because it is covered entirely by the solid red line. Average values among all 250 seeds per case are indicated by thin lines.

Obviously sextupole transverse misalignments dominate roll errors with respect to emittance coupling. It remains to be identified which type of transverse misalignment has the largest impact. Figure 38 attempts to illustrate the effect of different types of individual sextupole misalignments. It compares emittance coupling results for the standard imperfections model with those for identical models where, however, a specific type of alignment error has been increased: 50 $\mu$m RMS vs. the original 25 $\mu$m RMS for transverse misalignment as well as 0.5 mrad RMS vs. the original 0.2 mrad RMS for the roll errors.

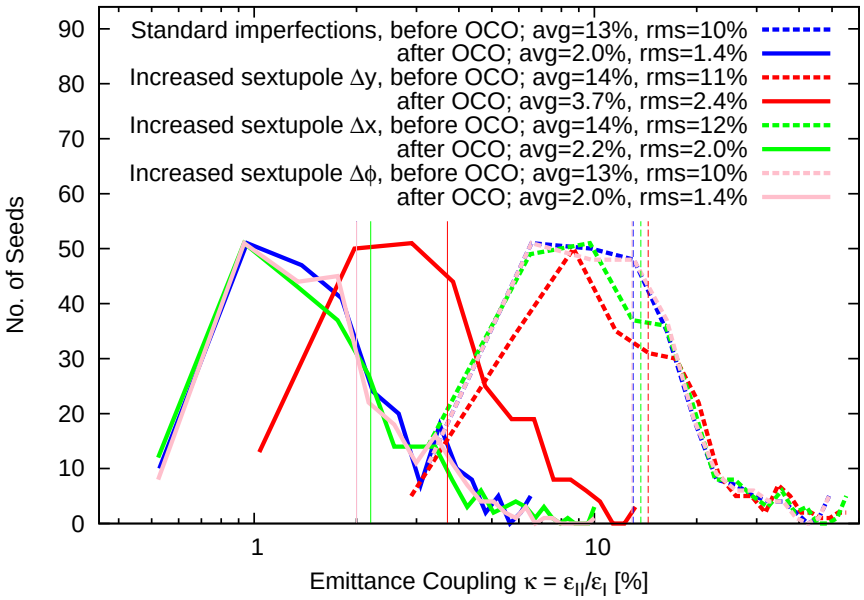


Figure 38: Histogram of emittance coupling results for four different cases: error model including standard imperfections (i.e. with 0.2 mrad RMS sextupole rolls and 25 $\mu$m RMS transverse sextupole misalignment) vs. error model with increased vertical [horizontal] misalignment on individual sextupoles ($\Delta$y [$\Delta$x] = 50 $\mu$m RMS) vs. error model with increased roll errors on individual sextupoles ($\Delta\phi$ = 0.5 mrad RMS). Both coupling values before and after orbit correction are shown. Average values among all 250 seeds per case are indicated by thin lines.

The outcome after orbit correction illustrates clearly that while increased horizontal misalignments and roll errors show little influence on emittance coupling, the increased vertical misalignment sticks out as the error source which actually increases emittance coupling. This increase is quiet significant: compared to the

standard misalignment case, the case with larger vertical misalignment error increases the emittance coupling by 1.7%, i.e. by more than one standard deviation.

As originally suspected, vertically misaligned sextupoles drive coupling through their skew quadrupole feed-down. In fact, one can go so far as to correlate RMS vertical sextupole misalignment with the resulting emittance coupling after orbit correction. This has been done in Fig. 39 where the emittance coupling is displayed for several different assumptions for the vertical sextupole misalignment[10]. For small values of coupling one can easily show that $\Delta\kappa/\kappa \approx \Delta\varepsilon_y/\varepsilon_y$ and hence it comes as no surprise that $\kappa$ can be fitted by a quadratic function in $\Delta y_{\mathrm{sext}}$.

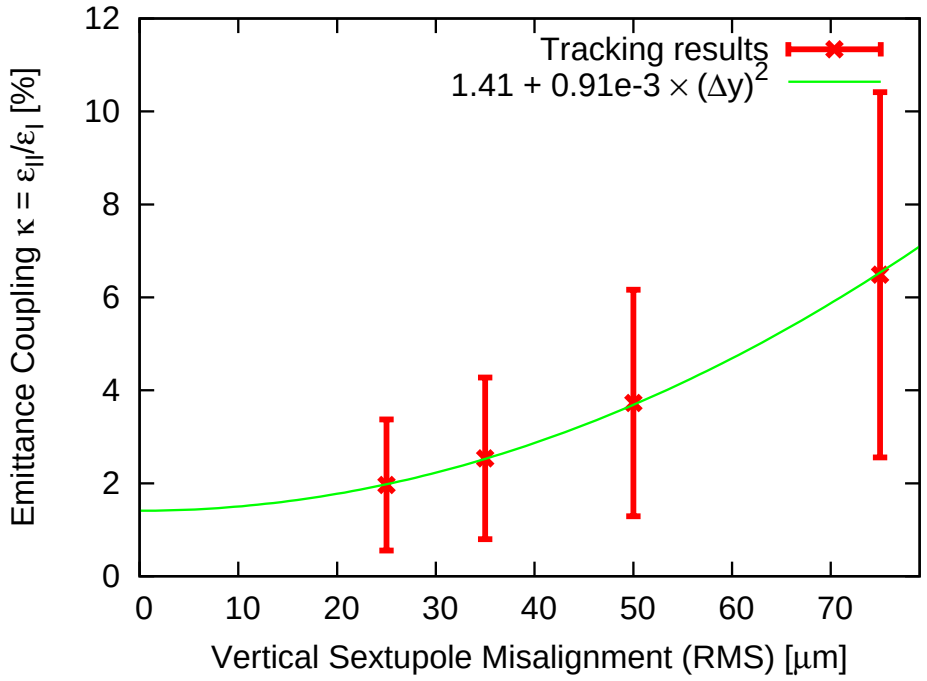


Figure 39: Emittance coupling results (after orbit correction) using the standard imperfections model while varying the RMS vertical sextupole misalignment. The first data point (25 $\mu$m RMS) corresponds to the standard misalignment model. Each data point is the average result across 250 seeds. The error bars indicate the standard deviation across those 250 seeds. The results are compatible with a quadratic fit (indicated).

In fact, Fig. 39 indicates that with the current standard imperfections model,

[10]Note that for the specific case of 75 $\mu$m RMS vertical sextupole misalignment the threader could not find a closed orbit for one seed without ramping up errors.

emittance coupling will always remain above 1.4% regardless of how small the individual vertical sextupole misalignment can be made[11]. This reflects the overall vertical misalignment determined by the girder misalignment as well as other (smaller) sources of coupling. On the other hand, the study also shows that the resulting emittance coupling after orbit correction doubles if the vertical RMS sextupole misalignment is allowed to grow from the original 25 $\mu$m to about 53 $\mu$m.

In summary, passing sextupoles off-center is the dominating source of emittance coupling in this lattice. It is crucial to ensure CODs in the vertical plane are minimized in the sextupoles. It is for this reason that the BPMs in the MAX IV 3 GeV storage ring are installed adjacent to the sextupoles and that these BPMs will be calibrated to the sextupole centers via auxiliary coils on these sextupoles (powered as upright quadrupoles). Obviously there are more sextupoles than correctors and BPMs in the lattice, so not all sextupoles can be passed exactly at their centers. However, BPMs have been installed closest to the strong SFi/o/m sextupoles in order to ensure vertical CODs can be minimized primarily in locations where they drive coupling most.

The roughly 2% emittance coupling that are achieved after orbit correction assuming imperfections are roughly compatible with the standard error models can certainly be deemed acceptable. The baseline requirement of 8 pm rad vertical emittance calls for 2.4%. However, in order to achieve highest brightness a more optimized coupling setting has to be contemplated (cf. Section 4.4). Therefore, in the future, required coupling values could end up lying around 0.6%. This is beyond what can be expected with improvements such as beam-based girder re-alignment (cf. Section 4.3.2) and must therefore be achieved with more sophisticated correction. One such possibility is local betatron coupling control in connection with cancelation of spurious vertical dispersion via excitation of auxiliary coils on the sextupoles and octupoles that act as weak local skew quadrupole correctors. This shall be the topic of future studies.

[11] It is interesting to note here that Fig. 37 indicates that emittance coupling without any transverse misalignment of the sextupoles is 1.3% (after orbit correction) which is perfectly compatible to the fit presented here.

## 4.4 Emittance, Intrabeam Scattering, Touschek Lifetime

The ultralow emittance of the MAX IV 3 GeV storage ring has two interesting consequences:

- The equilibrium emittance is determined by both the lattice and the ID gap settings (at any given time).
- The equilibrium emittance is determined by both the lattice/ID emittance and intrabeam scattering (IBS).

The first point means that the emittance in the MAX IV 3 GeV storage ring is not necessarily a constant, but can change throughout the course of a user run as a consequence of gap changes in the various IDs installed in the machine. This is in stark contrast to existing 3rd generation light sources where the resulting emittance is usually dominated by the magnetic lattice and hence remains constant. This behavior is caused by an unusual property of the MAX IV 3 GeV storage ring: the total radiated power is not dominated by dipole radiation (which would remain constant), but to a significant amount by ID radiation which is of course a function of ID gap settings at any given time. Hence, the total radiated power (and with it the RF acceptance) are not roughly constant, as is usually the case in existing 3rd generation light sources, but rather a quantity that can vary considerably throughout a typical user run.

The second point means that the transverse emittance in the MAX IV 3 GeV storage ring varies as a consequence of changes in stored charge and longitudinal phase space; again a characteristic not usually observed in existing 3rd generation light sources. As current decays in the MAX IV 3 GeV storage ring, the emittance will drop[12]. Furthermore, a change of energy spread (as a consequence of e.g. ID gap changes) or bunch length (by e.g. modifying the main cavity voltage or changing the frequency of the harmonic Landau cavities) will lead to a change in transverse emittance. This last point is most crucial: since IBS depends heavily on the charge density in 6D phase space, the applied cavity voltage and bunch lengthening from Landau cavities (LCs) governs the resulting emittance. Since Touschek lifetime also depends strongly on charge density in 6D phase space it varies as a function of overall emittance including IBS as well as bunch lengthening. Because of this nontrivial interplay between several factors in the realistic machine, the plan here will be to investigate several "base line" configurations of the MAX IV 3 GeV storage ring and then show consequences for variations of specific parameters like main cavity

[12]Note, however, that during user shifts, top-up operation is foreseen so changes in the amount of stored charge should be very limited.

voltage, bunch lengthening achieved with the LCs, or single-bunch charge.

### 4.4.1 Momentum Acceptance and Touschek Lifetime

The first set of calculations shall be carried out assuming 500 mA stored beam current in all buckets with no ion-clearing gap, i.e. an "even fill" which gives 5 nC charge per bunch. The MAX IV 3 GeV storage ring has six main RF cavities for a maximum overall accelerating voltage of 1.8 MV. For a bare lattice ($E_{\mathrm{loss}} = 363.8\,\mathrm{keV/turn}$) this corresponds to an RF acceptance of $\delta_{\mathrm{RF}} = 7.062\%$. The lattice and nonlinear optics were designed and tuned to exceed a minimum momentum acceptance (MA) of 4.5% everywhere. Momentum acceptance tracking performed with OPA (using a parametric/5D approximation to calculate lattice MA) as well as with TRACY-3 (using full 6D phase space to calculate lattice MA) can be applied to verify. This is shown in Fig. 40.

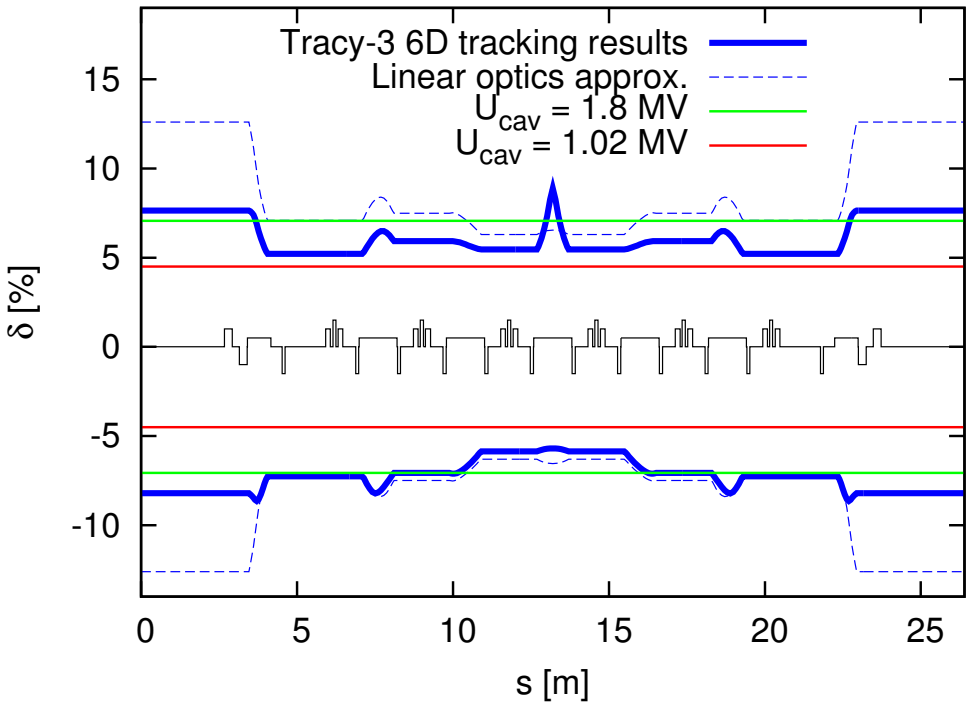


Figure 40: Lattice momentum acceptance for one achromat of the MAX IV 3 GeV storage ring. A bare lattice with actual vacuum chamber apertures has been used. For comparison, RF acceptance is shown as well: cavities at maximum voltage 1.8 MV (green line, corresponds to 7.062% MA) and at 1.02 MV corresponding to 4.5% RF acceptance (red line).

The linear approximation shown in Fig. 40 is calculated according to

$$\delta_{\mathrm{acc}}(s_0) = \min_{\forall s} \left[ \frac{a_x(s)}{\left( \sqrt{\mathcal{H}_{s_0} \beta_x(s)} + \eta_x(s) \right)} \right]. \tag{1}$$

For the tracking studies, tracking was performed for one synchrotron period using actual vacuum apertures. The resulting lattice MA is below the maximum RF acceptance in the arc (where dispersion increases but vacuum apertures remain roughly constant), but clearly always beyond the originally specified 4.5%. The minimum lattice MA recorded was $-5.7\%$ right at the center of the achromat and $+5.2\%$ in the short straights. The asymmetry in the resulting overall MA is a signature of asymmetric chromaticity (cf. Fig. 3) which can also be recognized in the off-momentum DA (cf. Fig. 6).

The overall MA is determined for every location in the lattice as the minimum between lattice MA and RF acceptance at that location. This means that the RF determines the overall MA in the long straights, while the lattice dominates in the arcs as long as sufficient cavity voltage is available. If the cavity voltage drops below $\approx 1.2\,\mathrm{MV}$ the RF acceptance ($\approx 5.2\%$) drops below the minimum lattice MA and therefore determines the overall MA everywhere in the lattice[13]. On the other hand, as long as sufficient RF voltage is available, the resulting overall MA will exceed the originally specified 4.5% throughout the entire lattice.

This interplay between RF acceptance and lattice MA can be nicely recognized when inspecting Touschek lifetime as shown in Fig. 41. The bare lattice losses are 364 keV/turn so the RF acceptance is just above zero at 0.4 MV cavity voltage. From there it rises towards around 7% for the maximum cavity voltage of 1.8 MV. The Touschek lifetime rises along with the RF acceptance up to about 1.2 MV or 5.2% RF acceptance. At this point the approximation for the Touschek lifetime using the RF acceptance as the overall MA starts deviating from the exact Touschek lifetime. The reason for this is that the RF acceptance now starts to exceed the lattice MA in certain areas of the lattice. When the cavity voltage is then further increased, the overall MA remains roughly constant (as it is dominated by the lattice MA) while the bunch length continues to shorten as can also be seen in Fig. 41. As a consequence, the Touschek lifetime actually starts to reduce. This is clearly seen above 1.4 MV where any further increase of cavity voltage only serves to shorten the bunch (without actually increasing the overall MA) and therefore reduces Touschek

[13]This situation allows a very quick Touschek lifetime calculation as opposed to the usual situation where the local lattice MA has to first be determined via tracking for the entire lattice before Touschek lifetime can be calculated [11].

lifetime[14]. In the real machine the cavity voltage would be adjusted accordingly: i.e. maximize Touschek lifetime instead of trying to maximize the RF acceptance.

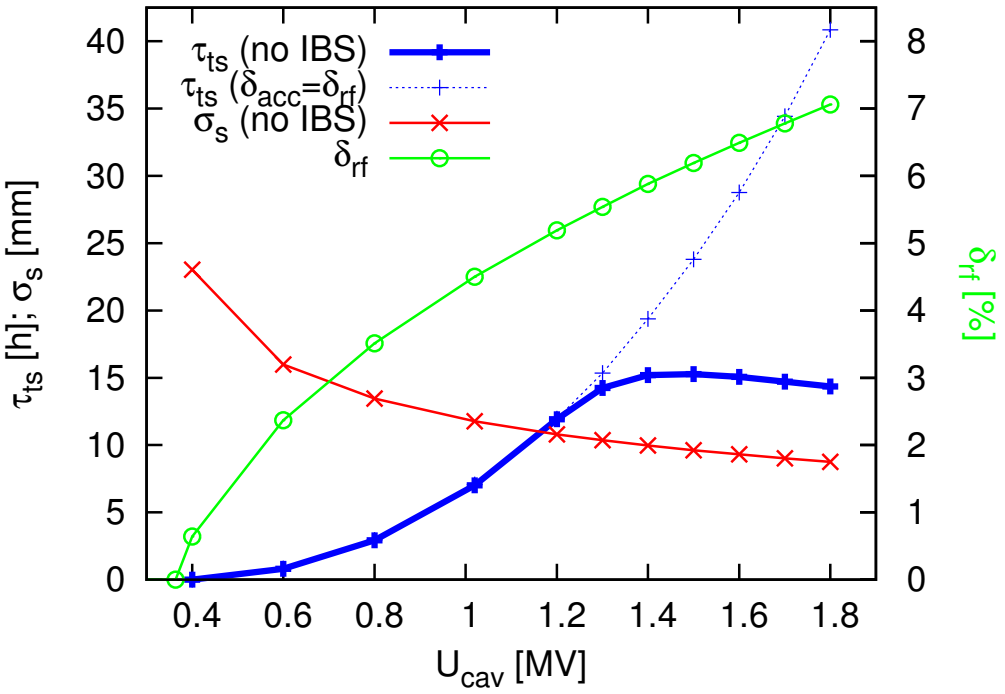


Figure 41: Touschek lifetime, bunch length, and RF acceptance as functions of the RF cavity voltage. The stored current was assumed to be 500 mA with the vertical emittance set to 8 pm rad. Bunch lengthening from Landau cavities and the effects of IBS have not been included. The calculated Touschek lifetime is based on resulting overall MA from tracking and actual vacuum apertures. The dashed line shows an approximation in which the MA is given by the RF acceptance.

However, as pointed out at the beginning of this Section, the charge density in the bunch acts back on the resulting bunch emittance through IBS. Since the cavity

[14]Note that this behavior changes somewhat when the bunches are stretched with LCs. In this case the Touschek lifetime stays roughly constant above a certain cavity voltage, however, the transverse emittance continues to grow as a consequence of increased IBS blow-up due to the shortened bunch (cf. below). Therefore, in the interest of reducing electric power consumption *and* limiting emittance growth from IBS, the cavity voltage should be adjusted to the value at which lifetime just starts to taper off.

voltage (together with the radiation losses) determines the bunch length (in absence of LCs), and since the bunch length variations change the bunch charge density, there is a direct influence of RF cavity voltage on bunch emittance. With 500 mA stored in the MAX IV 3 GeV storage ring in an even fill, IBS leads to a substantial increase of the bunch emittance in all three planes: the bunch length is stretched (along with the bunches' energy spread) while the transverse emittances are blown up. Even if it is assumed that skew quadrupoles allow setting the emittance coupling freely so as to maintain the vertical emittance at a certain value (e.g. 8 pm rad), the horizontal emittance will vary as a function of main cavity voltage. This can be recognized in Fig. 42. As the cavity voltage is increased, the bunch length decreases.

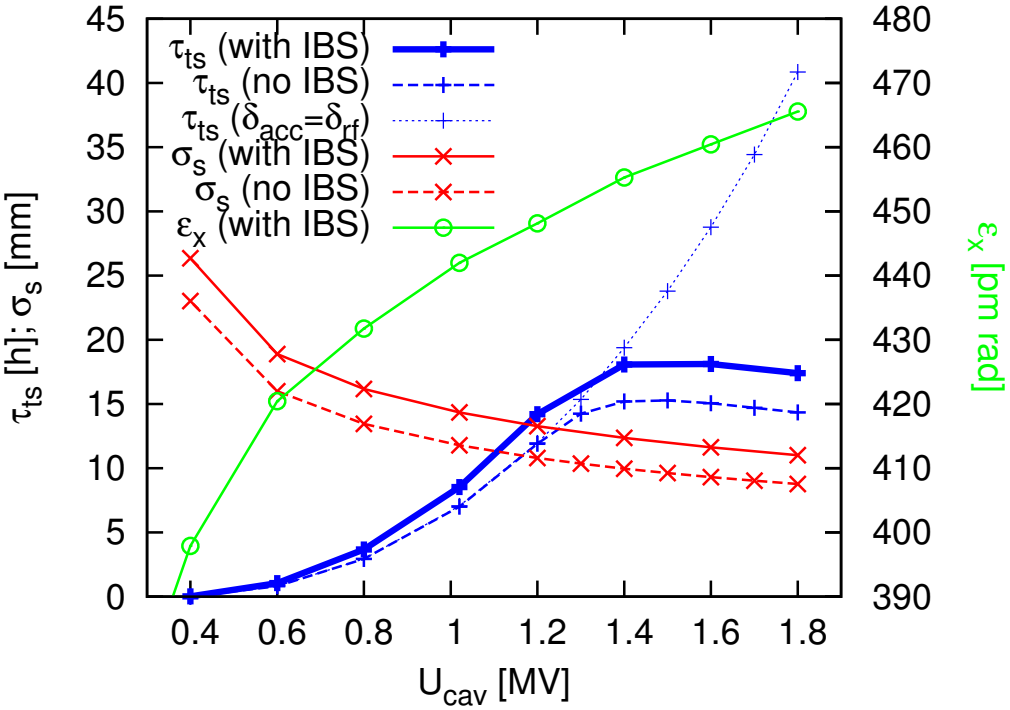


Figure 42: Touschek lifetime, bunch length, and horizontal emittance as functions of the RF cavity voltage. The stored current was assumed to be 500 mA with the vertical emittance always set to 8 pm rad. Bunch lengthening from Landau cavities has not been included. The calculated Touschek lifetime is based on resulting overall MA from tracking and actual vacuum apertures.

Compared to the zero-current situation (i.e. when neglecting IBS) the bunch length

is increased by roughly 3 mm for a bunch charge of 5 nC as a consequence of IBS. Apart from this extra bunch lengthening, the bunch length still steadily decreases as the RF voltage is increased. However, as the bunch length reduces, the charge density grows thus increasing the emittance blow-up caused by IBS. This can also be recognized in Fig. 42: at zero current the horizontal emittance is 320 pm rad (assuming the vertical emittance is set to 8 pm rad), but in the presence of IBS at 500 mA, this value is raised to almost 400 pm rad at the lowest possible cavity voltage (and consequently the longest possible bunch). As the cavity voltage is raised, the bunch becomes shorter, IBS stronger, and the emittance is eventually pushed to 464 pm rad, corresponding to a 45% increase in horizontal emittance.

As one can gather from observing the Touschek lifetime in Fig. 42, IBS helps with lifetime as one would expect because it reduces the charge density in phase space. Although lifetime improvements are welcome, IBS is nevertheless not a desired mechanism as it also carries the penalty of increased transverse emittance, i.e. an increase in source size. In fact, IBS does even more harm. Most often, the vertical beam size is lowered to match a specified diffraction limit and/or improve the matching of the electron beam to the photon beam emerging from an ID. This usually carries a lifetime penalty, however, in the presence of IBS this penalty becomes two-fold as a reduction in vertical beam size also leads to additional blow-up in the horizontal. One is faced with a situation where the lifetime has been reduced yet the horizontal source size has increased—the exact opposite of the usually encountered behavior. The introduction of LCs in order to stretch bunches presents a possible remedy for this conundrum imposed by strong IBS. The MAX IV 3 GeV storage ring has three passive LCs operated at the third harmonic that should allow bunch lengthening up to roughly 58 mm [12]. For the bare lattice and a main cavity voltage of 1.8 MV the natural bunch length is 8.76 mm. For a stored current of 500 mA in an even fill IBS will increase this bunch length to 11.01 mm. As the Landau cavities are tuned in the bunch length can be increased. Figure 43 shows the evolution of Touschek lifetime and emittance (under the influence of IBS) as the bunches are stretched.

IBS increases both the bunch length and the transverse emittance. Meanwhile, the Touschek lifetime increases linearly with the bunch length as one would expect. This holds both for the zero-current case as well as for strong IBS at 500 mA stored current. The emittance blow-up caused by IBS is, however, strongly reduced when the LCs have fully stretched the bunches. While the horizontal emittance blow-up from IBS is 45% at the natural bunch length, this blow-up is reduced to 13% when the bunches have been stretched by roughly a factor 5. This is a dramatic illustration of how bunch elongation with LCs effectively allows the ultralow lattice

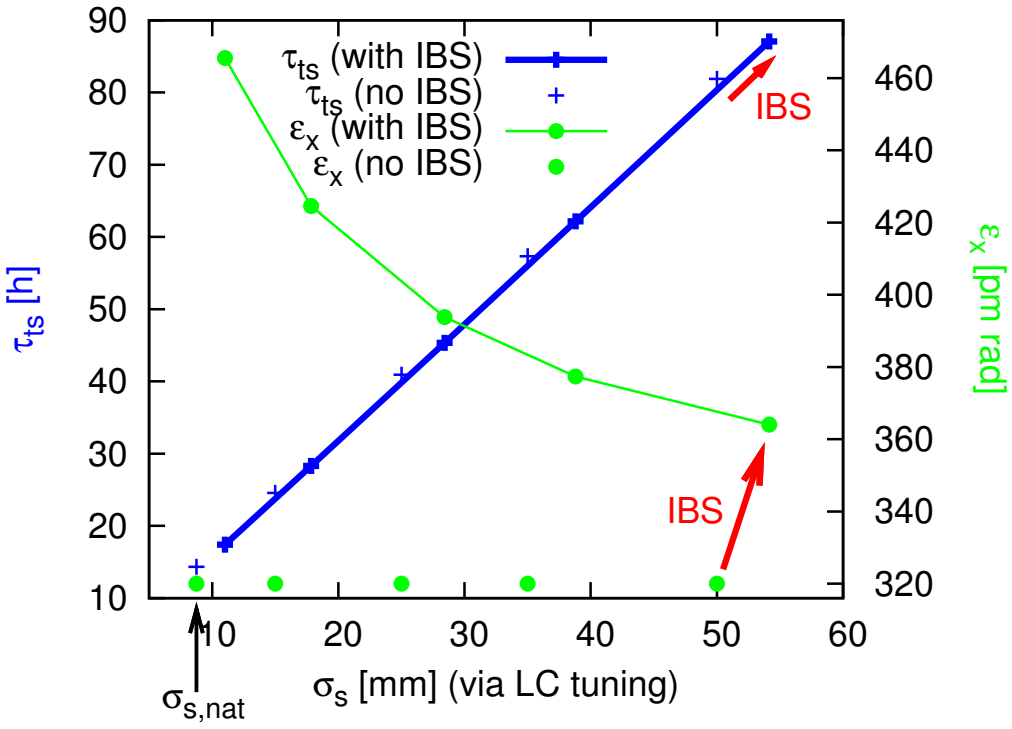


Figure 43: Touschek lifetime and horizontal emittance as functions of bunch length which is adjusted by tuning the LCs. The stored current was assumed to be 500 mA with the vertical emittance always set to 8 pm rad. The calculated Touschek lifetime is based on resulting overall MA from tracking and actual vacuum apertures. The emittance blow-up and bunch length increase from IBS as well as the associated lifetime increase are indicated.

emittance to be exploited even at high stored current (cf. also Fig. 45).

The effect of LCs on Touschek lifetime for different settings of emittance coupling (again assuming skew quadrupoles are available for such adjustment) are given in Table 10. A vertical emittance set to 8 pm rad (emittance coupling $\kappa = 2.5\%$) corresponds to the 1 Å diffraction limit. As has however been pointed out [13], a better matching to a photon beam coming from a typical ID can be achieved if the coupling is reduced to about 0.6% (zero-current setting) so that the vertical emittance is adjusted to 2 pm rad ("high-brightness mode"). The table gives values assuming maximum RF acceptance (1.8 MV cavity voltage corresponding to $\delta_{\rm rf} = 7.062\%$). The recorded lifetime with Landau cavities appears to be more than sufficient, and

is in fact very high[15].

Table 10: Overview of emittances, IBS (assuming 500 mA stored current in an even fill), and Touschek lifetime for different configurations of the bare lattice as calculated by tracking in TRACY-3 with actual vacuum apertures. The synchrotron radiation losses for this bare lattice are 364 keV/turn. The cavity voltage has been set to 1.8 MV which corresponds to $\delta_{\mathrm{rf}} = 7.062\%$.

| | $\kappa$ | $\varepsilon_y$ [pm rad] | $\varepsilon_x$ [pm rad] | $\sigma_s$ [mm] | $\sigma_\delta \times 10^3$ | $\tau_{\mathrm{ts}}$ [h] |
|---|---|---|---|---|---|---|
| **1 Å diffraction limit, no LCs** | | | | | | |
| no IBS | 2.5% | 8 | 320 | 8.76 | 0.7727 | 14.35 |
| IBS incl. | 1.7% | 8 | 466 | 11.01 | 0.9713 | 17.41 |
| **1 Å diffraction limit, LCs tuned in** | | | | | | |
| no IBS | 2.5% | 8 | 320 | 50.00 | 0.7727 | 81.90 |
| IBS incl. | 2.2% | 8 | 364 | 54.15 | 0.8368 | 87.08 |
| **High-brightness mode, no LCs** | | | | | | |
| no IBS | 0.6% | 2 | 326 | 8.76 | 0.7727 | 7.12 |
| IBS incl. | 0.4% | 2 | 552 | 12.15 | 1.072 | 9.60 |
| **High-brightness mode, LCs tuned in** | | | | | | |
| no IBS | 0.6% | 2 | 326 | 50.0 | 0.7727 | 40.63 |
| IBS incl. | 0.5% | 2 | 404 | 57.74 | 0.8875 | 45.85 |

Despite the apparently large Touschek lifetime recorded here, one must recall that it is not suggested to operate at such high RF acceptance as this (a) unnecessarily shortens the bunches which in turn increases IBS blow-up and reduces lifetime (cf. p. 60) and (b) increases electric power consumption. Therefore, a second set of results is presented at the other end of the RF acceptance range. Table 11 shows results where the RF acceptance has been set to 4.5% (1.02 MV cavity voltage) so that it dominates the resulting overall MA. Again, the recorded lifetime can be deemed more than sufficient when the Landau cavities are tuned in. This is a very important result considering the storage ring will eventually be filled up with IDs. With the amount of RF cavities and RF voltage available, it should always be possible to supply 4.5% RF acceptance regardless of number of IDs or their gap settings and with

[15]This is, however, absolutely necessary because at this point errors have not yet been factored in. A quantitative analysis of this effect will be delivered in Section 4.4.2.

it—assuming the effect of imperfections (cf. the next section) can be limited—an adequate Touschek lifetime.

Table 11: Overview of emittances, IBS (assuming 500 mA stored current in an even fill), and Touschek lifetime for different configurations of the bare lattice as calculated by tracking in TRACY-3 with actual vacuum apertures. The synchrotron radiation losses for this bare lattice are 364 keV/turn. The cavity voltage has been set to 1.02 MV which corresponds to $\delta_{\mathrm{rf}} = 4.5\%$.

| | $\kappa$ | $\varepsilon_y$ [pm rad] | $\varepsilon_x$ [pm rad] | $\sigma_s$ [mm] | $\sigma_\delta \times 10^3$ | $\tau_{\mathrm{ts}}$ [h] |
|---|---|---|---|---|---|---|
| **1 Å diffraction limit, no LCs** | | | | | | |
| no IBS | 2.5% | 8 | 320 | 11.78 | 0.7727 | 7.00 |
| IBS incl. | 1.8% | 8 | 442 | 14.34 | 0.9412 | 8.53 |
| **1 Å diffraction limit, LCs tuned in** | | | | | | |
| no IBS | 2.5% | 8 | 320 | 50.00 | 0.7727 | 29.72 |
| IBS incl. | 2.2% | 8 | 364 | 54.15 | 0.8368 | 32.08 |
| **High-brightness mode, no LCs** | | | | | | |
| no IBS | 0.6% | 2 | 326 | 11.78 | 0.7727 | 3.48 |
| IBS incl. | 0.4% | 2 | 519 | 15.74 | 1.033 | 4.73 |
| **High-brightness mode, LCs tuned in** | | | | | | |
| no IBS | 0.6% | 2 | 326 | 50.00 | 0.7727 | 14.77 |
| IBS incl. | 0.5% | 2 | 404 | 57.43 | 0.8875 | 16.99 |

### 4.4.2 Touschek Lifetime in the Presence of Imperfections

As indicated above, the question now arises if the long Touschek lifetime can be preserved in the presence of imperfections. Section 4.2 showed how errors reduce achievable on and off-momentum DA, and therefore, Touschek tracking will reveal that errors reduce the achievable Touschek lifetime as a consequence of reduced DA. At maximum RF voltage a Touschek lifetime without bunch lengthening from Landau cavities of 14.35 h was recorded (cf. Table 10). When all expected sources of imperfections are added and orbit correction is performed before the Touschek tracking is carried out, a Touschek lifetime of 11.0 h with an RMS of 0.8 h is recorded. The error seeds used in theses calculations are the same as those used to calculate the DA displayed in Fig. 14. For each of these seeds a Touschek lifetime is derived

from tracking giving the mean value and RMS over 20 seeds quoted here. The seeds used here are also identical to the first 20 used to generate the CODs and coupling displayed in Figs. 21–23 as well as Table 7.

The reduction in Touschek lifetime from the above mentioned imperfections appears to be roughly 23%. However, as further analysis shows, an additional reduction of Touschek lifetime has to be expected from in-vacuum IDs and/or narrow-gap ID chambers that limit the vertical acceptance to the point where Touschek scattered particles—in the presence of nonzero betatron coupling—are lost in the vertical plane. A typical IVU with 3.7 m length and gap closed to 4 mm imposes a vertical acceptance limit of $A_y = 1.1\,\mathrm{mm\,mrad}$ compared to the $A_y = 7.5\,\mathrm{mm\,mrad}$ of the bare machine. The 23% reduction of Touschek lifetime due to imperfections stated above results from a model where the vertical acceptance of the bare machine has been assumed. If the limiting vertical acceptance of the 4 mm gap of a 3.7 m long IVU is included in the model (while using the same seeds), the Touschek lifetime reduces to 9.4 h (1.3 h RMS) which corresponds to a reduction of 34% compared to the ideal machine. Fortunately, commissioning of the storage ring will take place without in-vacuum IDs or narrow-gap chambers so the full vertical acceptance should be available (assuming it is not limited by obstructions or crude misalignments of the chamber).

On the other hand, as pointed out in previous sections, during early commissioning imperfections are assumed to be larger than in the model used here. Touschek tracking has been repeated assuming these increased levels of field errors and misalignments. The seeds used for tracking are the same as those used to calculate the DA displayed in Fig. 17 as well as the first 20 seeds used to generate the CODs and coupling shown in Figs. 28–30. In fact, the situation corresponds exactly to what was discussed in Section 4.3.1. The resulting Touschek lifetime is calculated to be 6.7 h (1.3 h RMS) which is a 53% reduction compared to the ideal Touschek lifetime. This is a rather dramatic reduction and therefore presents another clear motivation for performing beam-based shunting and re-alignment during early commissioning.

Finally, Touschek tracking was also performed with the long-term goals in mind. Assuming that eventually beam-based shunting and re-alignment are successful in reducing overall imperfections to the very low levels discussed in Section 4.3.2, the Touschek lifetime should approach the values recorded for the ideal machine, considering that for such a situation the DA approaches on average the physical acceptance (cf. Fig. 15). The Touschek tracking studies were repeated using the exacts same seeds as used to prepare the DA displayed in Fig. 15 as well as the first 20 seeds used to generate the CODs and coupling shown in Figs. 32–34. These runs result in a Touschek lifetime of 11.3 h (0.9 h RMS) which is a 21% reduction compared

to the ideal Touschek lifetime. As pointed out above, this reduction is the result of imperfections *and* limited vertical acceptance of a machine equipped with IVUs and narrow-gap ID chambers. If the same seeds are used for Touschek tracking, but this time assuming the full vertical acceptance of the bare machine is available, the Touschek lifetime ends up at 12.1 h (0.6 h RMS) which corresponds to a reduction of 16% compared to the ideal machine.

In summary, if imperfections are corrected to a sufficient degree and Landau cavities can be tuned in to lengthen bunches as designed, Touschek lifetime should remain between 25 h for 4.5% MA (corresponding to 10 h overall lifetime) and 69 h for 7% MA (corresponding to 14 h overall lifetime) and therefore definitely beyond the original goal of 24 h (designed to give 10 h overall lifetime factoring in 25 h elastic scattering lifetime and 56 h inelastic scattering lifetime [5]). For the high-brightness mode a Touschek lifetime between 13 h (for 4.5% MA) and 36 h (for 7% MA) is expected leading to an overall lifetime between 8 h and 12 h. And as pointed out in Section 4.4.1, peak Touschek lifetime could in principle lie even higher if the cavity voltage is adjusted for optimum bunch length rather than maximum RF acceptance.

### 4.4.3 Connecting Touschek Lifetime, LCs, Emittance, and IBS

A special property of this ultralow emittance lattice is that Touschek lifetime rises as the emittance decreases. As already pointed out on p. 57 closing the gaps of strong IDs or reducing the charge per bunch will lower the equilibrium emittance in the storage ring. When this happens, the Touschek lifetime in the MAX IV 3 GeV storage ring—unlike existing 3rd generation synchrotron sources—will increase. The reason for this behavior lies in the ultralow lattice emittance. At such low transverse emittance the available transverse momenta are no longer sufficient to create large enough longitudinal momentum deviations extending beyond the RF bucket, i.e. create Touschek losses. Most of the scattering among electrons in the bunch will lead to an increase of emittance (as in IBS) via momentum transfer from one plane to another, but only very few events will be able to transfer enough momentum into the longitudinal plane so that particles are scattered outside of the RF bucket as is the case for Touschek scattering. Therefore, the Touschek lifetime is rather high in the MAX IV 3 GeV storage ring and becomes better as the emittance is further reduced. An illustration of this characteristic is given in Fig. 44 where the resulting Touschek lifetime (assuming 500 mA stored current) is plotted against equilibrium emittance. The underlying assumption is that the lattice emittance can be varied freely while holding the energy spread constant. For the plot shown in Fig. 44 the overall MA is set to 4.5% for all points. The vertical emittance is assumed to be

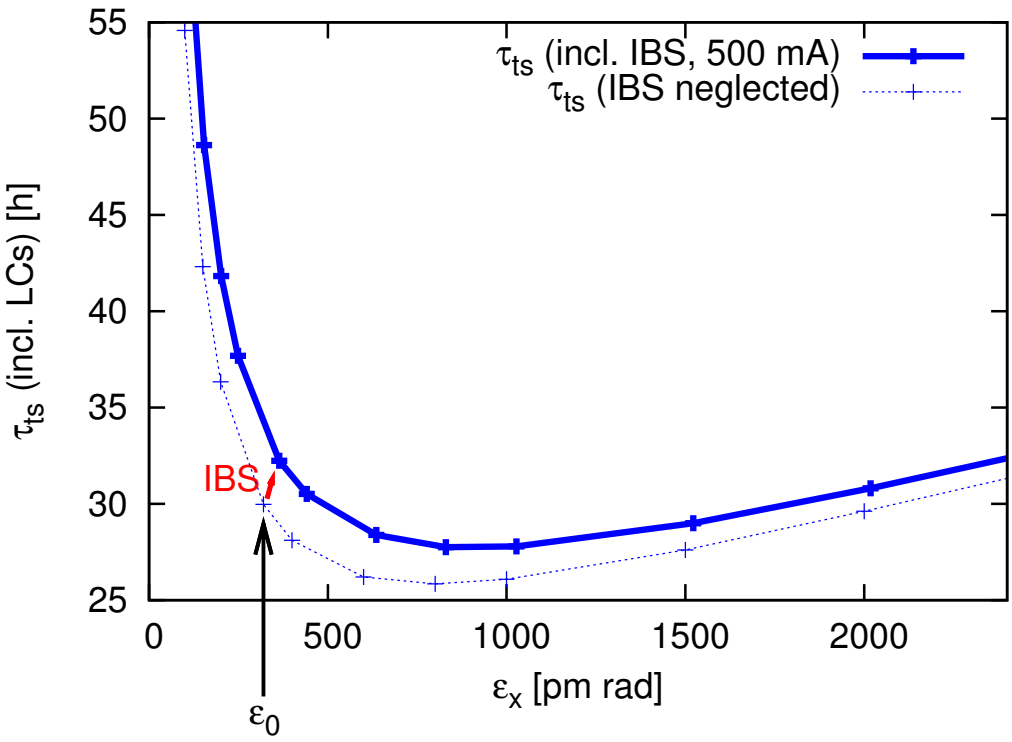


Figure 44: Touschek lifetime as a function of equilibrium emittance. The underlying assumption is that the lattice emittance can be adjusted freely while keeping the energy spread constant. The overall MA has been set to 4.5% and the vertical emittance is always adjusted to 8 pm rad. The effect of IBS (at 500 mA stored current) and LCs is included. The equilibrium emittance of the MAX IV 3 GeV storage ring bare lattice is indicated.

adjusted to a constant 8 pm rad. The effect of the Landau cavities is included. The plot shows two vastly different regimes: one above roughly 1 nm rad where lowering the emittance (e.g. lowering the bunch volume and thus increasing the charge density in the bunch) leads to a decrease in lifetime and one below roughly 800 pm rad where any decrease in emittance leads to an improvement in Touschek lifetime. It's also notable that below 300 pm rad this lifetime increase becomes quite dramatic. Since the MAX IV 3 GeV ring is clearly operated in the regime where the lifetime increases as the emittance is lowered it is especially important to consider how emittance growth from IBS can be prevented. As indicated in Fig. 44, IBS blows up the emittance and hence the resulting lifetime is not as high as it would be for the zero-current case. The LCs have already been shown to be an effective method to

mitigate the effect of IBS at high stored current, but the question arrises if this method remains effective for very low emittance, e.g. when many strong IDs are installed in the storage ring and operated at very low gap settings.

Figure 45 attempts to illustrate the benefit of LCs for different equilibrium emittance. Again the underlying assumption is that the lattice emittance can be varied

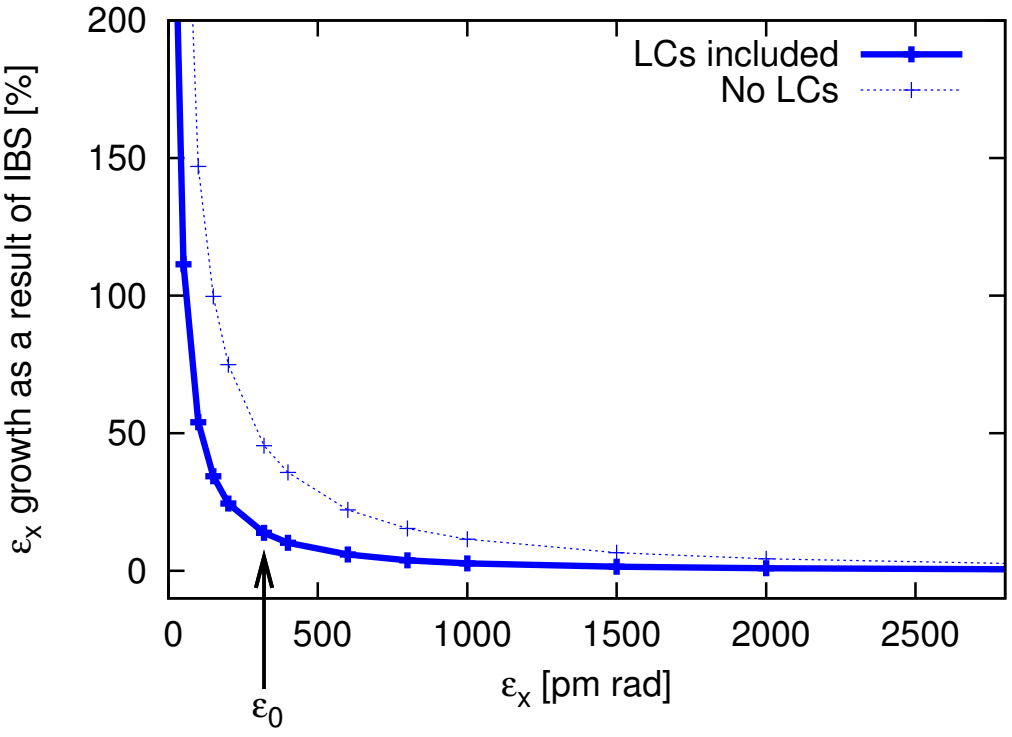


Figure 45: Horizontal emittance growth caused by IBS at 500 mA stored current as a function of equilibrium emittance. The underlying assumption is that the lattice emittance can be adjusted freely while keeping the energy spread constant. The overall MA has been set to 4.5% and the vertical emittance is always adjusted to 8 pm rad. The effect of the LCs is shown. The equilibrium emittance of the MAX IV 3 GeV storage ring bare lattice is indicated.

while the energy spread is held constant. The emittance blow-up at 500 mA caused by IBS is then shown for different values of the equilibrium emittance both with and without LCs used to stretch the bunches. For all cases, the overall MA is assumed to be 4.5% and the vertical emittance is always adjusted to 8 pm rad. It is quite clear that the LCs allow pushing to lower lattice emittance without suffering too severe blow-up from IBS compared to running without LCs. On the other had, even with

bunch lengthening from LCs, once lattice emittance is reduced below 100 pm rad, the emittance is blown up by 50% and more by IBS. A push to further reduce the lattice emittance without any attempt at reducing the charge (density) in the bunch starts to appear as a rather unbalanced "brute-force" approach.

The benefit of LCs in the MAX IV 3 GeV storage ring is quite clear. However, upon closer inspection one must also notice that while the emittance blow-up caused by IBS at 500 mA is 13% (cf. Figs. 43 and 45, Table 10), the lifetime increase caused by this dilution of charge density in the bunch remnains substantially below 10% (cf. Fig. 43 and Tables 10 and 11). Immediately the question arrises if this is overall still an advantageous trade-off and if a reduced bunch charge possibly presents an interesting alternative. Figure 46 attempts to summarize the evolution of the horizontal emittance under the influence of IBS at 500 mA for different amounts of bunch charge. Regardless of the choice of vertical emittance, the emittance blow-up

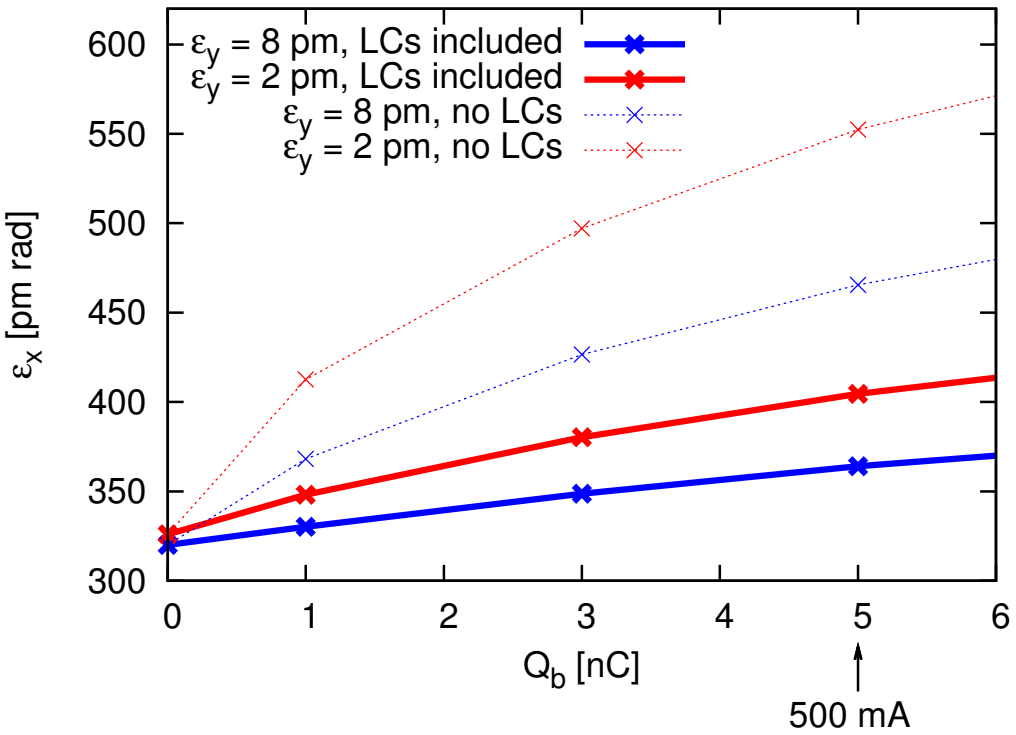


Figure 46: Horizontal emittance including the effect of IBS as a function of bunch charge for two different settings of vertical emittance. The overall MA has been set to 4.5%. The effect of the LCs is shown. The bunch charge corresponding to 500 mA stored current in the MAX IV 3 GeV storage ring is indicated.

caused by IBS is clearly recognized. The capability of the LCs to reduce the impact of this effect are also clearly displayed. Without Landau cavities the blow-up is very strong, especially for small coupling settings.

The electron beam brightness is determined by both the emittance and the bunch charge. Since the emittance keeps growing with the charge, the question immediately arises if the electron beam brightness "saturates" as a result of IBS or if there possibly exists an optimum choice of bunch charge considering the effect of IBS. Figure 47 shows the electron brightness for different bunch charge and vertical emittance choices both with and without Landau cavities. Within the relevant range,

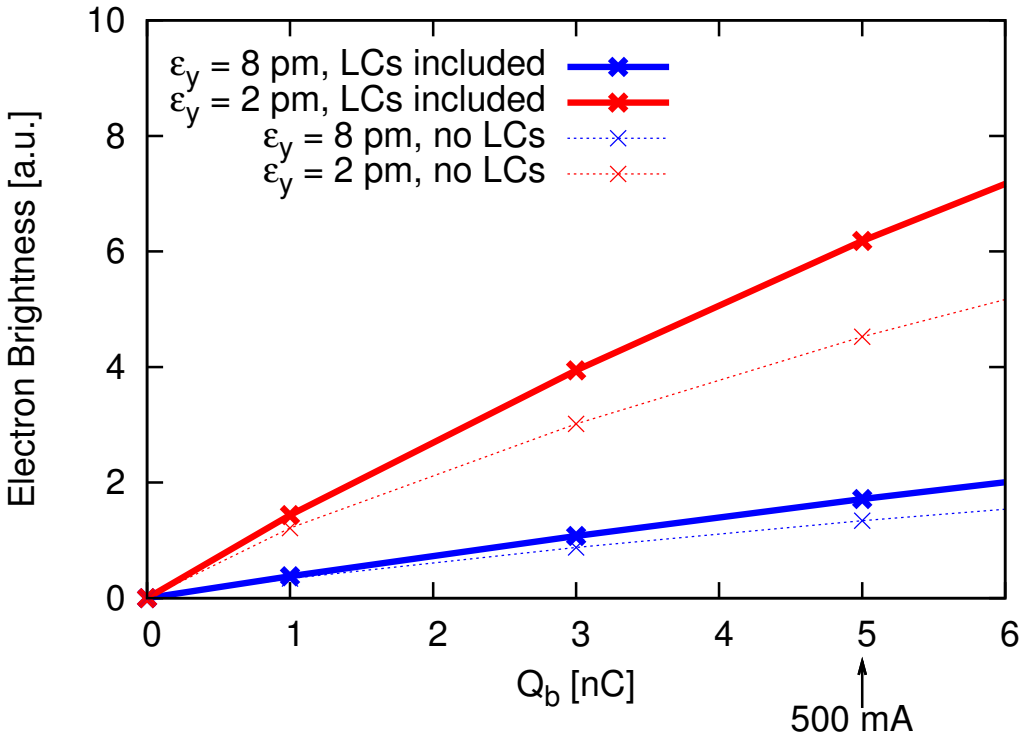


Figure 47: Electron brightness including the effect of IBS as a function of bunch charge for two different settings of vertical emittance. The overall MA has been set to 4.5%. The effect of the LCs is shown. The bunch charge corresponding to 500 mA stored current in the MAX IV 3 GeV storage ring is indicated.

no saturation of the electron brightness can be recognized as a result of IBS. More charge always leads to higher electron brightness, however, this growth is not linear.

However, as pointed out in [13] the ultimate benchmark for a storage ring-based

synchrotron sources is the photon brightness which itself is a convolution of the electron *and* intrinsic photon beam emittance. Since the latter depends on the parameters of the ID, different cases have to be considered. Instead of chasing a global optimum to achieve maximum electron brightness, the electron beam should ideally be matched to the intrinsic photon beam emerging from a specific ID with its individual gap setting in order to deliver maximum photon brightness for a specific application. In Fig. 48 the resulting photon brightness is displayed assuming a typical in-vacuum undulator for the MAX IV 3 GeV storage ring. For this example

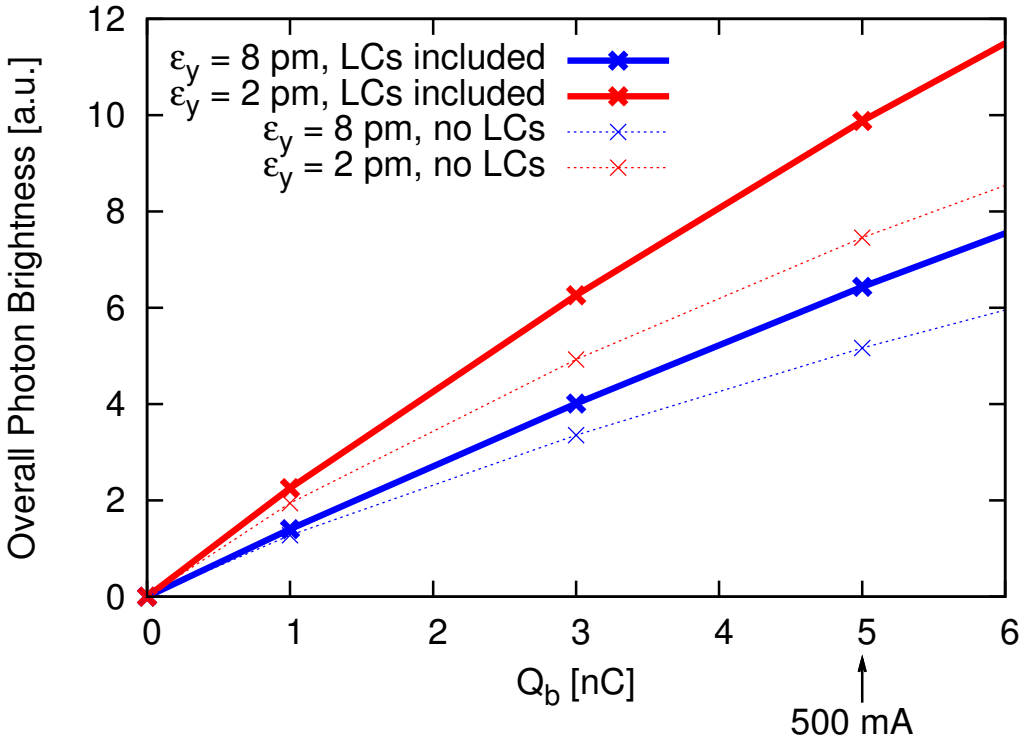


Figure 48: Overall photon brightness including the effect of IBS as a function of bunch charge for two different settings of vertical emittance. The ID is assumed to be 4 m long and tuned to emit radiation at 1 Å. The overall MA has been set to 4.5%. The effect of the LCs is shown. The bunch charge corresponding to 500 mA stored current in the MAX IV 3 GeV storage ring is indicated.

the assumption is that the ID has a length of 4 m and is tuned to emit photons at 1 Å.

As is quite common for existing storage ring-based light sources, despite being

well matched in the vertical plane, the electron beam is poorly matched to the photon beam in the horizontal plane as a result of its sheet-like form. The matching in the vertical plane can be improved for such hard radiation by reducing the electron beam emittance well below the diffraction limit [13]. In the case displayed here, the high-brightness setting is a factor four below the 1 Å diffraction limit. As can be inferred from the plot, higher bunch charge always leads to increased photon brightness. It is also quite impressive to note that because of the effect of IBS, the photon brightness of an 8 pm rad vertical emittance electron beam stretched by LCs is hardly lower than that of a 2 pm rad electron beam at natural bunch length. Without LCs the vertical emittance would have to be reduced to roughly 5 pm rad to achieve the same photon brightness as is achieved with an 8 pm rad beam and LCs. Quite obviously the latter would also achieve a much better lifetime. If the LCs are properly tuned in for bunch lengthening, the photon brightness can be almost doubled by improving the matching between electron and photon beam in the vertical plane. It is important to point out that the 2 pm rad vertical emittance required for the high-brightness setting calls for the emittance coupling set to a comparably generous 0.5% (incl. IBS) whereas the 1 Å diffraction limit of 8 pm rad would most likely require excitation of skew quadrupoles in order to increase emittance coupling to the required 2.2%.

As already pointed out above, the ultimate benchmark is photon brightness and overall electron beam lifetime at an optics and current required to achieve this photon brightness. In this sense, the optics (incl. the optics matching to a specific ID), main cavity settings, Landau cavity tuning, amount of stored current, and IBS are all linked to one another and ultimately to the achieved brightness and lifetime in a way that requires simulating all effect concurrently for every individual configuration. In [4] much emphasis was placed on optics matching to specific IDs and the achievable results. Since the changes to the optics since the last lattice revision are small, no fundamental change is expected in the ID matching procedure or results. Therefore, the combined effect of many IDs on emittance and MA is expected to be close to the originally calculated values. Hence, two figures from [4] are reproduced here showing the influence of number of installed IDs on emittance, radiation losses, and RF acceptance. The ID is assumed to be a fairly typical device for a light source such as the MAX IV 3 GeV storage ring: "pmuL" is a 3.7 m long in-vacuum undulator with 18.5 mm period length, 1.111 T effective magnetic field, and 4.2 mm minimum gap [14]. Figure 49 shows the horizontal emittance as a function of the number of installed pmuL in the ring. Both the effect of IBS (assuming a maximum stored current of 500 mA) and the LCs (assuming bunch lengthening to 50 mm) at two different vertical emittance settings are displayed.

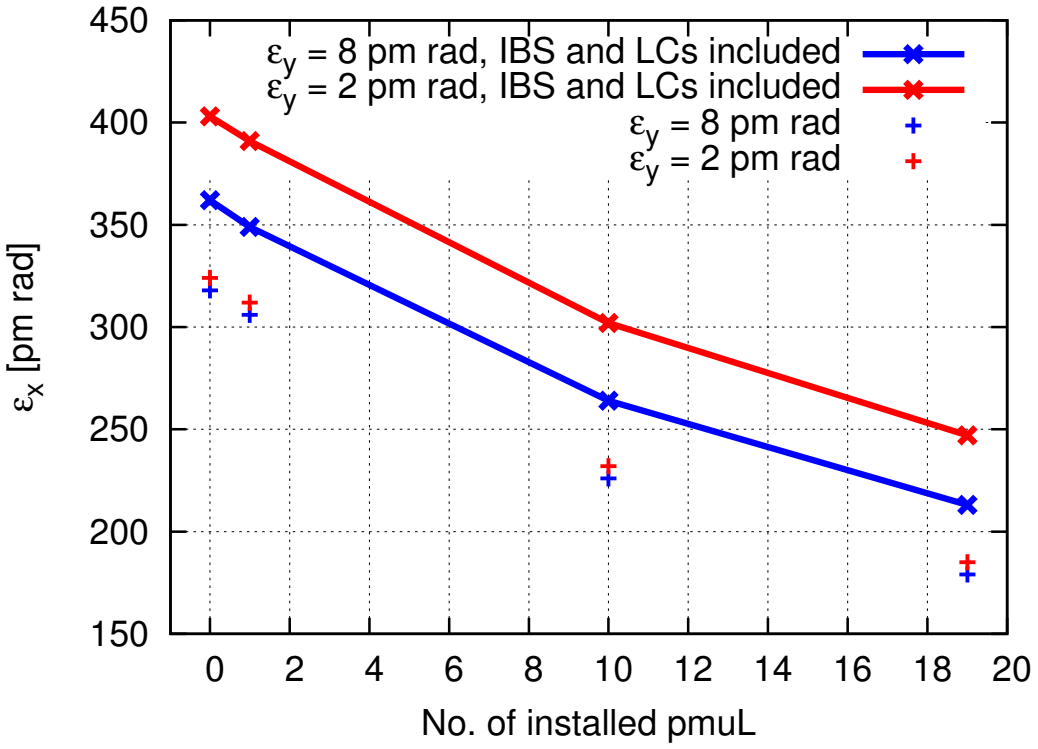


Figure 49: Horizontal emittance as a function of number of installed IDs of type "pmuL". The vertical emittance has been set to 8 pm rad and 2 pm rad, respectively. The effect of IBS (at 500 mA) and LCs (stretching bunches to 50 mm) is indicated. The overall main cavity voltage was assumed to be set at the maximum of 1.8 MV. This figure is reproduced from [4].

The energy loss per turn as function of number of installed IDs is shown in Fig. 50. Assuming that the main RF cavities are operated at maximum voltage the resulting RF acceptance has been calculated and is also displayed. While operating the cavities in this way ensures maximum RF acceptance, it's important to keep in mind that this does not ensure maximum lifetime or minimum emittance (cf. p. 60) and hence actual settings during user operation may vary. For the moment, however, this RF acceptance allows a good estimate of the resulting Touschek lifetime via comparison in Fig. 41. The increase in Touschek lifetime from LCs can then be estimated quite well via scaling according to the bunch lengthening.

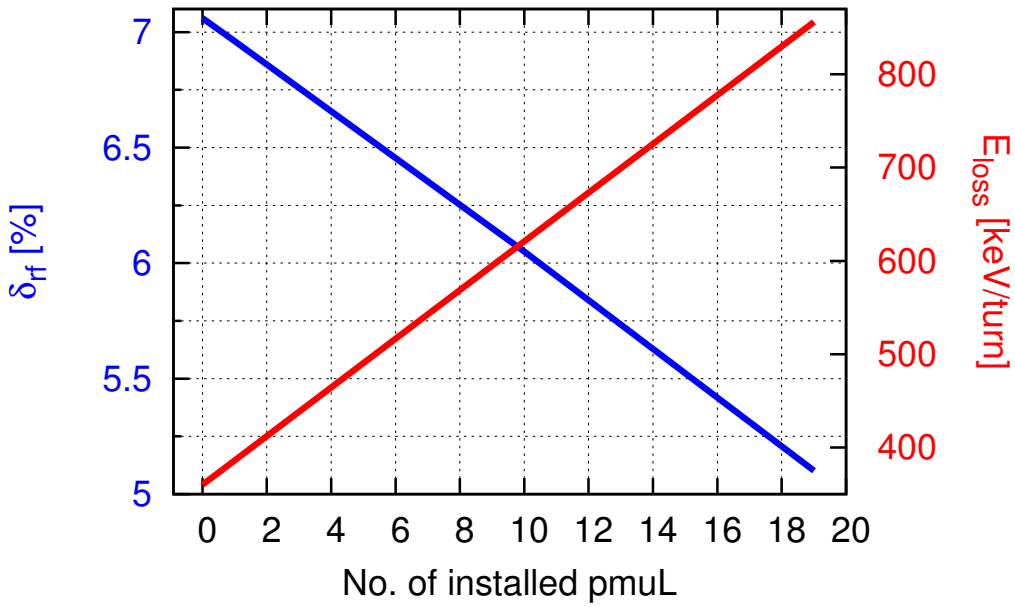


Figure 50: Radiation losses and resulting RF acceptance as a function of number of installed IDs of type "pmuL". The overall main cavity voltage was assumed to be set at the maximum of 1.8 MV. This figure is reproduced from [4].

# 5 Current Lattice Files

Table 12 lists all current official lattice files [1] and what type of elements are included. The lattice files are human-readable and in Tracy-3 format. All lattice files contain BPMs and correctors (SOFB). Girder markers are also included.

ID matching has so far not been re-evaluated for the new m4-20121107-430 lattice branch. Regarding properties of the lattices matched to IDs, no significant differences are expected since the original design optics have been restored very well in the new lattice branch. Hence, the m4-20110117-420 lattice files which include IDs and matched optics are being retained [3]. The analysis of ID matching presented in Internal Note 20110117 [4] should remain valid.

Table 12: List of all current lattice files.

| File name | Lattice contains |
|---|---|
| m4-20121107-420-bare.lat | Bare ring lattice, injection elements included |
| m4-20110117-420-01pmuL.lat | Lattice/optics not up-to-date, but retained to demonstrate ID matching: 1 pmuL installed in otherwise bare ring |
| m4-20110117-420-10pmuL.lat | Lattice/optics not up-to-date, but retained to demonstrate ID matching: 10 pmuL installed in otherwise bare ring |
| m4-20110117-420-19pmuL.lat | Lattice/optics not up-to-date, but retained to demonstrate ID matching: 19 pmuL installed, "fully loaded ring" |
| m4-20110117-420-2W.lat | Lattice/optics not up-to-date, but retained to demonstrate ID matching: $2 \times 4\,\mathrm{m}$ PMDW installed in otherwise bare ring |
| m4-20110117-420-10U.lat | Lattice/optics not up-to-date, but retained to demonstrate ID matching: $10 \times 3\,\mathrm{m}$ IVU installed in otherwise bare ring |

# References


[1] The updated lattice files can be found at http://www.maxlab.lu.se/node/1135

[2] L.-J. Lindgren, unpublished internal note, November 5, 2012.

[3] Retained previous version lattice files can be found at http://www.maxlab.lu.se/node/1135

[4] MAX-lab Internal Note 20110117, available at http://www.maxlab.lu.se/node/999

[5] The MAX IV Detailed Design Report, available at http://www.maxlab.lu.se/node/1136

[6] J. Safranek, NIM A, 388, pp. 27, 1997.

[7] D. Einfeld, unpublished internal note, January 29, 2013.

[8] L.-J. Lindgren, M. Johansson, private communication, January 29, 2013.

[9] M. Johansson, private communication, February 27, 2013.

[10] MAX-lab Internal Note 20130724, available at http://www.maxlab.lu.se/node/999

[11] A. Streun, Momentum acceptance and Touschek lifetime, SLS Internal Note 18/97, http://ados.web.psi.ch/slsnotes/sls1897a.pdf.

[12] Å. Andersson et al., "The 100 MHz RF System for the MAX IV Storage Rings", Proceedings of IPAC2011, San Sebastián, Spain, MOPC051, p. 194.

[13] S.C. Leemann, M. Eriksson, "Coupling and Brightness Considerations for the MAX IV 3 GeV Storage Ring", Proceedings of NA-PAC'13, Pasadena, CA, USA, MOPHO05, p. 243.

[14] E. Wallén, S.C. Leemann, "Strategy for Neutralizing the Impact of Insertion Devices on the MAX IV 3 GeV Ring", Proceedings of PAC'11, New York, NY, USA, TUP235, p. 1262.